Technische Universität München

TUM School of Life Sciences

Lehrstuhl für Systemverfahrenstechnik

Development of low-field and mobile MRI devices and methods to monitor xylem emboli in trees

Marco Meixner

Vollständiger Abdruck der von der TUM School of Life Sciences der Technischen Universität München zur Erlangung des akademischen Grades eines Doktors der Naturwissenschaften (Dr. rer. nat.) genehmigten Dissertation.

Vorsitzender: Prof. Dr. rer. nat. Klaus Richter

Prüfer der Dissertation: 1. apl. Prof. Dr.-Ing. habil. Petra Först

                             2. Prof. Dr. rer. nat. Anja Rammig

Die Dissertation wurde am 07.06.2021 bei der Technischen Universität München eingereicht und durch die TUM School of Life Sciences am 02.09.2021 angenommen.

ii

Content

Summary

A prerequisite of judging and mitigating the extent of massive tree dieback due to climate change is an understanding of the causal link between drought and tree death. A wealth of data indicates the xylem to be a likely candidate for this link, referring to the long-distance water transport system from the plant's roots to its leaves. Xylem transport is driven by evaporation at the leaves and relies on water being passively pulled through the plant in continuous columns, sometime referred to as 'threads' or 'ropes of water'. This causes the xylem water to be under high tension and complicates invasive measurements of xylem functionality or flow, since any xylem injury due to cutting may cause the continuous water columns to break, resulting in artificial xylem blockage. Drought stress is considered to cause xylem blockages, referred to as xylem emboli.

Magnetic resonance imaging (MRI) offers a number of unique advantages over other non-invasive approaches to image the xylem. Examples are that pixel values can reflect physical quantities, and that the energy deposition in the sample is negligible, allowing continuous measurements. Despite these advantages, however, MRI has only been used for a limited number of xylem studies. This can be ascribed to its relatively coarse spatial resolution, but more importantly to the fact that small, open MRI scanners, which accept living plants in an upright position and over longer time periods, are not readily available. Also, scanners that can be moved about easily and are sufficiently robust for outside measurements, while delivering high image quality, have not been introduced yet.

In this thesis small, low-field MRI devices and methods are developed and evaluated, which aim to image xylem water content changes in trees, and to monitor and quantify xylem embolism formation due to drought stress in particular. A dedicated combination of purpose-built hardware, imaging software and data evaluation routines is introduced and evaluated.

It is demonstrated that the shortcomings of a small and light permanent magnet can be compensated by using a multi-spin echo (MSE) imaging pulse sequence, which allowed quantitatively imaging water content (A) and signal decay time (T_2). Pixelwise multiplication of both quantities resulted in high quality $A*T_2$ product images. By means of a simulation it was shown that the correlation of T_2 and xylem conduit diameters makes $A*T_2$ product images a sensitive tool to monitor xylem dry-down. Xylem vulnerability curves are obtained by applying a threshold to xylem-masked $A*T_2$ images.

The utility of quantitative MR images of different spatial resolutions for recognizing and quantifying xylem emboli is investigated. The xylem of young beech and spruce trees is continuously monitored at different pixel sizes during dry-down. Even at pixel sizes larger than 0.5*0.5 mm², xylem dry-down could be spatially and temporally resolved and vulnerability curves could be obtained and quantified. Spatial resolution thus can be sacrificed to allow the use of much less powerful, and much more mobile

MR imagers, or to allow much shorter image acquisition times, without losing the ability to visualize and quantify embolism formation.

Finally, a dedicated combination of imaging hardware and software is paired with a set of mobile gradient amplifiers, resulting in a complete mobile imager with a weight of less than 45 kg. The self-made magnet, gradient coils and gradient amplifiers are proven to be sufficiently robust for outside measurement, which were performed at an ambient temperature of 7°C in an orchard. Also, the mobile MRI scanner is used in a continuous manner, imaging the stem of a young beech tree during leaf development over two months in the greenhouse. The resulting time series of images revealed an increase in signal decay time (T_2) in certain xylem locations, which could be interpreted to visualize in vivo the mobilization and translocation of starch from older to younger xylem via pith tissue.

Zusammenfassung

Um die Folgen der Klimaerwärmung für Bäume und Wälder abzuschätzen und ihnen begegnen zu können ist ein genaues Verständnis des kausalen Zusammenhangs zwischen Trockenstress und dem Tod einer Pflanze unerlässlich. Zahlreiche Studien deuten darauf hin, dass für viele Spezies das Xylem diesen Zusammenhang bildet, wobei es sich um das Wassertransportsystem einer Pflanze von den Wurzeln zu den Blättern handelt. Xylemtransport wird durch Verdunstung in den Blättern verursacht, wodurch das Wasser in kontinuierlichen Wassersäulen passiv durch die Pflanze gezogen wird, die auch als ‚Wasserfäden' bezeichnet werden könnten. Das Wasser im Xylem ist daher unter Spannung, was eine invasive Messung der Xylemfunktionalität oder Flussmessungen erschwert, da jegliche Verletzung des Xylems zu künstlichen Xylemblockaden führen kann. Nach dem derzeitigen Verständnis verursacht Trockestress Blockaden des Xylems durch Gas, die als Xylemembolien bezeichnet werden.

Bei der Untersuchung des Xylems bietet Magnetresonanztomographie (MRT) verschiedene Vorteile gegenüber anderen nichtinvasiven bildgebenden Methoden. Pixelwerte von MRT-Bildern können quantitativ physikalische Parameter des untersuchten Objektes wiedergeben. Außerdem ist die Energiedeposition bei MRT in aller Regel vernachlässigbar, was kontinuierliche Messungen erlaubt. Trotz dieser Vorteile wurde MRT bisher nur für einige wenige Xylem-Studien eingesetzt. Dies kann auf die relativ grobe räumlich Auflösung zurückgeführt werden; noch maßgeblicher ist aber die Tatsache, dass es nur wenige kompakte und offene MRT-Scanner gibt, in denen lebende Pflanzen aufrecht stehend und über längere Zeiträume gemessen werden können. Außerdem stehen keine mobilen Geräte zur Verfügung, die leicht und robust genug für Messungen im Freien bei hoher Bildqualität sind.

In dieser Arbeit werden kompakte MRT-Geräte mit begrenzter Feldstärke entwickelt und evaluiert, mit dem Ziel Änderungen im Xylemwassergehalt von Bäumen zu visualisieren. Speziell soll die durch Trockenstress hervorgerufene Entstehung von Xylemembolien in vivo beobachtet und quantifiziert werden, idealerweise auch bei Pflazen in ihrer natürlichen Umgebung (z.B. Wald oder Obstgarten). Eine dezidierte Kombination von Hardware, Bildgebungssoftware und Datenauswertungsroutinen wird dafür entwickelt und evaluiert.

Es wird gezeigt, dass die Defizite von kleinen, leichten Permanentmagneten mit Hilfe von Multi-Spin Echo Pulssequenzen kompensiert werden können. Diese Pulssequenzen erlauben das Erstellen quantitativer Wassergehalts- und T_2-Bilder. Durch pixelweise Multiplikation werden $A*T_2$ Produktbilder von hoher Bildqualität erstellt, die sich außerdem als sensitiv für die Austrocknung von Xylemgefäßen erwiesen haben. Anhand einer Simulation wird gezeigt, dass diese Sensitivität auf eine Korrelation von T_2 und Xylem-Gefäßdurchmessern zurückgeführt werden kann. Außerdem werden Xylemverwundbarkeitskurven durch Binarisierung von $A*T_2$ Produktbildern erstellt.

Des Weiteren wird untersucht wie gut sich MRT-Bilder verschiedener räumlicher Auflösung für das Detektieren und Quantifizieren von Xylemembolien eignen. Dafür wird das Xylem junger Buchen und Fichten kontinuierlich bei drei unterschiedlichen räumlichen Auflösungen per MR-Bildgebung beobachtet, während die Pflanzen ausgetrocknet werden. Das Ergebnis war, dass auch bei Pixelgrößen über 0.5*0.5 mm² die Xylemaustrocknung zeitlich und räumlich aufgelöst werden kann und korrekte Xylemverwundbarkeitskurven erstellt werden können. Es kann geschlussfolgert werden, dass die räumliche Auflösung für das Erstellen von Xylemverwundbarkeitskurven verringert werden kann. Eine geringere räumliche Auflösung würde zum einen die Nutzung von wesentlich einfacheren und mobileren MRT-Scannern erlauben; außerdem kann die Zeit für die Bildaufnahme signifikant verringert werden, ohne dass man die Fähigkeit einbüßt die Bildung von Xylemembolien zu visualisieren und zu quantifizieren.

Eine dezidierte Kombination von Bildgebunds-Hardware und -Software wird mit speziell angefertigten mobilen Gradientenverstärkern kombiniert. So wurde ein integrierter, mobiler MRT-Scanner mit einem Gesamtgewicht von 45 kg konstruiert. Die Widerstandsfähigkeit von Magnet, Gradientenspulen und Gradientenverstärker werden bei Bildaufnahmen von hoher Qualität im Freien bei einer Außentemperatur von 7 °C in einem Obstgarten gezeigt. Der MRT-Scanner wird außerdem für eine kontinuierliche Messung in einem Gewächshaus über zwei Monate verwendet, bei der ein Buchenstamm während der Blattentstehung im Frühjahr in vivo mit Bildgebung untersucht wurde. Die erhaltene Zeitserie von quantitativen Bildern zeigt ein Ansteigen der Signalzerfallszeit (T_2) in bestimmten Stammregionen, welche als Mobilisierung und Transport von Zucker von älterem zu jüngerem Xylem über das Markgewebe interpretiert werden kann.

List of publications

Peer-reviewed publications

Marco Meixner, Martina Tomasella, Petra Foerst, Carel Windt. 2020. A small-scale MRI scanner and complementary imaging method to visualize and quantify xylem embolism formation. *New Phytologist* **226**: 1517–1529.

Marco Meixner, Petra Foerst, and Carel W. Windt. 2021. Reduced spatial resolution MRI suffices to image and quantify drought induced embolism formation in trees. *Plant Methods* 17.1: 1-12.

Marco Meixner, Johannes Kochs, Petra Foerst, Carel Windt. 2021. An integrated magnetic resonance plant imager for mobile use in greenhouse and field. *Journal of Magnetic Resonance* **323**: 106879.

Oral presentations

Carel Windt, Marco Meixner, Johannes Kochs. Mobile NMR for plant sciences: Engineering for sensor-like, outdoor use. 13th International Conference on Magnetic Resonance Microscopy (ICMRM), Munich, Germany, 2nd-6th August 2015.

Petra Foerst, Iris Schmitz-Schug, Marco Meixner. Einsatzmöglichkeiten der Niederfeld-NMR für die Prozess- und Produktanalyse beim Trocknen. ProcessNet Jahrestagung Trocknungstechnik. Leipzig, Germany, 6th May 2015.

Marco Meixner, Martina Tomasella, Petra Foerst, Carel Windt. Development of a simple, mobile MRI plant imager. International Symposium on Sensing Plant Water Status - Methods and Applications in Horticultural Science, Potsdam, Germany, 5th-7th October 2016.

Carel Windt, Siegfried Jahnke, Marco Meixner, Johannes Kochs. Mobilizing magnetic resonance: sensor like applications and mobile imaging. International Symposium on Sensing Plant Water Status - Methods and Applications in Horticultural Science, Potsdam, Germany, 5th-7th October 2016.

Poster presentation

Marco Meixner, Martina Tomasella, Petra Foerst, Carel Windt. Development of a robust mobile plant imager. 13th International Bologna Conference on Magnetic Resonance in Porous Media, Bologna, Italy, 4th-8th September 2016.

1   Introduction

1.1   Basic tree stem anatomy

Trees are vascular plants, consisting of three basic tissue types. Parenchyma is unspecialized ground tissue that performs cell division and other functions. The other two tissue types are the outer dermal tissue, which provides protection, and vascular tissue for transport of water, nutrients and metabolites, namely the xylem and the phloem. The main organs of vascular plants are the root, the shoot and the leaf. In case of a tree, water enters the plant at the roots and is transported to the treetop via the long-distance transport system in the center of the stem, referred to as the xylem (Fig. 1). After the seedling phase the xylem tissue constitutes the majority of the stem volume, as it makes up the wood of a tree. At the treetop the majority of water is lost to transpiration and the minority is used for photosynthesis to produce sugar. The sugar subsequently is moved back down to be stored or metabolized via the other type of transport tissue in the outer layers of the stem, referred to as the phloem. While xylem transport can be considered as flowing water (speeds of centimeters to meters per hour), phloem transport is much slower and sometimes hard to distinguish from diffusion.

Trees not only show longitudinal growth in the direction of the shoot axis, but also lateral growth, increasing the shoot diameter (also referred to as secondary growth). This enables trees to increase the conductivity and stability of their shoots, and allowed them to become some of the largest land organisms. Any lateral or secondary growth is initiated in the cambium, which is a ring of unspecialized cells between the xylem and the phloem. Cells that form at the cambium subsequently specialize to become either xylem, phloem or parenchyma cells. Growth in lateral direction happens as layers of xylem cells grow inward, while layers of phloem cells grow outward from the cambium. Parenchyma cells form as discrete rays in the xylem in radial direction, often connecting in the center of the stem and referred to as the pith. Pith tissue serves as a connection between xylem and phloem to transport and store nutrients, such as starch (Fig. 1).

Two main types of xylem architectures are distinguished, one of which is found in gymnosperm (seed producing plants), the other in angiosperm (flowering plants) tree species. Gymnosperm wood almost exclusively consists of tracheids, which provide the two main xylem functions, namely support and water transport. In evolutionarily more advanced angiosperms different types of xylem cells perform different tasks. Tracheids and sometimes also vessels, are specialized for water transport, while wood fibers provide mechanical stability. Vessel containing angiosperm wood is further differentiated according to the arrangement of the vessels into ring porous and diffuse porous wood. In Fig. 1 the wood of semi-ring porous beech is shown, which can be considered an intermediate type of wood architecture between ring porous and diffuse porous.

In temperate regions with significant temperature fluctuations annual rings form. Xylem that forms during spring has larger cell diameters and thin cell walls, referred to as earlywood. It is required to maximize water transport during leaf formation and intense growth. In late summer conduits with a smaller diameter and thick cell walls form, referred to as latewood, which provides more stability and less conductivity than earlywood. As in temperate regions there is hardly any growth or metabolism during winter, in the xylem the border between latewood (small conduits) and earlywood (large conduits) can be recognized as the border of two annual rings (Reece *et al.*, 2014).
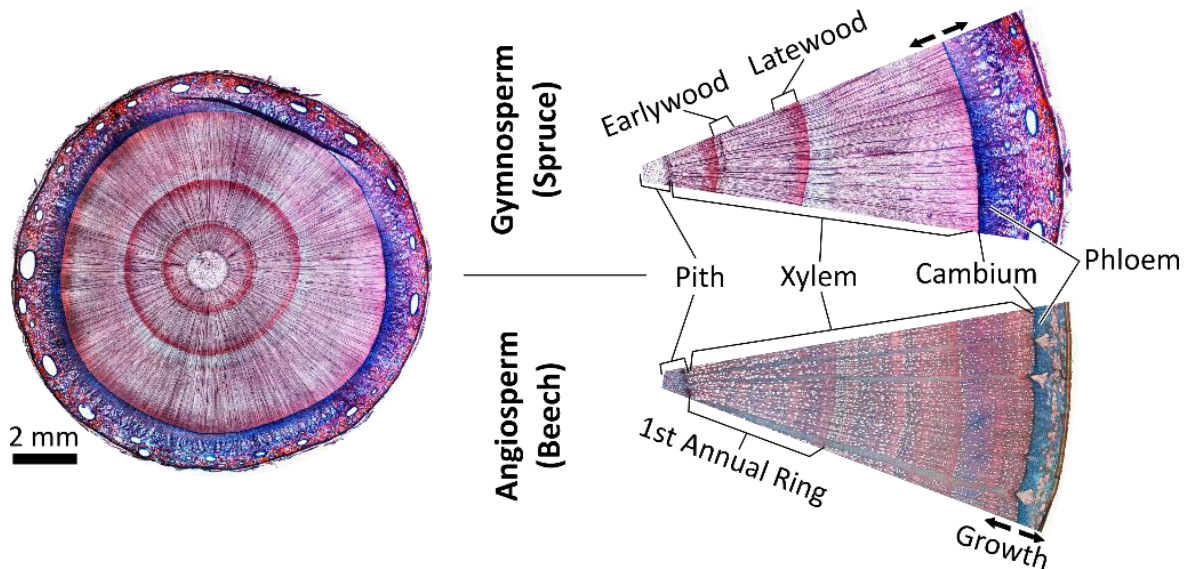

Figure 1:   The basic anatomy of a tree stem illustrated by means of a stem cross section of a 1.2 cm diameter three-year-old spruce, next to two angular cuts of the same spruce cross section and of a three-year-old beech tree. The main types of functional stem tissues are indicated.

1.2   The cohesion-tension theory

During transpiration, more than 95 percent of the water that is taken up by a tree at the roots is lost through the stomata at the leaves (Sutcliffe, 1968), since hundreds of water molecules are lost per one carbon dioxide molecule that is taken up from the air for photosynthesis. In case of tall trees, this results in the need for transporting more than one hundred liters of water on a clear day to heights beyond 50 m, to replace the water that is lost at the leaves. A question that has long occupied the minds of plant scientists is therefore how tall trees manage to transport water to such heights via the xylem, without an active pumping mechanism. Today's understanding of this long distance water transport in trees has first been published by Dixon and Joly (1894) and is referred to as the cohesion-tension theory. According to this theory water is transported under tension in continuous columns

without the need for metabolic energy, once the xylem has been grown (Sperry, 2011). In the following sections some of the key aspects of this theory will be discussed.

1.2.1   Long-distance water transport anatomy

The key anatomy in the three plant organs (root, stem, leaf) in the context of the cohesion-tension theory is illustrated in Fig. 2, which has been adapted from Venturas *et al.* (2017). The driving force behind the movement of the water upward in the stem against the gravimetric force (F_g) is generated by capillary rise at the evaporating surfaces inside of the leaf. Guard cells (Gc) in the leaves regulate transpiration by changing the size of the leaf openings, referred to as stomata. The actual air-water-interface, however, is not at the stomata, but inside of the leaves, within narrow (1-10 nm) pores in the walls of mesophyll cells (Mc), as well as in intercellular spaces. Adhesion of the water molecules to the walls of the cell pores results in a capillary force (F_c) and the formation of concave water menisci. Evaporation of water molecules from the pores in combination with the cohesion of the water molecules, withstanding the tendency of the meniscus to become more concave, causes a tension, and water is pulled upward to replace the water evaporated from the menisci (Pickard, 1981; Venturas *et al.*, 2017).

This tension is transmitted via hydraulically continuous water columns from the leaves to the roots, and causes soil water to enter a transpiring plant via root cells (Rc). The majority of the water moves in between the loosely packed root cells, while some water is also pulled across the membranes of root cells. A protective band of cell wall material, called the Casparian strip, causes all the water to be pulled across cell membranes before entering the xylem in the root center. This results in microscopic air bubbles being filtered from the water (Tyree and Zimmermann, 2002).

The xylem is an intricate network of elongated conduits, most of which are oriented vertically in the annual rings of the stem of a tree, inside of the cambium. Accordingly, conduits are water filled when they are functional. For the purpose of water exchange between the plant and its environment the xylem tissue also reaches into the roots and the leaves of the plant. The xylem conduits have a lignin secondary cell wall which is nonliving at maturity, prevents collapse due to the tension of the water (Hacke *et al.*, 2001) and enables support for tall plants. Xylem conduits are interconnected to adjacent conduits via pits, which are thin areas consisting only of primary cell walls. Pits divide adjacent conduits by a thin sheet of cellulosic meshwork, referred to as the pit membrane (Sperry, 2011).

Two types of xylem conduits are differentiated. The evolutionarily older type of conduit can be found in angiosperm and gymnosperm xylem and is referred to as a tracheid, which is 1 to 10 mm long and typically around 50 µm wide. The evolutionarily more advanced type of conduit can only be found in angiosperm xylem and is referred to as a vessel, which can be meters long and up to 500 µm wide. Connecting pits allow water exchange between two water filled conduits, but up to a limit prevent air

to move from a cavitated conduit to an adjacent water filled one. In this manner, pits provide interconduit water passage, but at the same time prevent air to spread within the xylem. A very large number of interconnected conduits form a network, which provides redundancy in case of cavitation of individual conduits by allowing lots of alternative pathways for the water (Venturas *et al.*, 2017).
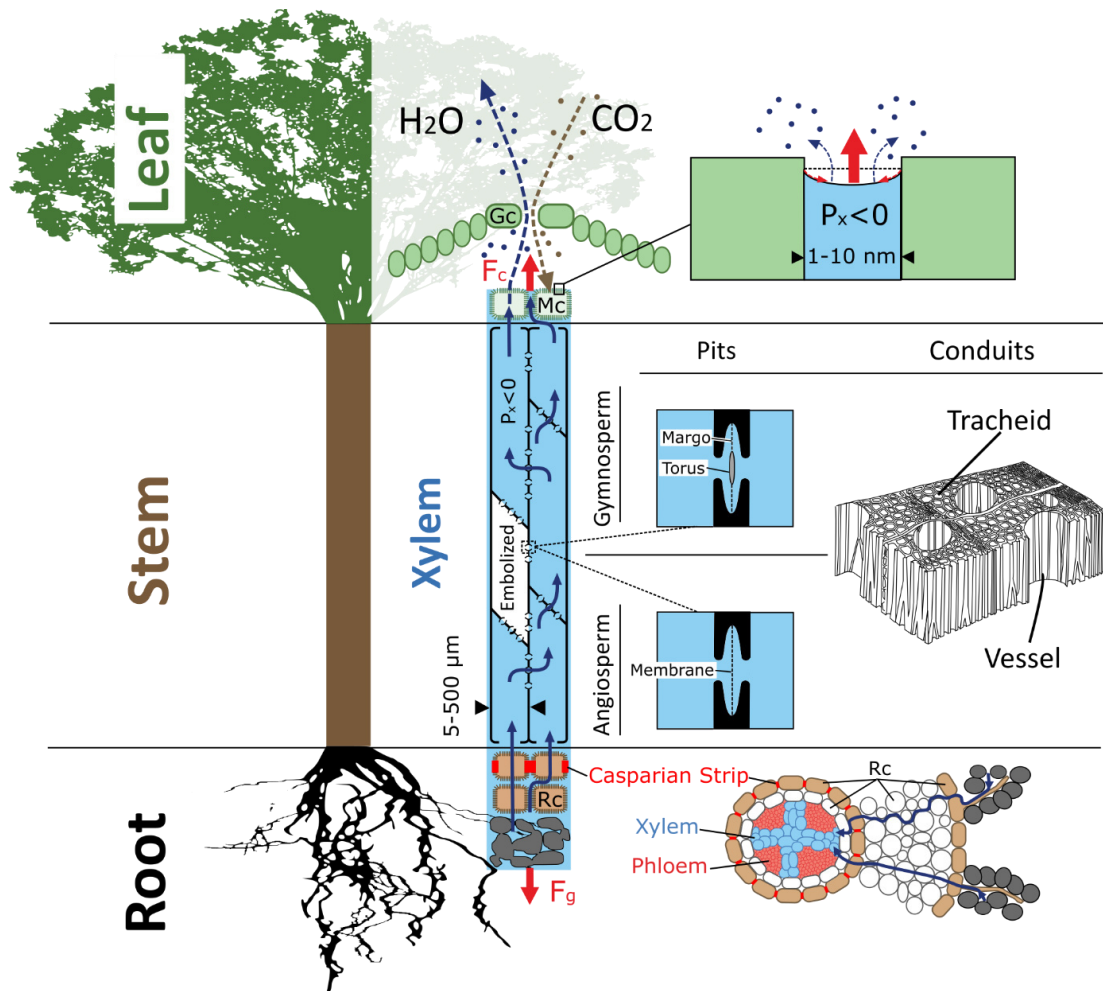

Figure 2:   Key anatomy in the different plant organs (root, stem, leaf) in the context of the cohesion-tension theory. The main reason plants have to transport water to their leaves is that they lose water as they take up CO_2 at the leaves. Water enters the xylem (negative pressure P_x) at the roots via root cells (Rc) and through the Casparian strip. In the xylem the water moves up through the conduits (vessels and tracheids), moving from one conduit to another via the pits. The lifting force is of capillary nature (F_c), acting on water (against the gravimetric force F_g) in the 1-10 nm wide pores in the walls of the mesophyll cells (Mc) of the leaves. The plant regulates transpiration via the Guard cells (Gc) of the leaf. Parts of this Figure were adapted from Venturas et al. (2017), with permission from The Journal for plant Botany.

1.2.2   Water under tension

One aspect that is often not straightforward to comprehend is the idea of water in the xylem being in a metastable state, as it transmits the pulling force from the leaves to the roots in the form of tension. This tension is also referred to as negative pressure by plant scientists (Tyree and Zimmermann, 2002), but also by experts on the physics of phase changes of water (Caupin et al., 2012). Water remaining liquid outside of the boundaries of the ordinary phase diagram, however, is more common than one might intuitively consider. Experimental work has shown that water at atmospheric pressure can remain liquid between -41°C and 280°C (Debenedetti, 1996), provided that disturbances like vibrations, impurities or container wall irregularities are avoided to a large degree. This state is referred to as metastable. Another way to bring water into a metastable state is by stretching it (Caupin & Herbert, 2006), which is the state that xylem water is assumed to be in during transpiration. While this type of metastability is less commonly known, the physics of it has been investigated in-depth (Trevena, 1984; Caupin et al., 2012; Meadley & Angell, 2015). This can also be said about the breakdown of this metastable state, referred to as cavitation (Caupin & Herbert, 2006; Franc & Michel, 2006; Davitt et al., 2010).

In a comprehensive review on the stability of liquids in a stretched state Chaupin et al. (2012) compared the theoretical tensile stability of water to values found experimentally. On the basis of the minimum work required to create a bubble of water vapor in a liquid, they calculated that cavitation can be expected at a pressure of -190 MPa for pure water at room temperature. This value, however, has not been found experimentally when comparing the results of different approaches to test the tensile strength of water, which were found to scatter widely. Three different methods (centrifugation: Briggs, 1950; acoustic: Galloway, 1954; Berthelot tube: Henderson & Speedy, 1980) and results from an artificial tree (Wheeler & Stroock, 2008) yielded values between -25 and -35 MPa, while a fourth method resulted in a value of -140 MPa (Zheng et al., 1991). It has been assumed that these discrepancies between the theoretical value and experimental findings are due to destabilizing impurities and what has been referred to as stabilizing impurities (Davitt et al., 2010; Caupin et al., 2012; Meadley & Angell, 2015). In any case, theoretical considerations as well as results of all four experimental methods confirm that water provides sufficient tensile strength to support even the most negative water pressures of -14 MPa that have been found in the xylem of trees (Hacke et al., 2001). The circumstances under which cavitation occurs will be discussed in more detail in section 1.3.

1.2.3   Pressure jump at capillary water menisci in the leaf

Another aspect of the cohesion-tension theory that can be difficult to comprehend is the idea that water can get out of the plant via the leaves, but air is not sucked into the plant, despite the significant negative pressures in the xylem. This behavior can be explained by the limited size of the pores in the

walls of the mesophyll cells (1 to 10 nm, Fig. 2). The static pressure jump across the interface of air and water can be estimated by the Young-Laplace equation (Gennes *et al.*, 2013)

$$\Delta P_{a/w} = \frac{4\sigma \cos\Theta}{d_p} \quad . \tag{1}$$

Assuming a pore diameter d_p of 5 nm, a contact angle Θ of zero (completely wetting) and a surface tension σ of 0.073 N/m results in a pressure difference $\Delta P_{a/w}$ of 58.4 MPa, also referred to as capillary pressure.

Replacing the pressure difference $\Delta P_{a/w}$ by a term for the height (h) dependent hydrostatic pressure of water $\rho_w\, g\, h$ results in Jurin's equation (Jurin, 1718)

$$h = \frac{4\sigma \cos\Theta}{\rho_w\, g\, d_p} \quad , \tag{2}$$

which can be used to calculate the height to which water rises in a capillary. Inserting the same numbers as above, as well as the density of water, results in a height close to 6000 m. This solves the common misconception of using the same formula, but inserting the diameter of a small xylem capillary of 5 µm for d_p, which results in a capillary rise of only 6 m. This is in line with Koch *et al.* (2004), who pointed to increased leaf water stress due to gravity and resistance of long pathways as the most likely factors limiting tree height, not the pulling capillary force in the leaves.

Further support of the idea that the ultimate lifting force is generated by capillary rise into the pores of the mesophyll cell walls has come from the fabrication of synthetic leaves. Such leaves were based on nanoporous hydrogels and shown to be capable of creating negative pressures according to the same principles between -20 MPa and -33.8 MPa (Wheeler & Stroock, 2008; Wang *et al.*, 2020).

1.2.4   Xylem water potential

As water in plants is confined, osmotic and capillary forces may play a significant role besides gravity and pressure. To take into account all forces inside of a plant that may act on water, the plant water potential has been defined as follows (Cruiziat *et al.*, 2002; Tyree and Zimmermann, 2002)

$$\Psi = \frac{\mu_w - \mu_w^0}{V_w} = P + \rho_w\, g\, h + \Pi \quad . \tag{3}$$

It is defined for any water containing plant organ as the difference between the chemical potential of water in the plant μ_w and water at atmospheric pressure μ_w^0, both at the same temperature. Dividing this difference by the molar volume V_w of water results in the unit of pressure for the water potential, typically given in MPa. The different terms are the hydrostatic water pressure P, a gravitational term $\rho_w\, g\, h$ and the osmotic potential Π.

One of the most often used methods to measure the water potential, including the work presented in this thesis, was introduced by Scholander et al. (1965) and is referred to as the pressure chamber or pressure bomb method. A small twig is harvested from the plant. To make sure the water potential of the twig and the stem equilibrate, Scholander's method has been extended by stopping the twig's transpiration (it is covered with plastic and aluminum foil) and harvesting it after a waiting time of typically 15 minutes. Subsequently, the twig is put inside a metal chamber and by means of a rubber seal positioned in such a way that the cut end sticks out of the chamber, so that it can be observed with a stereomicroscope (Fig. 3). The pressure in the chamber is slowly increased until water is observed to be squeezed out of the cut xylem of the twig. The corresponding pressure is referred to as the balance pressure and its absolute value is assumed to equal that of the xylem pressure, while both are of opposite sign (Tyree and Zimmermann, 2002). When introducing the method, Scholander et al. (1965) illustrated that the water potentials are increasingly negative at increasing plant heights, as well as in case of species that grow in drier or elevated habitats.
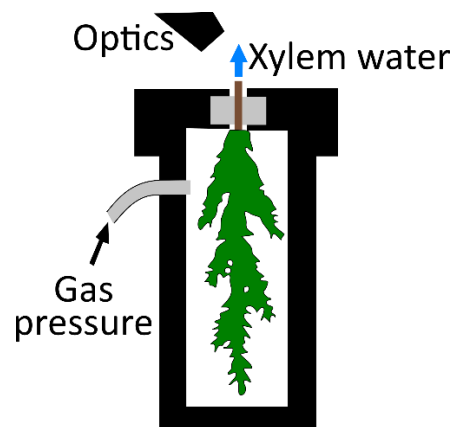

Figure 3:   Illustration of the pressure chamber technique to measure the xylem water potential. The pressure that is required to force water out of the xylem and the xylem pressure are assumed to be the same in absolute values.

1.2.5   Xylem water transport

Water movement in the xylem is caused by water potential differences, with water moving from higher to lower water potential, which in the xylem of trees typically means that water moves from negative water potential at the bottom of the plant to more negative water potential towards the treetop. As solute concentration in the xylem is low and solutes can move relatively freely, no significant differences in the osmotic potential can be expected within the xylem and the term can be neglected for the quantification of xylem transport. If one considers a static water column, the remaining two terms of the water potential, the hydrostatic pressure (P) and the gravitational term ($\rho\, g\, h$), balance each other out, resulting in the same water potential Ψ at any height. In this static water column the

potential energy of the water due to gravitation increases at increasing height, while the pressure decreases at increasing height. This results in a negative hydrostatic pressure gradient of -0.01 MPa/m. Water movement in a plant against gravitation can only be caused by a pressure gradient that is more negative than this hydrostatic pressure gradient, resulting in a negative water potential gradient $\partial \Psi / \partial x$ in height direction. This was confirmed by studies measuring the xylem pressure of tall trees at different heights. While those studies confirmed the hydrostatic pressure gradient prior to transpiration at predawn, the initiation of transpiration caused the xylem pressure gradient to become more negative than the hydrostatic pressure gradient (Bauerle *et al.*, 1999; Koch *et al.*, 2004).

The conductivity or resistance of the xylem determines the flow that is caused by a particular water potential gradient. This correlation between the water potential gradient and the resulting flow can be approached in different ways. When the xylem is considered as an assembly of individual pipes, the volume flow (Q) through one pipe of radius r can be described by the Hagen-Poiseuille law (η: viscosity)

$$Q = -\frac{r^4 \pi}{8\eta} \frac{\partial \Psi}{\partial x} \qquad (4)$$

The implications of the fact that the conductivity, which is the proportional factor between Q and $\partial \Psi / \partial x$, scales with the fourth power of the pipe radius r is illustrated in Fig. 4, showing three blocks of wood which all have the same hydraulic conductivity (Tyree and Zimmermann, 2002). Studies on cut stem pieces of trees showed, however, that only 33 to 67% of the theoretical conductance is actually reached (Tyree & Zimmermann, 1971; Petty, 1978, 1981), which has been ascribed to xylem conduits not being perfectly round, as well as the flow being interrupted by xylem pits. The matter is complicated further, as in vivo magnetic resonance imaging (MRI) flow studies on angiosperm trees showed that not all water filled vessels do actually conduct water (Homan *et al.*, 2007; Nagata *et al.*, 2016), and that in grapevine the pressure drop in height direction across different vessels is not constant, but that lateral pressure gradients appear to redirect some flow from larger to narrower xylem elements (Bouda *et al.*, 2019).
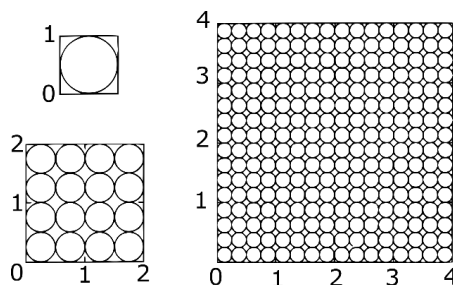

Figure 4:   Illustration of the Hagen-Poiseuille law. All three blocks of wood have the same hydraulic conductivity, which for an individual conduit relates to the fourth power of the conduit radius. This figure was adapted from Tyree & Zimmermann (2002) with permission from Springer.

While the xylem structure of angiosperm plants more closely resembles an assembly of pipes (as they are long, relatively wide and round), Brodersen *et al.* (2019) argued that coniferous xylem (conifers are a subset of gymnosperms, often with needle-like leaves), with its short, densely packed and highly interconnected tracheids, is more accurately described as a porous medium and the use of Darcy's law (Couvreur *et al.*, 2018), with the volume flow scaling linearly with wood permeability and the cross-sectional area. A third approach is to quantify xylem flow by using Ohmic analogies (Cruiziat *et al.*, 2002). The difference between coniferous and angiosperm xylem in terms of conductivity is confirmed by significantly lower speeds of the transpiration flow in coniferous tracheids (20-40 centimeters per hour) than in the vessels of broad-leaved trees (5 meters per hour is common, 44 meters per hour has been recorded in an oak) (Brown, 2013).

1.3   Xylem cavitation and hydraulic failure

Xylem water is subject to the interdependence of transpiration at the leaves, xylem conductance and availability of soil water. If transpiration exceeds water supply from the soil, the xylem pressure will become more and more negative and the tension in the xylem grows, eventually resulting in xylem conduits to cavitate. In this manner, warmer periods of high transpiration and limited water supply can significantly impair xylem function and may eventually lead to plant death (Tyree & Sperry, 1989; Cruiziat *et al.*, 2002). Significant effort went into the development of methods to determine xylem tension values that cause a certain degree of the xylem to become dysfunctional due to cavitation of conduits. Specifically, those xylem water potential values are of interest at which a point of no return is reached. This value has been found to differ widely with respect to numerous parameters, such as species, age and habitat of the plant.

1.3.1   Embolism formation

A phase change of water in a metastable state can happen in essentially two different ways, referred to as homogeneous and heterogeneous nucleation. Homogeneous nucleation happens in the bulk of the metastable liquid and is not caused by impurities. It reflects the actual cohesive stability of the water molecules, provided by hydrogen bonds, and therefore determines the attainable limit of superheating and supercooling. Under common circumstances the preferential site for the formation of a new phase (leading to cavitation) is provided by suspended and dissolved impurities, referred to as heterogeneous nucleation (Debenedetti, 1996).

More specifically, heterogeneous nucleation in plants is ascribed to the existence of tiny gas bubbles that grow under specific circumstances. The characteristics of those preexisting gas bubbles, however, are not always reported in a consistent manner. In plant science those bubbles are sometimes referred to as air bubbles (Denny, 2011), while more often they are considered to consist of a mixture of air and water vapor (Tyree and Zimmermann, 2002). Franc and Michel (2006) discussed the stability of

different microbubble radii for microbubbles that contain gas and vapor, and that are smaller than 0.5 mm in diameter. This was done in dependence of the pressure of the surrounding liquid p_∞ and a starting radius R_0. The pressure of the liquid (p_∞) was assumed to equal a pressure term for the gas bubble; the latter was composed as the sum of the partial pressure of the gas p_g and its vapor pressure p_v, minus a term for the surface tension $2S/R$, which opposes p_g and p_v

$$p_\infty = p_g + p_\mathrm{v} - \frac{2S}{R} \tag{5}$$

.

Stable bubble scenarios are shown in Fig. 5b for two different starting radii (R_0 and R_0'). Once the pressure of the liquid (p_∞) drops below the critical pressure p_c, there are no more stable radii and the bubble becomes the point of weakness from which the phase change of the liquid originates.
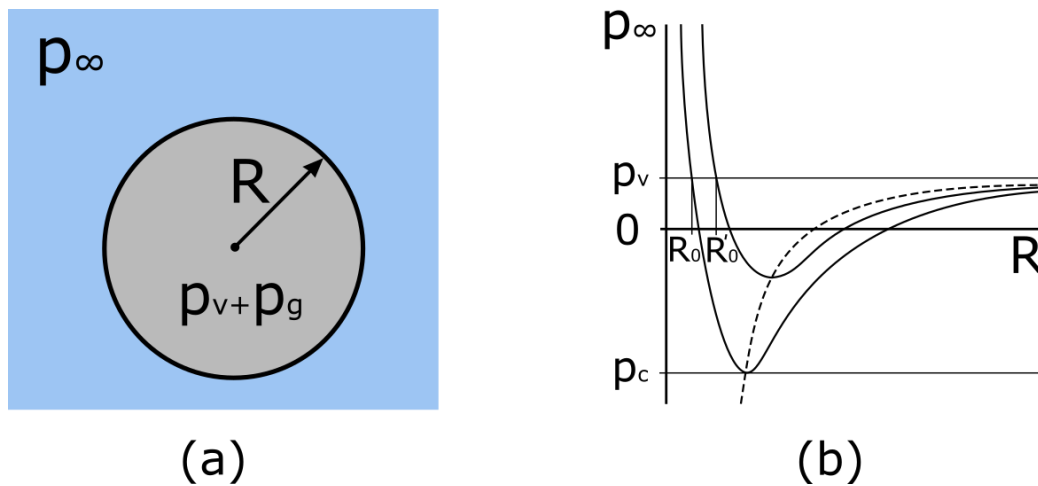

$$(a) \qquad\qquad\qquad\qquad (b)$$

Figure 5:   The stable radii for a bubble with radius R, vapor pressure p_v and gas pressure p_g, which is surrounded by a liquid with the pressure p_∞ (a). Two solid lines indicate stable radii of bubbles with starting radii R_0 and R_0', while the dashed line indicates the locus of minima for all curves (b). For a specific starting radius a critical pressure p_c indicates when no stable situation is available anymore and the bubble causes cavitation.

1.3.2   Air-seeding

The survival of plants at increasingly negative xylem pressures depends on their ability to keep small gas bubbles out of their xylem vessels. This is achieved in the first place by the fact that xylem cells are born wet. Further, water that enters the plant via the roots is subject to filtration in root cell membranes, which are considered to stop air bubbles beyond a critical size from entering the xylem via the roots (Oertli, 1971; Tyree & Sperry, 1989). The most common way through which small air bubbles do enter xylem conduits is from one xylem conduit to another via the pits. This process is referred to as air-seeding. Xylem pits evolved to prevent this leakage of air from embolized conduits,

while they also evolved to allow sufficient water transport through the xylem network. This trade-off makes the pits the weakest part of the hydraulic network with respect to cavitation (Wojtaszek, 2011).

The existence of air-filled xylem conduits, from which emboli spread via the pits at decreasing xylem water potential is considered inevitable. Reasons are events such as leaf abscission, branch breakage, insect feeding or rupture during tissue growth (Sperry, 2011). If air gets sucked from an air-filled conduit into a functional water filled one depends on the size of the pores in the pits. The maximum pressure difference at the air-water-interface $\Delta P_{a/w}$ that is supported by a pore of a certain diameter can again be calculated with the Young-Laplace equation (Eq. 1), scaling with the inverse of the pore diameter.

Accordingly, more than on the dimension of the xylem conduits themselves, the likelihood of air-seeding to occur depends on the pressure difference, as well as the combination of the structure and the number of the pits connecting the conduits (Sperry, 2011). Due to the large number of xylem conduits, arranged in a highly interconnected network, the blockage of individual conduits due to cavitation can be compensated by water taking alternative pathways. If the pressure becomes so low, however, that the spread of emboli reaches a systemic level, the xylem conductivity can be impeded to a agree that poses a threat to plant survival, referred to as catastrophic hydraulic failure (Choat *et al.*, 2012).

1.3.3   Xylem vulnerability curves

The ability of trees to handle drought stress is mostly defined by (i) their capacity to maintain the xylem water potential within functional limits and (ii) the physical limits of the vascular system at declining xylem water potential (Choat *et al.*, 2018). A quantitative measure of the degree to which the xylem is cavitated at a specific xylem water potential is provided by a xylem vulnerability curve. A common method to obtain a vulnerability curve for a particular species is to harvest stem pieces and measure the hydraulic conductivity (K) in dependence of the declining xylem water potential. K is measured as the mass flow rate divided by the pressure difference across the sample (Tyree & Sperry, 1988). After the initial conductivity is measured (K_i) (sample index i), each sample is flushed with degassed water, after which the maximum conductivity is measured (K_{max}). A vulnerability curve is obtained by calculating the percentage loss of conductivity (PLC) via $100*(1-K_i/K_{max})$ (Tyree and Zimmermann, 2002), which results in vulnerability curves scaling from 0% (maximum conductance) to 100% (no conductance, xylem transport stops, Fig. 6). While the method is relatively cheap and easy to perform, care must be taken when sampling stem segments to avoid artificial loss of conductivity due to air being sucked into the xylem when cutting the sample (Tyree and Zimmermann, 2002; Cochard *et al.*, 2013), i.e. by cutting samples under water.

Another commonly used approach to measure vulnerability curves in an invasive manner on cut stem pieces is the centrifuge method. Stem pieces are spun in rotors for the purpose of increasing the tension of the xylem water; the conductivity is measured either in between bouts of spinning (Pockman *et al.*, 1995; Alder *et al.*, 1996) or during spinning (Cochard, 2002), allowing full vulnerability curves to be obtained rapidly from one cut stem sample.

Vulnerability curves usually have a sigmodial shape and the most relevant parameters are the position of the curve, indicating the water potential Ψ_{50} at which the conductivity declined by 50%, and the slope of the curve, which indicates how rapidly the xylem cavitation spreads. A key purpose of vulnerability curves is to find lethal PLC values, which were found to be around 88% in angiosperms (Barigah *et al.*, 2013; Urli *et al.*, 2013), while in gymnosperms lethal values around 50% indicate a higher vulnerability of this xylem architecture (Brodribb & Cochard, 2009).
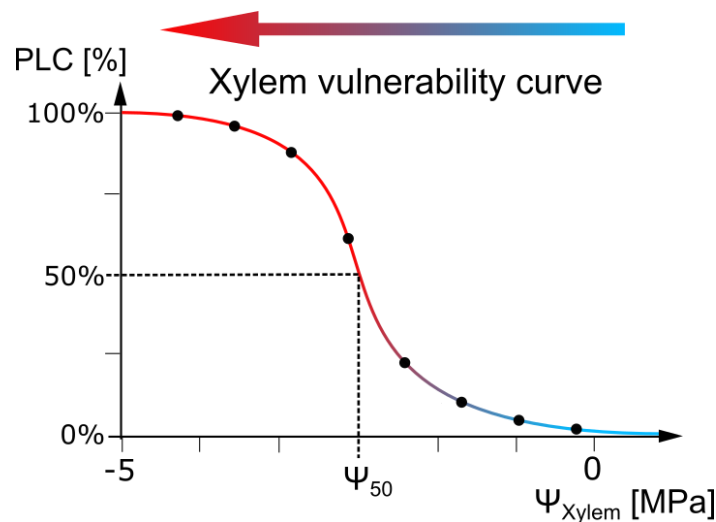

Figure 6:   Illustration of a xylem vulnerability curve. At increasingly negative xylem water potential (Ψ_{xylem}) the xylem loses its function, indicated by the increasing percentage loss of conductivity (PLC). At a PLC of 50% the xylem has lost half of its conductivity, while at a value of 100% the xylem is completely blocked by emboli.

1.3.4   Winter embolism and spring refilling

Besides drought stress, a second common reason for cavitation causing gas bubbles to occur in xylem conduits are freeze-thaw cycles during winter. Cavitation occurring during the thawing phase has been observed in angiosperms and gymnosperms, and is considered an import factor in regions of sub-zero temperatures (see Mayr and Sperry (2010) and literature therein). The reason is that gases are practically insoluble in ice, resulting in gas bubbles to occur during freezing of xylem water. The fate of such gas bubbles can again be described by Eq. 5. (Lipp *et al.*, 1987), indicating the critical water

tension at which the bubble nucleates cavitation to correlate with the inverse of its radius (Sperry & Sullivan, 1992).

As in larger xylem conduits more gas will be released due to freezing of xylem water, species with larger conduits are more susceptible to this type of winter embolism. This is confirmed by conifers with small tracheids (and vessel-less angiosperms) to be hardly susceptible to this type of winter embolism formation, while it is commonly found in species with large vessels (Sperry & Sullivan, 1992; Mayr & Sperry, 2010). Accordingly, temperate growing angiosperm tree species in particular require the ability to recover from winter embolism to support transpiration of new leaves in spring. The two recovery mechanisms in spring that have evolved are (i) refilling of embolized vessels and (ii) growth of new xylem vessels (Cochard *et al.*, 2001). Refilling of vessels at negative xylem pressures is not understood and can be considered a topic under debate, which inspired different theories and research efforts (Zwieniecki & Holbrook, 2009; Brodersen & McElrone, 2013).

Ring-porous angiosperm species with large vessels (such as oak) may have evolved in response to the problem of freezing xylem water. They regrow a ring of large earlywood vessels in late spring, on which they mainly rely for water transport until the first frost in autumn (Sperry, 2011). In diffuse-porous to semi-ring porous beech (Schweingruber, 1990) both types of xylem recovery mechanisms were observed. Active refilling occurred mostly in the roots and the trunk, while new functional vessels were observed to form mainly in young terminal shoots (Cochard *et al.*, 2001).

1.4   Existing non-invasive methods to monitor xylem functionality

Vulnerability curves are the most important measure to investigate and compare how different plant species cope with drought and limited water supply, and are therefore considered 'at the heart of plant hydraulics' (Venturas *et al.*, 2017). The accuracy of invasive methods (using cut stem pieces) to measure the decline in xylem conductivity, however, has been debated extensively. The reason is, in essence, that the xylem water is under tension. Therefore, any incision or cut can result in air being sucked into the xylem and cause artificial xylem emboli. Another problem can be artificial refilling of existing emboli, when trying to prevent air from being sucked into the cut xylem. Numerous contributions illustrate the discussion on (i) air entering the sample subsequent to its incision, causing a 'cutting artefact' (Wheeler *et al.*, 2013; Venturas *et al.*, 2015), (ii) artificial refilling due to xylem tension relaxation procedures prior to the measurement (Trifilò *et al.*, 2014; Hochberg *et al.*, 2016b), and air entering the xylem during the measurement in the form of an 'open vessel artefact' when using the centrifuge method (Jacobsen & Pratt, 2012; Sperry *et al.*, 2012; Tobin *et al.*, 2013; Torres-Ruiz *et al.*, 2014; Hacke *et al.*, 2015).

The need to validate standard hydraulic methods with appropriate control experiments has been referred to as the single most limiting factor to progress in the field of plant hydraulics (Sperry, 2013).

Therefore, efforts were made to develop less invasive methods for monitoring xylem functionality. Examples of cheap and relatively easily implemented approaches are the use of acoustic emissions (Jackson & Grace, 1996; Rosner *et al.*, 2006), which are considered to be caused by water columns breaking, and a more recently developed optical approach (Brodribb *et al.*, 2017). While both methods have been shown to be capable to obtain VCs, neither of them allows to accurately spatially resolve the emergence of emboli in the xylem. The ability to obtain more accurate information on where emboli form in the xylem in a non-invasive manner is only provided by more sophisticated imaging approaches such as neutron radiography (Tötzke *et al.*, 2013), high resolution computed tomography (HRCT) or MRI. While technologies of this kind are costly and more difficult to operate, they are expected to resolve open questions around xylem dry-down, such as embolism repair, plasticity and xylem redundancies (Melcher *et al.*, 2003).

The most compelling argument for HRCT is the high spatial resolution down to a few mircometers, allowing to resolve individual xylem vessels (Brodersen *et al.*, 2010; Brodersen *et al.*, 2011). Xylem VCs were successfully obtained (Brodersen *et al.*, 2013; Choat *et al.*, 2016) and HRCT was used as a reference technology to validate whether invasive hydraulic methods are affected by artefacts (Cochard *et al.*, 2015; Nardini *et al.*, 2017). Also, HRCT has been used more frequently in plant hydraulics since affordable desktop devices can be purchased (Torres-Ruiz *et al.*, 2014; Cochard *et al.*, 2015; Nolf *et al.*, 2017).

Besides the fact that until now it cannot be used in the field, an important drawback of HRCT is the use of ionizing radiation, which may result in damage of living tissue in different ways (Dhondt *et al.*, 2010; Savi *et al.*, 2017; Petruzzellis *et al.*, 2018). Such effects may be less of a problem when imaging the xylem, as it mainly contains non-living cells. Depending on the sample size and the spatial resolution, however, at higher numbers of exposures the non-invasiveness of HRCT should be questioned. Details on this issue are provided in the context of desktop HRCT devices by Suuronen *et al.* (2013), who concluded that the radiation dose may be the biggest drawback of the technology, making it inappropriate for long-term and continuous measurements.

1.5   Magnetic resonance imaging

In this thesis the use of magnetic resonance imaging (MRI) for the purpose of monitoring the emergence of xylem emboli in small trees in vivo is investigated. In the following the basic principles of the technology, necessary to follow the publications and discussion, are outlined.

1.5.1   Spins and sample magnetization

Spin is a basic property of individual electrons, neutrons and protons. In an atomic nucleus two particles of opposite spin typically pair up, resulting in a net spin of zero. Specific atomic nuclei,

however, have a nonzero net spin due to unpaired protons or neutrons, including hydrogen, which has an individual proton as its nucleus. In a simplified model, the phenomenon of nuclear magnetic resonance (NMR) originates from a tendency of those specific nuclei to align themselves with external magnetic fields (B_0), similar to a compass needle, due to their magnetic moment. In an MRI scanner the external magnetic field B_0 is typically provided by a superconducting, resistive or permanent magnet. Subsequent to aligning themselves with the field direction, the nuclei rotate (or precess) parallel or anti-parallel to the direction of B_0, the majority being in the energetically favorable parallel state. The frequency of this precession (also referred to as the Larmor frequency ω_0) relates linearly to the local magnetic field, as expressed in the fundamental NMR equation (Larmor equation)

$$\omega_0 = \gamma B_0 \quad .$$

(6)

The Larmor frequency ω_0 and the magnetic field are related via the gyromagnetic ratio γ, which is element specific and has the highest value for hydrogen nuclei or protons (of all stable nuclei) of $\gamma_H = 2\pi*42.6$ MHz/T. This makes hydrogen a natural choice for NMR and MRI experiments, together with its abundance in water.

The tendency of the individual magnetic moments to align with an external magnetic field results in a net magnetization of the sample M_0 in the direction of B_0, which scales with the spin density (the number of protons per unit volume, ρ_0) and the field itself

$$M_0 = \frac{\rho_0 \gamma^2 \hbar^2 B_0}{4 k_B T} \quad .$$

(7)

Besides $\hbar^2$ (the Planck constant squared and divided by π), M_0 also scales with the inverse of the sample temperature (T), multiplied with the Boltzmann constant (k_B). This is due to the interaction of the spins with each other and their surroundings, which increases with rising temperature and counteracts the spin alignment (Brown *et al.*, 2014).

1.5.2 Radio frequency pulses and signal acquisition

The sample magnetization M_0 cannot be utilized in the form of a signal due to the presence of B_0 in the same direction. To generate a signal that can be detected, the direction of the magnetization is temporally moved out its equilibrium direction by means of a magnetic field that is alternated at the Larmor frequency. This alternating magnetic field B_1 is oriented perpendicular to B_0 and produced by a radio frequency (RF) coil. B_1 causes a sample magnetization with a non-zero component $M_\perp$ perpendicular to B_0. If B_0 points in the z direction, the perpendicular component $M_\perp$ can be expressed by a complex number according to its orientation in the xy-plane (Fig. 7)

$$M_\perp = \cos(\omega_0 t + \phi)M_x + i\sin(\omega_0 t + \phi)M_y \quad .$$

(8)

The alternating B_1 fields are pulsed and referred to as excitation pulses, which are named in accordance with the angle they cause the magnetization to rotate by. Commonly used are 90 and 180 degree pulses.
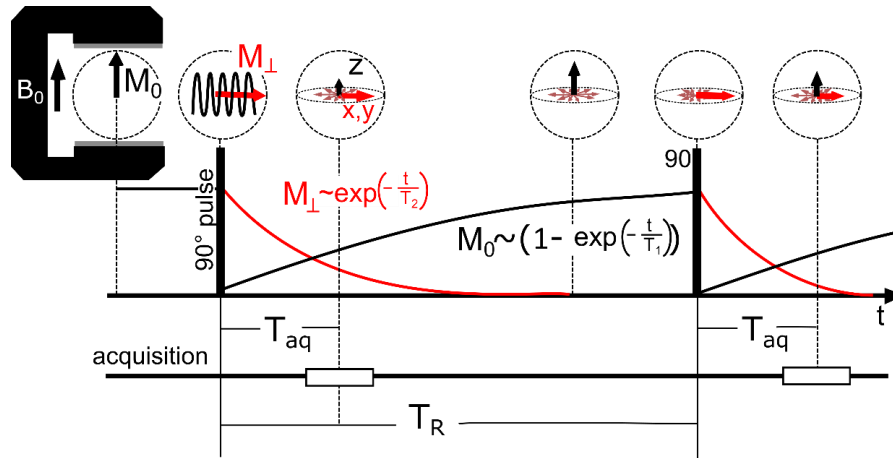

Figure 7:   Time dependency of the net sample magnetization, which starts out in the direction of B_0 (z-direction). The component of the sample magnetization in B_0 direction is referred to as M_0 (black curve). By means of a 90 degree radio frequency (RF) excitation pulse the net magnetization is flipped into the xy-plane. The component of the magnetization perpendicular to B_0 in xy-direction is referred to as $M_\perp$ (red curve), and can be detected as an RF signal, which is acquired during the acquisition time T_{aq} by an RF coil and is subject to exponential spin-spin relaxation (relaxation time T_2). Due to spin-lattice processes the net sample magnetization is restored in z-direction (relaxation time T_1). Another 90 degree pulse is applied to flip the signal back into to xy-plane after the repetition time T_R.

After signal excitation, the perpendicular magnetization component $M_\perp$ can be detected by an RF coil as a signal in the form of an alternating voltage. When ignoring spatial dependencies, this signal S is proportional to $\omega_0 M_0$, resulting in the following dependencies (Brown *et al.*, 2014)

$$S \propto \frac{\rho_0 \gamma^3 B_0^2}{T} \qquad (9)$$

.

1.5.3 Signal decay due to relaxation: T_1 and T_2

The time dependency of $M_\perp$ is illustrated in Fig. 7. Due to spin-spin interactions the detectable magnetization $M_\perp$ decays as a function of time t, according to the relaxation time constant T_2

$$M_\perp(t) = M_\perp(0) \exp\left(-\frac{t}{T_2}\right) \qquad (10)$$

.

Spins not only interact with each other, but also with their surroundings. This interaction is referred to as spin-lattice interaction and causes the magnetization to realign with B_0 according to the relaxation

time constant T_1. Therefore, when exciting the sample twice (or multiple times) in a row by means of 90 degree pulses (as normally done in MRI), the total detectable signal at the second or later signal acquisition depends on both relaxation time constants (T_1 and T_2), when the signal is acquired (t) and the time between excitations, called repetition time (T_R)

$$M_\perp(t) = M_\perp(0) \left(1 - \exp\left(-\frac{T_R}{T_1}\right)\right) \exp\left(-\frac{t}{T_2}\right) \qquad (11)$$

.

Accordingly, the time between signal excitation (with a 90° pulse) and signal acquisition should be chosen as short as possible to avoid signal decay before signal acquisition. If the aim of an experiment is to quantitatively measure proton density, then the repetition time T_R should be chosen long enough so that the magnetization is completely aligned with B_0 before the next excitation. In an MRI experiment $M_\perp$ can be determined for the purpose of measuring the sample's water content (as a function of proton density), but also the relaxation time constants T_1 and T_2 can be probed and provide insights about the sample's physicochemical properties, proton mobility or the liquid composition (Eq. 11).

1.5.4   Signal decay due to B_0 and susceptibility inhomogeneities

The signal not only decays due to stochastic spin-spin interactions within the sample (described by what can be called the 'true' T_2 value), but also due to non-moving spins experiencing slightly different magnetic fields (described by T_2'). There are different reasons for spins to experience different magnetic fields, such as inhomogeneities of the main magnetic field B_0 and inhomogeneities of the magnetic susceptibility of the sample. In the context of this thesis it is relevant that small permanent magnets in particular only offer limited field homogeneity, and that susceptibility inhomogeneities are particularly relevant in desiccating plant xylem, since the area of water-air-interfaces increases.

The observed total decay time is the reciprocally added combination of T_2 and T_2' processes, referred to as T_2* (Brown *et al.*, 2014)

$$\frac{1}{T_2^*} = \frac{1}{T_2} + \frac{1}{T_2'} \qquad (12)$$

.

When assuming that the change of the magnetic field is linear within the volume of interest, the decay constant T_2' of the signal that originates from this volume depends on the field inhomogeneity experienced by the spins (ΔB_{inhom}) across this volume as follows (Chavhan *et al.*, 2009)

$$T_2' = \frac{1}{\gamma \, \Delta B_{inhom}} \qquad (13)$$

.

T_2' type of processes (signal decay due to non-moving spins experiencing different magnetic fields) are treated separately in terms of T_2 because their effects can be reversed and cancelled by applying a 180

degree RF refocusing pulse, subsequent to a 90 degree excitation pulse (Hahn, 1950). This causes the occurrence of what is called a spin echo. The technique is also referred to as refocusing the signal.

1.5.5   Multiple spin echoes and quantitative imaging

Besides the reversal of T_2' signal decay, there are benefits of refocusing the signal more than once per one excitation by means of multiple spin echoes. If it is refocused successfully, the signal can be acquired subsequent to each refocusing pulse. Exponential fitting of the resulting curve of echo amplitudes allows for quantitatively probing the water content and the true T_2 value (not affected by T_2') of each pixel, with fit parameters being M_0 and T_2 (Eq. 10). Quantitative imaging refers to obtaining MR images in which pixel values directly relate to physical sample quantities, such as the proton density and the signal relaxation times (T_1, T_2) (van As *et al.*, 2009).

(a)   (b)
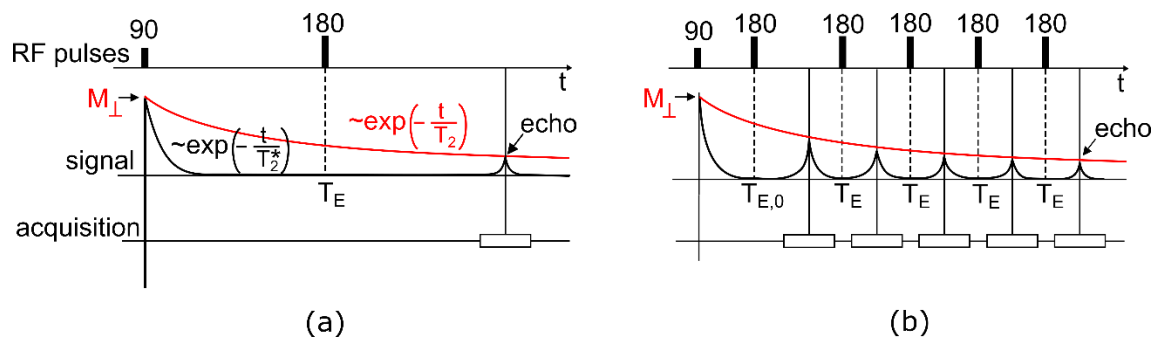
Figure 8   Comparison of a single-spin echo (SSE) (a) and multi-spin echo (MSE) (b) imaging pulse sequence. In both cases (SSE and MSE) the sample is excited by means of a 90 degree pulse, after which the signal decays according to the relaxation time T_2, reflecting physicochemical sample characteristics and proton mobility in the sample. In a SSE pulse sequence the signal is refocused by means of a single 180 degree pulse, and acquired after a certain echo time (T_E). In a MSE pulse sequence the signal is refocused and acquired many times per excitation and T_E is typically chosen shorter.

Besides imaging quantitatively, another important advantage of acquiring the signal many times per excitation instead of only once is a more efficient use of measurement time, which is especially valuable when B_0 and therefore the inherent signal-to-noise ratio (SNR) of an NMR measurement is low (Callaghan, 1991). Relatively low magnetic fields (0.25 to 1 Tesla) are a property of mobile permanent magnets, compared to stationary superconducting ones. The difficulty of using a multi-spin echo (MSE) type of pulse sequence, however, is the cumulative effect of small turn angle errors of the magnetization (which cause what is referred to as stimulated echoes), caused by small errors in the 180 degree pulses. This problem can be solved by periodically altering the relative orientation of

successive 180 degree pulses in the xy-plane and the receiver orientation. This approach, referred to as phase cycling, adds up spin echoes, while the unwanted stimulated echoes cancel each other.

Phase cycling patterns for the purpose of NMR (non-imaging) have been developed by H. Y. Carr and E. M. Purcell (1954) and Meiboom and Gill (1958) (CPMG). For imaging applications the presence of field gradients (see the next section) poses a particular challenge for acquiring accurate T_2 images (Poon & Henkelman, 1992). On the basis of specific phase cycling patterns, these problems have been solved for the purpose of imaging water content and T_2 in plants quantitatively (Edzes *et al.*, 1998), as well for the purpose of combining fast imaging and flow (Scheenen *et al.*, 2000).

1.5.6   Spatial encoding with magnetic field gradients

The NMR principle can be utilized to obtain the spatial distribution of the spins in one or more directions, referred to as MR images in case of a 2D distribution. For this purpose, switched linear magnetic field gradients ($G_{x,y,z}$) in different directions are superimposed on top of B_0 and B_1 to spatially define or encode the sample magnetization. This is done by gradient coils that are positioned within the magnet and typically outside of the receiving RF coil.

In 2D imaging mode and when obtaining an image in the xy-plane, in the z-direction a slice encoding gradient G_z is present during the 90 degree pulse. This results in the resonance condition (Eq. 6) to only apply to the spins within a particular slice thickness (TH), depending on the spectral width (SW), which is the frequency window chosen to be picked up by the RF coil. Accordingly, the slice thickness (TH) can be chosen by adjusting those corresponding parameters

$$TH = \frac{\text{SW}}{\gamma\, G_z} \qquad (14)$$
.

Spatial encoding in the x-direction is achieved by superimposing a frequency or read gradient during signal acquisition, which result in a spatial dependency of the Larmor frequency in the corresponding direction

$$\omega_0(x) = \gamma_H(B_0 + G_x x) \qquad (15)$$
.

The frequency interval of a pixel $\Delta\omega_{pix}$ is determined by the gradient strength G_x, the pixel width in real space Δx in the encoding direction and the gyromagnetic constant γ

$$\Delta\omega_{pix} = \gamma\, G_x\, \Delta x \qquad (16)$$
,

and must not be exceeded by the inhomogeneity of the magnet (ΔB_0) over the same distance.

Spatial encoding in the y-direction is achieved by applying a phase gradient pulse G_y in between the excitation and the acquisition of the signal for the duration of t_y, which causes $M_\perp$ to pick up a position (y) dependent phase

$$\phi(y) = \gamma_H \; y \; G_y \; t_y \quad \cdot \tag{17}$$

This step is repeated N_{ph} times with different phase gradient values. The linear relation of phase and position is utilized for obtaining an image with N_{ph} pixels in y direction.

Frequency and phase encoding together result in $M_\perp$ to have a spatial dependency in two directions, which results in the following term for the signal

$$S \propto \int \int dx \; dy \; M_\perp(x,y) \exp(i \; (\omega(x) \; t + \phi(y))) \quad \cdot \tag{18}$$

Right after applying an ideal 90 degree pulse $M_\perp$ equals M_0, which in turn is proportional to the spin density. Therefore, a 2d Fourier transform (2DFT) of the signal results in a function for the spin density in the xy-plane

$$\rho(x,y) \propto 2DFT_{\omega\phi}(S) \quad , \tag{19}$$

which in z-direction is limited to the slice thickness and can be plotted as a 2D MR image.

1.5.7   Using T_2 to probe the internal sample structure

In plants cells the largest vacuoles and conduits with the widest diameters give rise to the longest T_2 relaxation times. The T_2 of the bulk liquid is up to 2 s for pure water, whereas narrow pores, conduits or small cells give rise to T_2s that are much smaller (tens of milliseconds). The true relaxation time constant is the result of molecular processes which can be subdivided into three different kinds. They are the intrinsic or bulk relaxation of the fluid, surface relaxation processes and relaxation due to diffusion

$$\frac{1}{T_2} = \frac{1}{T_{2,bulk}} + \frac{1}{T_{2,surf}} + \frac{1}{T_{2,diff}} \quad . \tag{20}$$

At decreasing lumen size, due to the growing surface-to-volume ratio, the influence of surface relaxation processes grows. Therefore, the dimensions of the sample structure that the water is contained by can be probed on the basis of T_2. This principle is used in well logging (probing subsurface properties with low-field sensors that are lowered into a bore hole) for measuring the porosity, permeability and other quantities of sandstone (Kleinberg, 1999).

For living plant tissue the correlation between the sample structure and the observed T_2 has been tested in different crops by van der Weerd *et al.* (2001). They also successfully modeled the correlation between the observed $T_{2,obs}$ and the structural dimensions of living plant tissue, assuming the plant cells to be ellipsoidal (with radii $R_{x,y,z}$), on the basis of the following equation

$$\tag{21}$$

$$\frac{1}{\text{T}_{2,obs}} = H\left(\frac{1}{R_x} + \frac{1}{R_y} + \frac{1}{R_z}\right) + \frac{1}{T_{2,bulk}} \quad,$$

with the sink strength density H, which was found to be proportional to membrane permeability (Snaar & H. Van As, 1992). The more general form of Eq. 21 had been stated by Brownstein and Tarr (1979), using the surface to volume ratio (S/V)

$$\frac{1}{\text{T}_{2,obs}} = H\frac{S}{V} + \frac{1}{T_{2,bulk}} \quad. \tag{22}$$

1.5.8   Signal decay due to diffusion

Besides T_2- and T_2'-processes, another type of signal decay process that causes signal attenuation, but other than T_2'-processes cannot be compensated by the use of 180 degree pulses, is the diffusion of water molecules (i.e. spins) through local magnetic field gradients. Such field gradients can be inhomogeneities of B_0, magnetic susceptibility inhomogeneities or imaging gradients that are used to spatially encode the signal. Attenuation caused by water molecules diffusing through field and susceptibility inhomogeneities scales with the product of the spin diffusion constant and the echo time squared. Accordingly, signal decay due to diffusion is significantly decreased by using short echo times. In plants, especially when drying down, susceptibility inhomogeneities at air-water-interfaces are a major cause of signal attenuation. Since the mean square distribution of local magnetic field gradients relates to B_0^2 (Edzes *et al.*, 1998), lower field strengths have been shown to result in longer observed T_2 values in the same cherry tree stem (Homan *et al.*, 2007). Attenuation caused by diffusion through imaging gradients scales with $D/\Delta x$ (where D is the spin diffusion constant, and Δx pixel size) and is therefore negligible at pixels sizes beyond 100 µm (Edzes *et al.*, 1998).

1.6   Motivation and thesis objectives

Due to shifts in temperature and precipitation patterns (Dai, 2013; Trenberth *et al.*, 2014), forests worldwide are expected to experience an increase in duration and frequency of drought events, potentially resulting in widespread forest dieback. Some of the worlds forested ecosystem have been found to already respond to climate change with higher background tree mortality rates (Allen *et al.*, 2010; Williams *et al.*, 2013; Brodribb *et al.*, 2020; Schuldt *et al.*, 2020).

Trees and forests are relevant for human life in ways that far exceed their economic value. Wood serves as an energy source and building material, but on a global scale forests are also critical for biodiversity (Gibson *et al.*, 2011), and are considered a global carbon sink with the potential to reduce the rising atmospheric CO_2 levels (Keenan & Williams, 2018). Also, forests have a major impact on global water cycles, as transpiration from plants plays a major role in returning precipitation back to the atmosphere (Schlesinger & Jasechko, 2014). Besides threatening the earths largest land ecosystems, extensive forest dieback may therefore also result in atmospheric and hydraulic feedback loops with unpredictable consequences.

To estimate the potential effects of different drought scenarios for forested ecosystems a better understanding is required of how drought stress causes plant death. The question is a complex one, as the response of plants has to be taken into account in terms of water potentials, metabolism, stomatal conductance and others, when plants face decreasing soil water potential and high transpiration rates, as well as pathogens (Brodersen *et al.*, 2019). Hydraulic failure, i.e. the breakdown of the xylem transport process to a life threatening degree, however, is considered the lethal breaking point of many tree species (Tyree and Zimmermann, 2002; McDowell *et al.*, 2008; Choat *et al.*, 2012). A more detailed understanding of how anatomical traits (i.e. conduit number, size and connectedness) relate to xylem vulnerability are relevant for the development of comprehensive hydraulic models of plants (Papastefanou *et al.*, 2020). This may provide the ability to choose species and varieties that are better able to withstand climate change and drought.

MRI offers a number of unique opportunities to study water dynamics in plant xylem non-invasively. In contrast to HRCT and neutron radiography, obtaining information about the interior of the sample does not rely on the sample absorbing high-energy photons or neutrons. Instead, by fulfilling the resonance condition, the protons of the water in the sample are caused to coherently emit an NMR signal, which carries information about this water, as well as the sample structure. This can allow for quantitative imaging, which refers to pixel values that directly relate to individual physical sample parameters. Examples are the proton density, which has been used to monitor the water content of different plant tissues (Schepper *et al.*, 2012; Robert *et al.*, 2014), while the signal decay time (T_2) has been linked successfully to the xylem anatomy of cherry trees (Homan *et al.*, 2007) and poplar (Windt

et al., 2007). MRI is capable of acquiring sub-pixel information, as pixel values reflect information on the sample geometry, even if this geometry is not resolved spatially. Depending on the context and research question at hand, this aspect has the potential to compensate for the limited spatial resolution MRI provides.

A particular advantage of MRI over HRCT is the ability to do high numbers of repeated measurements on the same sample, as in most cases the sample energy deposition of MRI can be considered negligible. An open question that may benefit from the ability to do repeated measurements is if plants can adapt to drought stress (plasticity, Anderegg, 2015). The ability to monitor xylem dry-down development and spread of emboli at high time resolution has been illustrated in grapevine (Holbrook *et al.*, 2001; Hochberg *et al.*, 2016a) and acer (Zwieniecki *et al.*, 2013), and in the future may help to answer the question how some plants are able to refill conduits despite substantial negative xylem pressure (Brodersen & McElrone, 2013).

Accordingly, MRI offers unique advantages over approaches such as HRCT and neutron radiography, namely the ability to measure water content, diffusion times and other parameters directly, quantitatively and with a negligible sample energy deposition. Those advantages are utilized routinely in medical MR imaging and their potential for studying xylem desiccation in vivo has been illustrated for angiosperms with large vessels (Holbrook *et al.*, 2001; Clearwater & Clark, 2003; Kaufmann *et al.*, 2009; Choat *et al.*, 2010; Hochberg *et al.*, 2016a), but also in different tree species without xylem conduits being spatially resolved (Utsuzawa *et al.*, 2005; Zwieniecki *et al.*, 2013; Fukuda *et al.*, 2015; Umebayashi *et al.*, 2016). The latter was done by utilizing pixel values as a proxy measure of the percentage of embolized xylem.

Accordingly, the potential to use MRI in the context of monitoring xylem dry-down has been shown in a fair number of studies. The technology, however, is far from being used routinely for this purpose. The main reasons are that affordable, plant-suitable MRI scanners and imaging methods are largely unavailable. Most MRI scanners are designed under the assumption that the machine will not be moved, and that it will be used in an environment that is temperature stable and shielded from electromagnetic noise. The use of smaller, dedicated and open scanners, that are based on small permanent magnets, has been limited to experts who are able to modify and build their own imaging equipment (Rokitta *et al.*, 2000; Fukuda *et al.*, 2007; Kimura *et al.*, 2011). Existing approaches to use MRI scanners in the field require significant effort to move the machine about and set it up, due to the size and weight of the magnet (Jones *et al.*, 2012; Nagata *et al.*, 2016), as well as the different electronic components that are required for MR imaging (Kimura *et al.*, 2011).

This thesis addresses some of the key challenges that prevent the broader use of MRI to image embolism formation in tree xylem. This is done by designing custom MRI hardware, and programming dedicated image acquisition software and data evaluation routines specifically for this purpose. It was tested if imagers can become significantly smaller and lighter, while still providing in vivo images of high anatomical detail, ideally in the field.

To this end, the following hypotheses are investigated and discussed:

I.   The use of a multi-spin echo imaging pulse sequence compensates for the imperfect homogeneity and lower field strength of small-scale and open permanent magnets.

II. Quantitative MR imaging allows the detection and visualization of xylem emboli, even if xylem conduits are not spatially resolved.

III. Xylem vulnerability curves can be obtained from quantitative water content and T_2 images.

IV. All imaging components can become sufficiently small and robust for imagers to be easily moved, set up and used in a greenhouse or in the field.

2 Integration of first authorship publications

2.1 Publication I: A small-scale MRI scanner and complementary imaging method to visualize and quantify xylem embolism formation

Marco Meixner, Martina Tomasella, Petra Foerst, Carel Windt

Background

Magnetic resonance imaging is rarely used in the field of plant hydraulics, despite different benefits and its successful use for imaging xylem embolism formation in vivo in different studies. A major reason is that affordable, small and plant suitable imagers are not commercially available. In this paper a novel magnetic resonance imaging approach was tested in the context of visualizing the formation of xylem emboli in young trees. A small and open permanent magnet was paired with a set of open, custom-made imaging gradients. The magnet was sufficiently light and small to be mounted on the stem of young trees in between branches and leaves with little effort. The two main drawbacks of using a small open magnet are low field strength and poor homogeneity of the magnetic field. It was examined if those limitations can be compensated to a sufficient degree by using strong custom-made gradient coils and a multi-spin echo imaging pulse sequence. The imaging approach was tested by non-invasively monitoring the stems of young beech trees that were bench dehydrated inside the magnetic resonance imaging system. Subsequent to the dry-down experiments, microscopy images were obtained at the position where the magnetic resonance imaging had been conducted.

Results

The benefits of using a multi-spin echo imaging pulse sequence with a large number of echoes and short echo times was found to be beneficial in three different ways when using a small open magnet. The low signal amplitude was compensated as the signal was picked up as often as possible per excitation. The short signal decay time (due to the low field homogeneity) was compensated as the signal was rapidly refocused. Finally, the ability to obtain and fit a signal decay curve for every pixel allowed to obtain quantitative water content (A) and T_2 parameter images, as well as $A*T_2$ product images via pixelwise multiplication.

All three types of images were utilized to detect the cavitation of xylem vessels in beech, despite the fact that those vessels could not be spatially resolved. T_2 images showed higher sensitivity to a limited number of vessels drying down in a pixel. By means of a simulation this effect was shown to be caused by the longer T_2 values of water in larger lumina. Xylem vulnerability curves were successfully obtained on the basis of binarizing water content and $A*T_2$ product images; the latter approach yielded slightly

more accurate sigmodial fits than the former. Both approaches were in agreement with beech vulnerability curves from literature.

Author contributions

Marco Meixner and Carel Windt designed, built and programmed the magnetic resonance imager. Marco Meixner performed the experiments and analyzed the data. Martina Tomasella prepared the anatomical sections and microscopic images. Marco Meixner and Carel Windt wrote the manuscript with contributions from Petra Foerst and Martina Tomasella.

A small-scale MRI scanner and complementary imaging method to visualize and quantify xylem embolism formation

Marco Meixner[1,2] (iD)**, Martina Tomasella[3,4]** (iD)**, Petra Foerst[1]** (iD) **and Carel W. Windt[2]** (iD)

[1]Process Systems Engineering, Technical University of Munich, Gregor-Mendel-Straße 4, 85354 Freising, Germany; [2]IBG-2: Plant Sciences Institute, Forschungszentrum Jülich, Leo-Brandt-Straße 1, 52428 Jülich, Germany; [3]Chair for Ecophysiology of Plants, Technical University Munich, Hans-Carl-von-Carlowitz-Platz 2, 85354 Freising, Germany; [4]Dipartimento di Scienze della Vita, Università di Trieste, Via L. Giorgieri 10, 34127 Trieste, Italy

Summary

Author for correspondence:
Carel W. Windt
Tel: +49 2461 613256
Email: c.windt@fz-juelich.de

- Magnetic resonance imaging (MRI) is a useful tool to image xylem embolism formation in plants. MRI scanners configured to accept intact plants are rare and expensive. Here, we investigate if affordable small-scale, custom-built low-field MRI scanners would suffice for the purpose.
- A small-scale, C-shaped permanent magnet was paired with open, plane parallel imaging gradients. The setup was small enough to fit between leaves or branches and offered open access for plant stems of arbitrary length. To counter the two main drawbacks of the system, low signal to noise and reduced magnetic field homogeneity, a multi-spin echo (MSE) pulse sequence was implemented, allowing efficient signal acquisition and quantitative imaging of water content and T_2 signal relaxation.
- The system was tested visualizing embolism formation in *Fagus sylvatica* during bench dehydration. High-quality images of water content and T_2 were readily obtained, which could be utilized to detect the cavitation of vessels smaller than could be spatially resolved. A multiplication of both map types yielded images in which filled xylem appeared with even greater contrast.
- T_2 imaging with small-scale MRI devices allows straightforward visualization of the spatial and temporal dynamics of embolism formation and the derivation of vulnerability curves.

Introduction

As a result of shifts in temperature and precipitation patterns, forests worldwide are expected to experience an increase in duration and frequency of drought and widespread forest dieback events (Dai, 2013; Park Williams *et al.*, 2013; Trenberth *et al.*, 2014). One of the main causes of drought-induced tree mortality is thought to be embolism formation, resulting in reduced xylem conductivity and, ultimately, hydraulic failure (McDowell *et al.*, 2008; Choat *et al.*, 2018). While there is a good basic understanding of, and a large body of literature on, xylem embolism formation, most of it is based on results obtained by means of invasive methods, applied to excised stem pieces. Only in recent decades have noninvasive imaging methods emerged that allow the spatially explicit visualization of the dynamics of xylem embolism formation and spread (Fukuda *et al.*, 2015).

High-resolution computed tomography (HRCT) is currently the most used noninvasive method and is known for the excellent resolution that it affords (Choat *et al.*, 2016). It has, for instance, been shown to be capable of fully resolving individual xylem vessels in three dimensions (3D; Brodersen *et al.*, 2010, 2011; Choat *et al.*, 2016). However, an important drawback of HRCT is the

use of ionizing radiation. It was found to damage living tissue (Savi *et al.*, 2017) and cause growth inhibition (Dhondt *et al.*, 2010) and disruption of cellular function (Petruzzellis *et al.*, 2018). It is thus less suitable for long-term repeated observations or for investigations of recovery, even though current evidence suggests that xylem vulnerability *per se*, as it primarily depends on the integrity of the dead xylem structure rather than on its living cells and surroundings, is not easily affected by HRCT.

Magnetic resonance imaging (MRI, also known as nuclear magnetic resonance (NMR) imaging) is unusual in that it does not, in contrast to most other imaging or sensing methods, image the absorption of radiation in the visible or X-ray domain. Inside an magnetic resonance (MR) magnet, protons in water within a sample can be excited to emit a weak radio signal. The latter is achieved by means of radio frequency (RF) signals of an appropriate frequency and amplitude, neither damaging nor appreciably heating up the sample. MRI is thus well suited for continuous or long-term measurements. The technology has been used to image structure and anatomy (Robinson *et al.*, 2000; Metzner *et al.*, 2014; Hesse *et al.*, 2018), plant water content (Schepper *et al.*, 2012), and to measure phloem and xylem sap flow (Köckenberger *et al.*, 1997; Scheenen *et al.*, 2000; Windt *et al.*, 2006). For detailed reviews and

more examples see van As *et al.* (2009) and Borisjuk *et al.* (2012). In the scope of plant hydraulics, MRI has been used to study embolism formation (Choat *et al.*, 2010; Fukuda *et al.*, 2015), refilling (Holbrook *et al.*, 2001), hydraulic vulnerability segmentation (Hochberg *et al.*, 2016) and the spread of disease in the xylem (Utsuzawa *et al.*, 2005).

In the context of embolism formation, large high field stationary imagers based on superconducting or resistive magnets have been employed to study grapevine (Holbrook *et al.*, 2001; Choat *et al.*, 2010; Hochberg *et al.*, 2017), woody lianas (Clearwater & Clark, 2003), maple (Zwieniecki *et al.*, 2013) and various herbaceous species (such as the stem of cucumber by Scheenen *et al.* (2007), roots of maize by Ilja Kaufmann *et al.* (2009) and tomato pedicel by van de Wal *et al.* (2017)). However, despite their proven utility, large stationary MRI scanners that are suitable for imaging living plants are rare. The problem is not only the significant cost of such systems, but also the fact that most imagers have an unfavorable hardware configuration. The most limiting factors are: the inaccessibility of the magnet for intact plants (e.g. bore not wide enough, bore horizontal instead of vertical, isocenter not accessible for other reasons); the strength and accessibility of the imaging gradients (imaging gradients do not offer access or cannot be opened, maximum gradient strength too low for microimaging of small samples); or size and accessibility of the RF coil (coil too large relative to the sample to achieve a satisfactory signal-to-noise ratio, coil cannot be split to accept long samples such as stems). For these reasons, imaging plants has so far remained the domain of laboratories that have the technical knowhow to modify their equipment to match the geometry of the plant organ of interest and research question at hand.

Small-scale imagers based on permanent magnets have the potential to make MRI of plants much more affordable and can be tailored for use on plant stems (van As & van Duynhoven, 2013). C-shaped magnets (Umebayashi *et al.*, 2011; Lechthaler *et al.*, 2016) or ring-shaped Halbach magnets that can be opened from the side (Windt & Blümler, 2015) may be especially well suited to image plants. Indeed, a number of such imagers have already been applied to study xylem embolism formation and pine wilt disease (Umebayashi *et al.*, 2011; Fukuda *et al.*, 2015; Ogasa *et al.*, 2016; Umebayashi *et al.*, 2016).

The technology to make small-scale imagers more broadly available thus seems within reach. However, so far, most small-scale MRI scanners still appear to be based on design principles from medical imaging. They employ strong and highly homogeneous magnets, relatively weak imaging gradients, and run single-spin echo (SSE) imaging sequences (i.e. a sequence of commands to operate an MRI scanner; see Fig. 1) with very long echo times. These specifications are optimal for applications on animals or humans, but will have drawbacks for applications on plants. Highly homogeneous magnets have desirable traits: they allow imaging with narrow spectral widths, thus reducing external RF noise; they permit the use of weak imaging gradients, as a result of which gradients can be large and wide, and gradient amplifiers need only modest power; and they allow 3D and multi-slice imaging over large fields of view. However, they will also be wider, heavier and more costly, or have a smaller air gap than is optimal to allow access to plants. Further, their wide but slow

gradients may limit the types of imaging sequences that they can run. SSE has been used by all small-scale MRI studies of plants to date, but in that application it has many drawbacks. Advantageous properties of SSE are that it is robust, does not require fast gradient switching and allows for easy implementation of multi-slice imaging: it is one of the most efficient ways to image a 3D volume with optimal signal to noise. However, in plant stems where 3D imaging is not needed, SSE mainly has drawbacks. In single slice mode it inefficiently samples the available NMR signal (Fig. 1). Furthermore, especially if acquired with long echo times, the resulting images will not only be weighted by water content, but also by tissue-dependent differences in signal relaxation (T_2). SSE images thus do not quantitatively reflect either of these two quantities, and for that reason, may be difficult to interpret.

We propose here that a multi-spin echo sequence (MSE) would be much better suited when imaging plants with small-scale MR imagers, in which field strength inherently limits signal-to-noise performance. Using MSE, the exponentially decaying signal is sampled many times per excitation (Fig. 1). This makes for efficient signal acquisition and enables quantitative proton density imaging, even when long repetition times are required to avoid signal loss as a result of saturation. An additional benefit is that MSE (at short echo times) is relatively insensitive to magnet inhomogeneity (Donker *et al.*, 1997). In
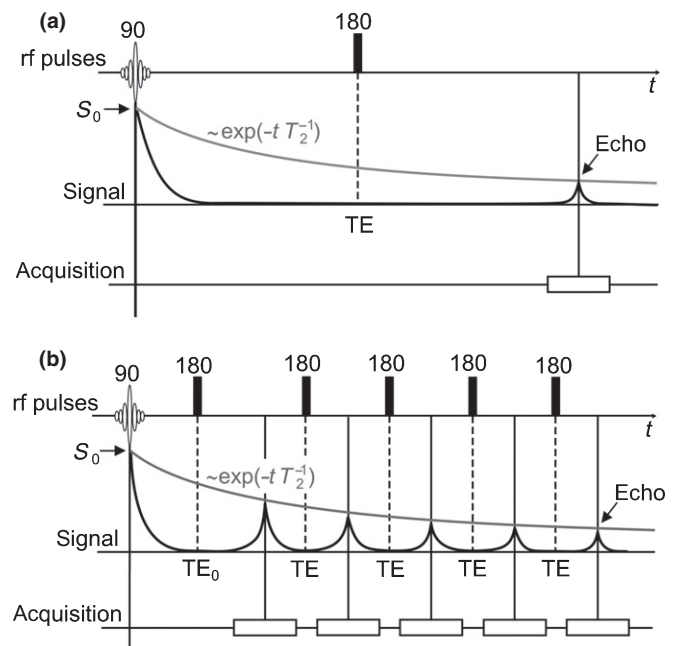
Fig. 1 Comparison of a single-spin echo (SSE) (a) and multi-spin echo (MSE) (b) imaging pulse sequences. In both cases (SSE and MSE) the sample is excited by means of a 90° pulse, after which the signal decays according to the relaxation time T_2, reflecting physicochemical sample characteristics such as proton mobility. In an SSE sequence the signal is refocused by means of a single radio frequency pulse (180° pulse), and acquired after a certain echo time (TE). In the SSE sequence this happens only once and TE is usually chosen to be very long. In the MSE sequence used here, the signal is refocused and acquired many times per excitation and TE is chosen to be as short as possible. S_0 is the amplitude of the signal immediately after excitation.

the data analysis following MSE acquisition, a monoexponential fit of the decaying signal for every pixel in the image will yield quantitative parameter maps of proton density (i.e. water content) and the relaxation time of the signal (T_2). T_2 is highly correlated to water mobility and compartment size (van der Weerd *et al.*, 2000) (also see Theory section). The T_2 relaxation time of water in wide lumina such as xylem vessels is much longer than that in the surrounding tissue, a property that can be measured even if the vessels themselves cannot be resolved (Windt *et al.*, 2007; Schepper *et al.*, 2012; Robert *et al.*, 2014). This may make T_2 a valuable parameter for monitoring the cavitation of vessels, even if they are smaller than the pixels.

In this study we demonstrate how a small-scale MRI scanner and complementary imaging method based on MSE can be used to visualize and quantify embolism formation. We constructed a magnet in which size, weight, robustness, pole gap width and accessibility for stems and branches was prioritized over sheer magnet homogeneity. The device was fitted with custom-built, plane parallel gradients that are open from the front, yet strong and fast enough to enable the use of MSE-type sequences, programmed on a small-scale spectrometer. Embolism formation was visualized and quantified using *Fagus sylvatica* (European beech) as a model species, a tree that is both drought-sensitive and of high economic relevance (Leuschner *et al.*, 2006; Tomasella *et al.*, 2019).

Theory: T_2 relaxation behavior in plants

Nuclear magnetic resonance relies on the fact that certain nuclei have a magnetic moment (spin). In plants the most abundant nucleus with spin is the proton (i.e. the nucleus of hydrogen ^1H). When placed in a strong homogeneous magnetic field, protons will orient themselves along with and opposite to the field direction. One of these two states will be slightly more populated, leading to a weak sample magnetization. After exciting the sample with an appropriate RF pulse, a signal can be detected as the protons induce a weak voltage in an RF coil placed around the sample (Schild, 1992; Köckenberger *et al.*, 1997). Two types of signal relaxation can be distinguished: spin-lattice relaxation (T_1) and spin-spin relaxation (T_2) (Haacke *et al.*, 1999). In the context of this study, only T_2 relaxation is of interest.

Spin–spin–relaxation describes the exponential decay of the amplitude of the signal (S) immediately after excitation (S_0), and is strongly correlated with proton mobility (Fig. 1). It reflects intra- and intermolecular proton–proton interactions that cause the signal (S) to decay exponentially as a function of time (t):

$$S = S_0 \exp\left(-\frac{t}{T_2}\right). \qquad \text{Eqn 1}$$

Signal amplitude S_0 thus linearly and quantitatively correlates with proton density, and, after normalizing against a phantom of 100% water, can be used to quantify the amount of water (A) in a pixel in absolute or relative terms.

The T_2 relaxation time of watery solutions in confined compartments or pores is a function of their inherent T_2 relaxation time, and the probability that water molecules of the solution reach the compartment membrane or wall (Brownstein & Tarr, 1979). Protons that pass through membranes are likely to end up in narrow compartments with much smaller relaxation times (cytoplasm, cell wall, intracellular spaces) and thus more rapidly lose their magnetization, or may interact with the compartment wall directly and lose their magnetization in that manner (van As, 2007).

Imaging maize and pearl millet, van der Weerd *et al.* (2001) modeled and demonstrated this correlation in living plant tissue. They modeled T_2 relaxation ($T_{2,obs}$) as a function of the T_2 of the bulk liquid ($T_{2,bulk}$) and the surface to volume ratio S/V, the latter of which scales with the inverse of the compartment size:

$$\frac{1}{T_{2,obs}} = H\frac{S}{V} + \frac{1}{T_{2,bulk}}. \qquad \text{Eqn 2}$$

The rate of wall relaxation or sink strength density H has been found to vary as a function of membrane permeability (van der Weerd *et al.*, 2000), but differences in compartment size typically dominate T_2. In practice, cells with the largest vacuoles and conduits with the widest diameters give rise to the longest T_2 relaxation times, approximating the T_2 of the bulk liquid (up to 2 s for pure water), whereas narrow pores, conduits or small cells give rise to T_2 values that are much smaller (tens of milliseconds). Correlations between the wide xylem vessels and long T_2 values have been observed in poplar (Windt *et al.*, 2007), cherry (Homan *et al.*, 2007), oak (Schepper *et al.*, 2012) and *Avicennia marina* (Robert *et al.*, 2014).

In this study we test if the correlation between the relaxation time T_2 and compartment size can be utilized to detect water-filled xylem conduits or, conversely, visualize their disappearance as a result of cavitation.

Materials and Methods

Plant material and experimental treatment

Two- to five-year-old European beech (*Fagus sylvatica*) saplings were purchased at a local nursery (Baumschule Veith, Merzenich, Germany) and grown in a glasshouse (16 h : 8 h, 20°C : 16°C, day : night), supplemental lighting provided by a set of metal halogen vapor lamps (SON-T Agro 250 W; Philips Lighting, Eindhoven, the Netherlands). They were watered every second day to capacity.

During the dehydration experiment the plants were continuously illuminated by a sodium vapor lamp (SON-T Agro 400W; Philips Lighting). Three polyethylene reference tubes (inner diameter 1 mm, Perfusor Line; Braun, Melsungen, Germany) were attached to every stem, filled with nickel nitrate-doped water (T_2 = 66, 165 and 296 ms). The MRI scanner was mounted around the stems of the intact trees at 110, 110 and 85 cm above the soil, for trees B1, B2 and B3, respectively. Stem diameters at the imaging slice were 10.2, 9.3 and 9.9 mm, respectively; the stem diameters at the base of the tree were 30.6, 22.3 and 34.6 mm. The stems were fixed with aluminum laboratory clamps above and below the position of the MRI magnet, and at the base of the stem. First, MR images of the intact, well-watered trees were acquired. Second, the stems were cut 10 cm above the soil to initiate desiccation. The

distances between the cut end of the stem and the imaging slice were thus 100 cm (B1 and B2) and 75 cm (B3). The drying trees were imaged every 2 h. After the MRI measurements, the imaged stem section was excised and stored at −20°C for microscopy.

MRI hardware and methods

A 0.25 T, 16 kg C-shaped permanent NdFeB magnet with a 35 mm air gap was custom-built and fitted with a three-axis plane parallel gradient set. The gradient set was etched on layers of two-sided 105 μm copper circuit boards (Octamex, London, UK) and mounted on an openable, aluminum frame that also served as a Faraday cage and a heat sink (Fig. 2a). To reduce magnetic field drift resulting from temperature changes, the poles of the magnet were equipped with resistive heating wire and coupled to an accurate temperature controller, regulating magnet temperature to a set point value of 29 °C. The MR imager was connected to a standard Kea II spectrometer (Magritek, Wellington, New Zealand) with a built-in 100 W RF amplifier. The gradients were driven by a set of three BAFPA40 gradient amplifiers (Bruker, Rheinstetten, Germany), yielding a maximum gradient strength of 0.24 T m^{-1} over a spherical volume of 25 mm. Before placing the plant inside the magnet, an 11-turn, 15-mm-diameter solenoidal RF coil was hand-wound around the stem with the help of a split Teflon coil former. The magnet was mounted on an adjustable nonmagnetic stand constructed of aluminum and stainless steel (Fig. 2b). If built in series, it is conceivable that small-scale MR imagers with similar specifications could be produced for less than, for example, a set of high-end portable infrared gas analyzers.

For image acquisition, an MSE (modified Carr, Purcell, Meiboom, Gill sequence (Edzes *et al.*, 1998), with an XY-8 phase cycling scheme) type imaging pulse sequence was used. Imaging was done using the following settings: matrix size 128 × 128, repetition time 1.5 s, 64 echoes, first echo time 3.95 ms, all subsequent echo times 2.01 ms for B1 and 2.1 for B2 and B3. The slice thicknesses were 4.5, 5.5 and 5.0 mm, the fields of view 18.0, 15.5 and 14.7 mm, and the number of averages 32, 32 and 24, for plants B1, B2 and B3, respectively.

All image acquisition and initial data processing were done in PROSPA (Magritek). First, all images were masked and phase corrected according to Ma *et al.* (2008). Quantitative water content (*A*) and T_2 maps were calculated on the basis of a monoexponential fit of the signal ($S(t)$) for every pixel according to Eqn 1. Water content maps were normalized by dividing them by the average water content value of all three reference tubes. $A \times T_2$ product maps were obtained by performing a pixel-by-pixel multiplication of the amplitude and T_2 maps.

Obtaining vulnerability curves

Before each MR measurement, the plant leaf water potential was determined according to Scholander *et al.* (1964). For this purpose a random twig was bagged, cut off and quickly transferred to a pressure chamber (Model 1000; PMS Instrument Co., Albany, NY, USA). On the basis of calibration curves that were acquired by means of independently obtained dry-down measurements, we found the difference between stem and leaf water potential to be insignificant for beech saplings after stomatal closure occurred, at water potentials of −1.5 MPa and lower.
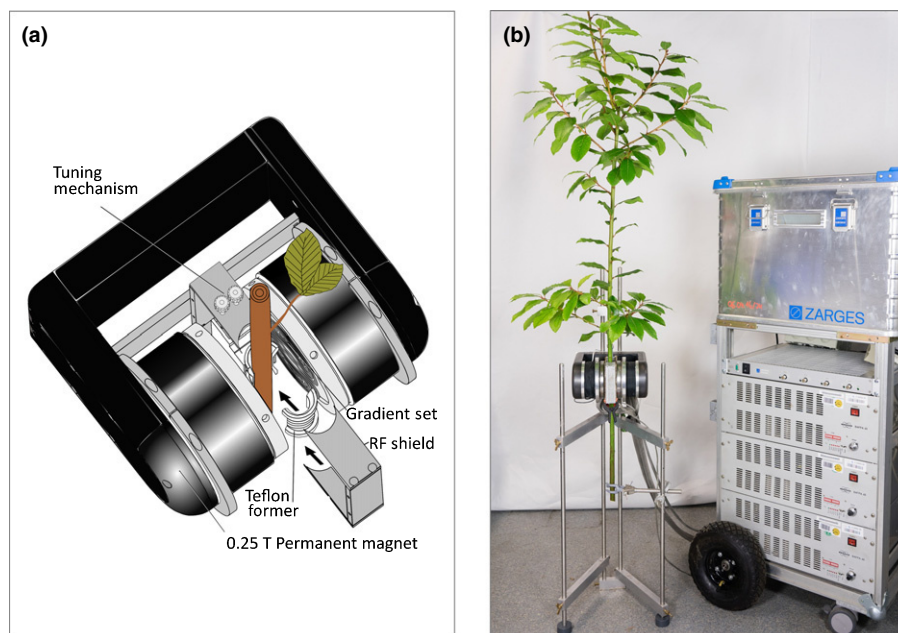
Fig. 2 (a) Schematic representation of the small-scale magnetic resonance imaging (MRI) magnet and plus probe head. The magnet as well as the plane parallel imaging gradient coils are open and fully accessible from the front, allowing trees or branches to be slid in. Arrows indicate how the split coil and the probe head close around the plant. The magnet has an air gap of 35 mm and a spherical homogeneous region of 25 mm in diameter, defining the maximum field of view. The probe head and radio frequency (RF) coil are slightly more restrictive, allowing for a maximum object diameter of 20 mm. (b) The complete instrument. The magnet is borne by an adjustable nonmagnetic support. Three large gradient amplifiers and associated components are mounted in the wheeled aluminum trolley; on top of it an aluminum enclosure is visible that contains the spectrometer.

To obtain vulnerability curves (VCs), xylem masks were created for all measurements. The xylem region was selected by hand, excluding the phloem, bark and reference tubes from further analysis. Slight changes in stem position over the course of the dry-down experiment were corrected by shifting the masks accordingly. VCs were calculated using four different methods. First, by determining the loss of conductivity on the basis of the number pixels lost within binarization masks of (method 1) the amplitude or (method 2) the $A \times T_2$ product maps; and second, on the basis of the loss of the total proton density (i.e. the amount of water per pixel) that was lost during dry-down from within the previously mentioned binarized masks, made on the basis of water content (method 3) or $A \times T_2$ product maps (method 4).

To obtain a relative value for the embolized xylem area ($\%_{emb}$), the initial pixel count or amplitude sum ($P_{initial}$) and the final pixel count or amplitude sum (P_{min}) were calculated from the number of pixels above threshold (P_{abv}):

$$\%_{emb} = 100 \times \frac{P_{initial} - P_{abv}}{P_{initial} - P_{min}}. \qquad \text{Eqn 3}$$

The resulting curves of all four approaches mentioned were fitted with a sigmodial function (Pammenter & van der Willigen, 1998):

$$\%_{emb}(\psi_{xylem}) = \frac{100}{1 + \exp\left(\frac{S}{25}\left(\psi_{xylem} - \psi_{50}\right)\right)}, \qquad \text{Eqn 4}$$

where the slope and the position of the curve in x-direction are denoted by S and Ψ_{50}, respectively, the latter indicating the water potential at which 50% of the xylem is embolized. All fits were performed with MATLAB (Mathworks, Natick, MA, USA) and fitting errors were calculated according to Press (2002).

Light microscopy

After the dry-down experiment, the imaged stem pieces were marked and excised. Transverse sections of 20 µm were prepared with a sliding microtome (GSL1; Schenkung Dapples, Zürich, Switzerland) and stained with a 1 : 1 (v/v) mixture of safranin and astrablue, following Gärtner & Schweingruber (2013). Images of the cross-section were obtained with a digital camera connected to a light microscope (Leica Microsystems GmbH, Wetzlar, Germany), at a magnification of ×4 in combination with a digital camera (Kappa PS30; Kappa optronics GmbH, Gleichen, Germany). All images were merged with Adobe PHOTOSHOP CS2 to obtain the picture of the whole cross-section.

Results

Imager and imaging

The half-open C-shaped design of the small-scale MR imager allowed mounting of the setup on a plant in < 20 min. Although still 16 kg, the weight of the magnet was low enough to allow its

position, height and angle to be adjusted easily and by hand. An MSE imaging sequence (Edzes *et al.*, 1998) was implemented and run continuously, which can be thermally challenging for a gradient set without active cooling. Here, up to 64 echoes could be acquired, for all examples shown in this study, without overheating the gradient system. The prototype imager proved to be reliable, allowing continuous operation during several months of tests and dry-down experiments.

Water content and T_2 maps of stems of well-watered beech saplings were acquired, in which seven different types of tissue could be clearly identified (from outside to inside): bark, phloem and cambium, early- and latewood of the annual xylem rings, the pith and (in B1) xylem parenchyma rays. Despite the fact that all trees were furnished by the same grower, were of the same genotype and of comparable heights and stem diameters, their anatomy revealed strongly varying life histories. B1 and B3 had five annual rings at the imaging position, whereas B2 had only two. The current-year annual ring in B1 exhibited evidence of much faster growth than the annual rings from earlier years, whereas both annual rings of B2 showed fast growth.

The most striking features of the parameter maps were the bright bands in the annual rings, which became visible in the amplitude maps as well as in the T_2 maps. The contrast of these bright rings was fairly low in the amplitude maps, but much higher in the T_2 maps and could be improved even more by multiplying the two parameter maps to yield $A \times T_2$ product maps (Fig. 3). The latter procedure resulted in images with excellent contrast and low noise that did not require any image manipulation to remove spikes resulting from erroneous fitting in areas of low signal intensity.

The bright rings of high water content and long T_2 were clearly associated with a high density of wide vessels, except for the oldest annual ring. This was illustrated by matching the microscopic xylem structure accurately with the MR images, overlaying the microscopy image of B3 with its T_2 map (Fig. 4). The water content in those bright rings was *c.* 70% (Fig. 3, row I), while the darker latewood surrounding those regions showed values of *c.* 30%. The T_2 maps showed a similar pattern but with much greater contrast (row II). The bright rings had T_2 values of *c.* 90 ms, while the remaining tissue exhibited values of *c.* 20 ms. The bright xylem rings in the T_2 maps were slightly wider than those in the amplitude maps.

Imaging embolism formation

During the dry-down experiment three beech saplings were bench dehydrated, while an MR measurement and a water potential measurement were conducted every 2 h. Of the resulting time series of images and water potential measurements, only the five sets that show the most significant changes are displayed (Fig. 5). Videos incorporating all product images that were acquired during dry-down of each plant are provided in Supporting Information Videos S1–S3.
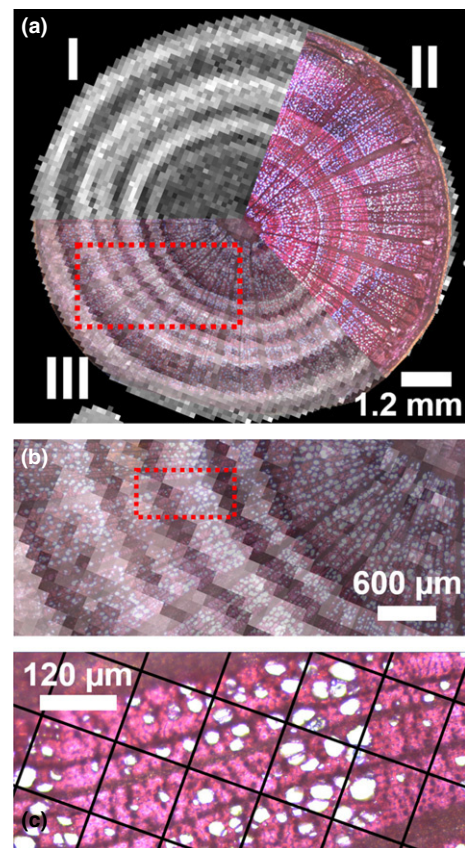
In all parameter maps (water content (A), T_2 and $A \times T_2$) the bright rings in the xylem were found to progressively disappear at increasingly negative water potentials, supporting the idea that
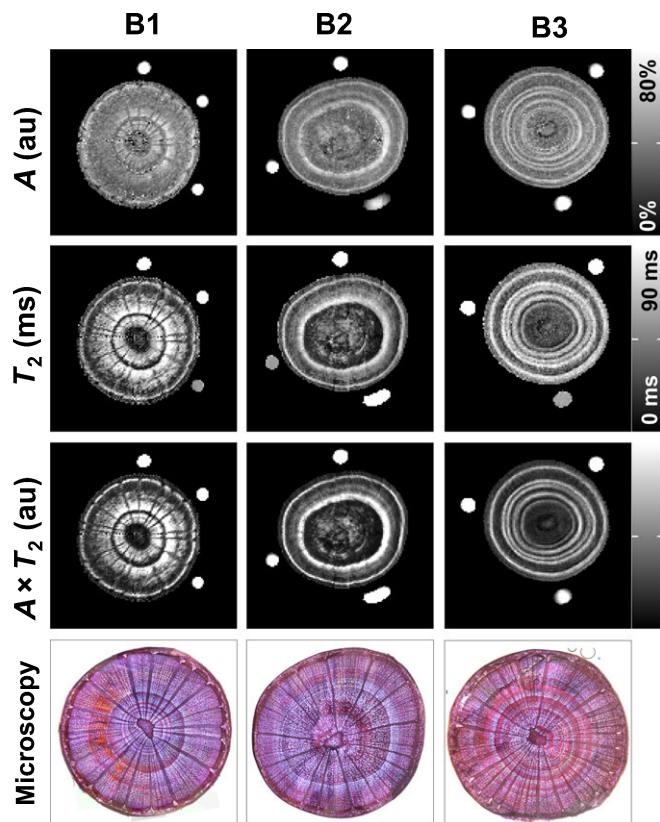
Fig. 3 Comparison of amplitude (A), relaxation time (T_2) and $A \times T_2$ product maps of the stems of three well-watered beech (*Fagus sylvatica*) trees (B1, B2, B3), measured before commencing the dry-down experiment, and optical microscopy of the same positions in the stems after harvesting (bottom row). The first row shows the signal amplitude maps in au, normalized to relate linearly and quantitatively to water content (0–80%); the second row illustrates T_2 relaxation maps in ms; the third shows the product maps of amplitude and relaxation time. Bars indicate the values corresponding with black (minimum) and white (maximum) values. Next to the plants three reference tubes are visible. The fourth row shows microscopy images of each plant at the same position.

Fig. 4 (a) Overlay of the relaxation time (T_2) parameter map and the corresponding light microscopy image of beech (*Fagus sylvatica*) stem B3. Region I of the image shows the T_2 map, region II microscopic image, and region III an overlay of the half transparent microscopy image with the T_2 map superimposed. (b) Magnified view of the region indicated with a dashed box in (a). (c) Further magnification of the region indicated in (b). In this window the grid indicates the magnetic resonance imaging pixel size ($120 \times 120\ \mu m$).

the declining water content and the change in T_2 corresponded with the loss of water from previously filled xylem vessels. The percentage change in water content was much smaller than the percentage change in T_2. The average amplitude loss observed for pixels with filled xylem vessels over the course of the dry-down ranged from 37% to 48% (B1, 37.1%; B2, 48.4%; B3, 35.5%), concomitant with a decrease in water potential of *c.* -1 to < -5 MPa. The corresponding changes in T_2, however, were about twice as large and ranged from 67% to 72% (B1, 72.3%; B2, 71.3%; B3, 67.9%). At the end of the dry-down experiment, at water potentials < -5 MPa, in all three trees the residual xylem water content was *c.* 30% with a T_2 value of around 20 ms. As shown in Fig. 5, the contrast provided by the water content and T_2 maps could be improved even further by multiplying the two parameters. The resulting $A \times T_2$ product maps were found to show even greater percentage changes over the course of the dry-down (B1, 81.7%; B2, 85.0%; B3, 78.9%).

In most beech stems, the oldest annual rings lost water and showed declining T_2 values before the younger ones did. The

only exception was the second annual ring in B3, which lost water before the third one (rings counted from the outside). For all beech trees, a homogeneous radial spread of emboli within the annual rings was observed, resulting in a narrowing of the bright xylem sections. As the dry-down continued, the radial spread of emboli within the rings was accompanied by a tangential spread. For all trees, the latewood within the rings was affected first (signal decline < -2 MPa), the earlywood last. Before the dry-down, in B1 a domain of low water content and T_2 within the current annual ring was already showing, extending in tangential direction (arrow in Fig. 5a, row III). Below -3 MPa this domain of low water content and T_2 values grew larger and spread in tangential and radial directions.

Vulnerability curves

Four methods to approximate the percentage loss of conductivity (PLC) were tested: (1) calculation of PLC on the basis of the loss of number of pixels containing water-filled vessels, determined on the basis of binarized amplitude maps; (2) as method 1 but calculated on the basis of binarized $A \times T_2$
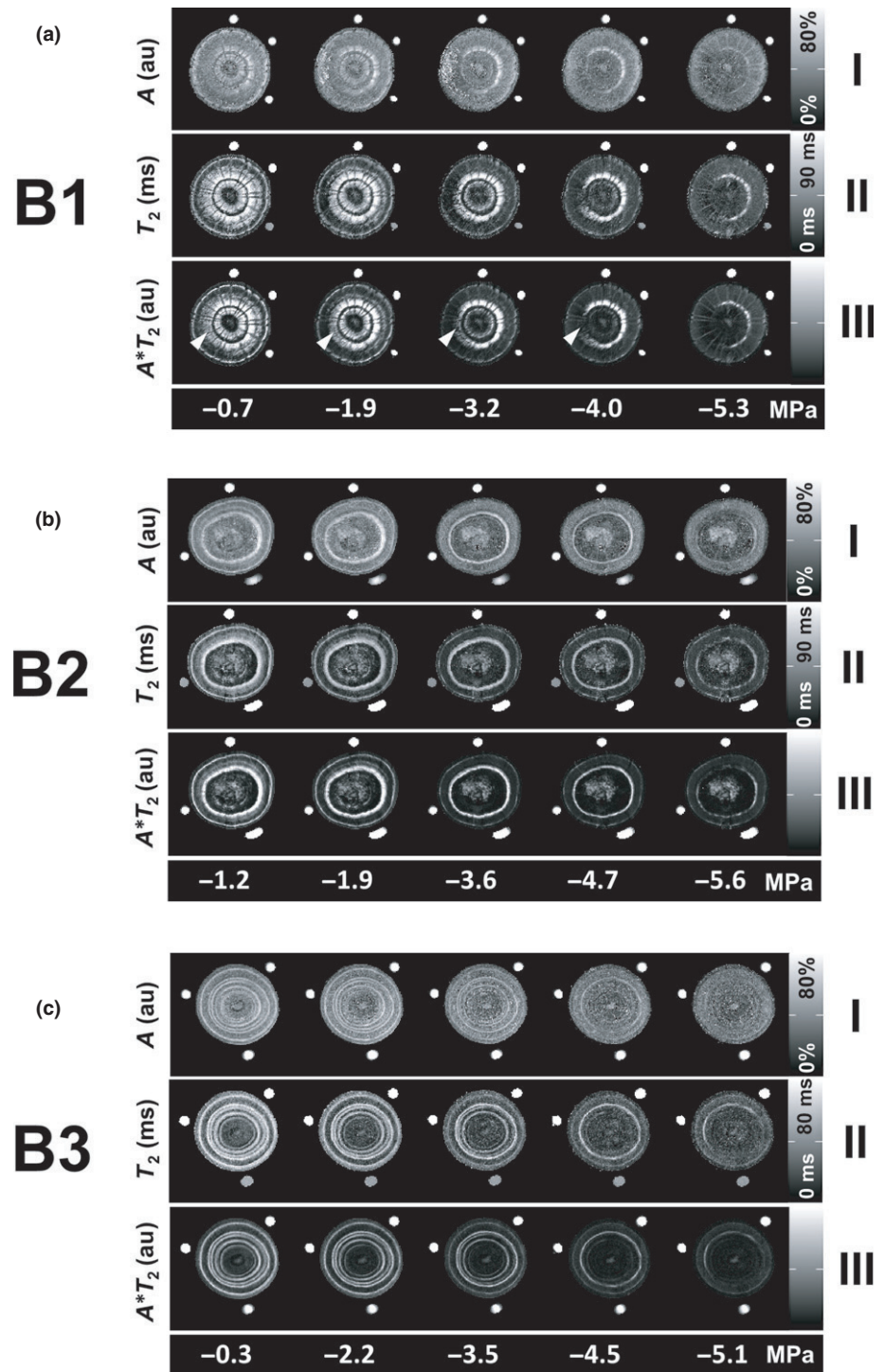
Fig. 5 A comparison of magnetic resonance maps acquired during progressive dry-down of three beech (*Fagus sylvatica*) trees (a–c, B1, B2 and B3, respectively). Row I shows the signal amplitude (A), normalized to relate linearly and quantitatively to water content (0–80%); row II shows relaxation time (T_2); row III shows the $A \times T_2$ product maps; corresponding water potential values are shown underneath (WP).

product maps; (3) as method 1 but based on the decrease in the cumulative proton density in the pixels identified by means of binarized amplitude maps; and (4) as method 3 but based on the cumulative proton density in the pixels identified by means of binarized $A \times T_2$ product maps. Masks resulting from the binarization of water content and $A \times T_2$ product maps are shown for five water potential values of B3 in Fig. 6(c,d). Using Eqn 3 and fitting the result with a sigmodial function (Eqn 4), VCs were calculated either on the basis of the number of pixels

in the binarization masks, or by summing up amplitude values of those pixels (Fig. 6a,e,f). The exact values and error values of r^2, slope and Ψ_{50} for each plant are provided in Table S1. All four approaches resulted in VCs that matched the data points well, with values of r^2 close to 1. The vulnerabilities of samples B1 and B3 were found to be very similar (a difference of *c.* 0.1 MPa), whereas the Ψ_{50} of B2 was found to be *c.* 0.6 MPa lower. An additional comparison of the four methods with all plants grouped together, done by means of the FITPLC package

Amplitude maps

(a)

Product maps

(b)

(c)

(d)

(e)

(f)
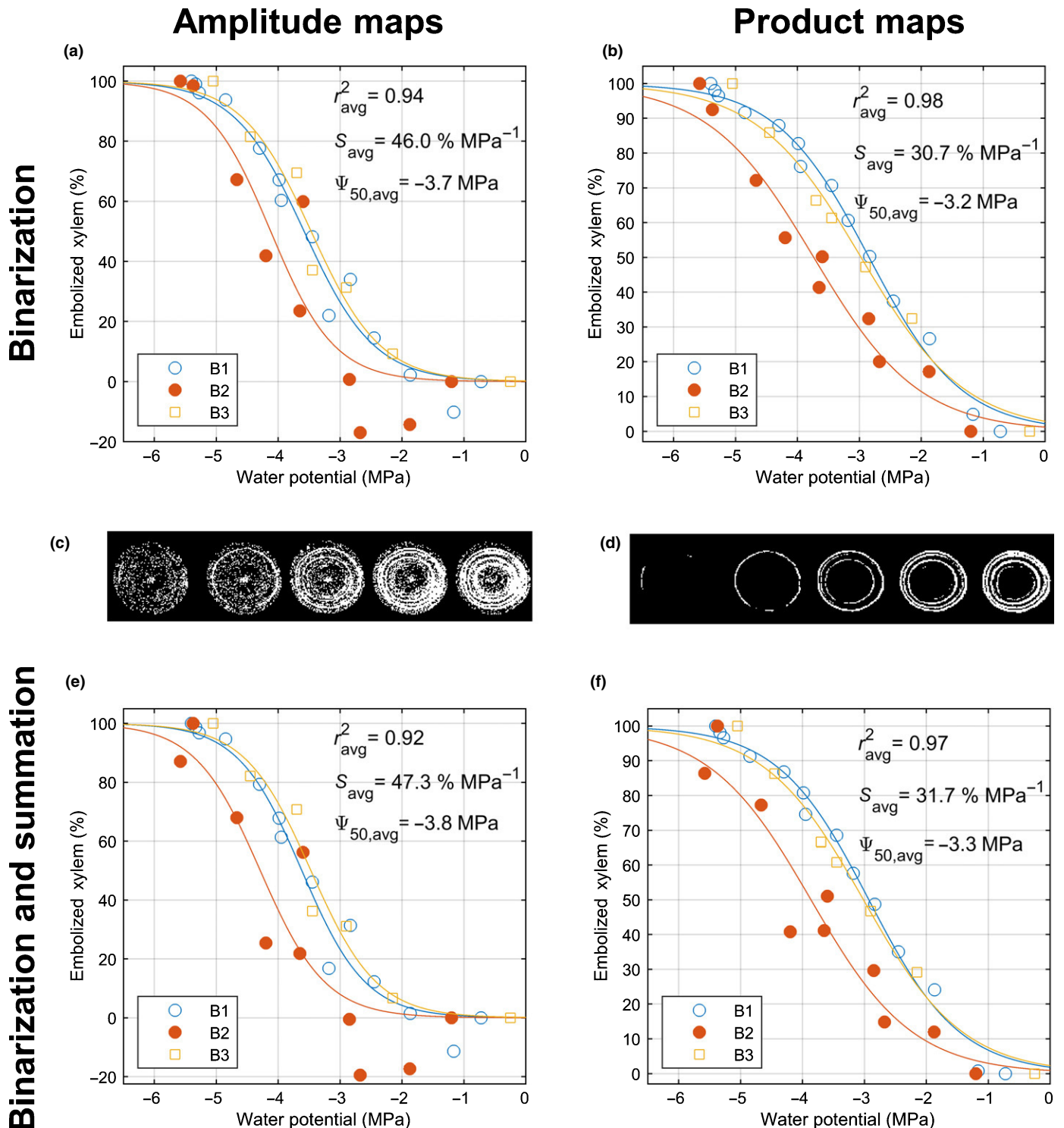
Fig. 6 Vulnerability curves (VCs) based on binarized amplitude and amplitude × relaxation time ($A \times T_2$) magnetic resonance images of three beech (*Fagus sylvatica*) trees. (a, b) VCs constructed on the basis of the cumulative pixel area of all pixels with values above a threshold in the amplitude (a) or $A \times T_2$ product images (b). (c, d) Examples of the masks thus created are shown for five water potential values (in MPa: −0.3, −2.2, −3.5, −4.5, −5.1) in B3. (e, f) VCs are shown that were constructed on the basis of the change in water content (i.e. amplitude) inside the same masks as before, made on the basis of amplitude images (e) and $A \times T_2$ product images (f). After normalizing, all curves were fitted with a sigmodial function; in the upper right corner the mean values for r^2, slope S and Ψ_{50} of the curves are shown. For the values of the individual curves see Supporting Information Table S1. For a supplemental analysis of the data with the FITPLC package see Fig. S1.

(Duursma & Choat, 2017), is provided in Fig. S1 and yielded comparable results.

The masks based on the product maps much more clearly reflected the filled xylem than those based on the amplitude maps (Fig. 6c,d). This corresponds to the fact that the contrast between filled and cavitated xylem pixels was much greater in the product maps than in the amplitude maps, as was the signal-to-noise ratio of the respective images.

Compared with VCs obtained from binarized product images (Fig. 6b,f), VCs obtained from binarized amplitude images (a and e) resulted in lower values of r^2, steeper slopes and more negative values for Ψ_{50}.

Discussion

Imaging xylem embolism formation

Despite the low field strength and the relatively low resolution afforded by the small-scale MR imager, our method was remarkably successful at visualizing the appearance and spread of embolism in the xylem. The use of an MSE imaging sequence allowed for efficient signal acquisition, enabling the computation of quantitative water content and T_2 maps. Embolism formation became visible in all three parameter maps that were acquired, water content, T_2 and $A \times T_2$. The multiplication of amplitude and T_2 maps to yield $A \times T_2$ product maps was especially helpful, as it provided even more contrast between filled and empty xylem than did either amplitude or T_2 maps, while also yielding cleaner and less noisy images without any further image processing.

The time resolution of the measurements (2 h) was sufficient to visualize the spread of emboli. Embolism spread happened first radially, from latewood to earlywood (i.e. from outside to inside), and subsequently in a tangential direction. This was indicated by bright (i.e. water-filled) rings becoming narrower from the outer to the inner xylem. We did not observe a spread of emboli between annual rings. This agrees with observations by Fukuda et al. (2015), who saw a similar narrowing of rings from outside to inside in Katsura and Japanese birch. Brodersen et al. (2013a, b) observed in grapevine a radial spread of emboli as well, but in the other direction, that is, from the pith towards the cambium via direct connections and xylem vessel relays between vessels.

Xylem conduits in the older annual rings of all samples cavitated at less negative water potentials than those in the youngest annual rings. This is in agreement with findings of previous non-invasive studies on angiosperms (Fukuda et al., 2015) and gymnosperms (Umebayashi et al., 2016). The phenomenon has been suggested to be caused by cavitation fatigue, attributed to repeated cycles of drought causing pit membrane degradation (Hacke et al., 2001; Melcher et al., 2003; Hillabrand et al., 2016).

A water content of c. 30% remained in the wood after water potentials dropped below −5 MPa, at which point most of the bright rings had already disappeared (Fig. 5). The T_2 value of this remaining water was c. 20 ms, which is significantly lower than the T_2 value of regions with filled vessels. The T_2 of the remaining water is depressed, because it resides in narrow lumina such

as fiber tracheids (Schweingruber, 1990). While Fukuda et al. (2015), by means of scanning electron microscopy, also found remaining water in fiber tracheids surrounding cavitated vessels in the xylem of Katsura, this water was hardly visible in their MRI images. This may be attributed to the fact they used an SSE imaging sequence with an echo time of 13 ms. After that time, most signal from water in fiber tracheids can be assumed to be lost as a result of T_2 signal relaxation.

Simulating embolism detection by means of T_2 relaxation

Embolism formation in vessels became visible more readily in the T_2 parameter maps than in the water content maps, confirming that T_2 provides a useful parameter with which the presence, and subsequent disappearance, of water in filled vessels with long T_2 relaxation times can be detected amongst the signal of water within the wood around the vessel lumina. The latter pool of water has much shorter relaxation times and is found in narrow structures such as fibers, intracellular spaces, or cell wall matrices. T_2 thus becomes a means to gain subpixel information: if in a pixel sufficient water is present in conduits with a T_2 that is much
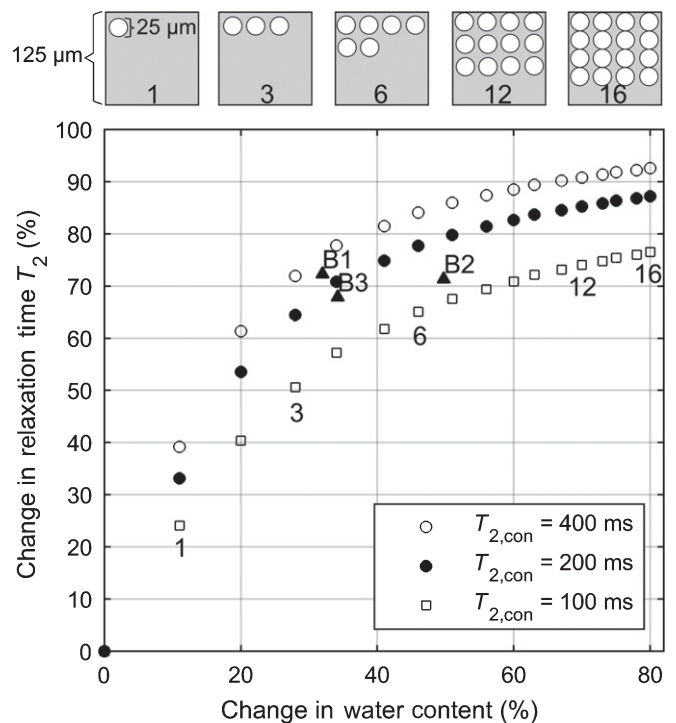
Fig. 7 Modeled relationship of the percentage change in amplitude (A) and relaxation time (T_2) that is expected if n vessels are present in a pixel, and all cavitate. In the model, pixels had a size of 120 × 120 μm and all conduits had a diameter of 25 μm. The simulation is run for 0–16 conduits with a volumetric water content of 100% with T_2 values of 100, 200 and 400 ms (see key). The wood around the conduits is assumed to have a volumetric water content of 30% with a T_2 of 20 ms. The resulting curves indicate a larger effect on the T_2 value of a pixel than on its amplitude value, in case only a few (one to six) vessels inside of it cavitate. The actual average changes in amplitude and T_2 that were measured in the different beech individuals were added to the graph (filled triangles) and match well with the modeled results.

longer than that of water in the surrounding wood, the T_2 relaxation time of the pixel as a whole will be elevated sufficiently to stand out clearly.

The data acquisition and monoexponential fitting were simulated to compare how the two fit parameters are affected by the presence and subsequent cavitation of varying numbers of vessels inside of a pixel. The NMR signal before cavitation was assumed to be the sum of two pools of water in a pixel: water in conduits (S_{con}), comprising both tracheids and vessels with longer T_2 values ($T_{2,con}$); and water in all other, much narrower spaces in the wood such as fibers and intracellular lumina (S_{other}), with a correspondingly short T_2 ($T_{2,other}$). After cavitation of all conduits in a pixel, the only remaining NMR signal was assumed to originate from water in the wood surrounding the conduit lumina.

The signals of both pools of water were calculated assuming that all space not occupied by conduits was filled by wood, that all conduits had a diameter of 25 μm, and that the water content of the wood before and after cavitation remained at 30%. The conduit diameter was chosen on the basis of the observed conduit diameter distributions (see Fig. S2); the water content of the wood was estimated based on the water content next to the bright rings observed in the water content images. The NMR signal of a pixel was subsequently modeled on the basis of Eqn 1:

$$S_{con} = \frac{n_{con} A_{con}}{A_{pix}} \exp\left(-\frac{t}{T_{2,con}}\right),$$
<div align="right">Eqn 5</div>

and

$$S_{other} = 0.3 \times \left(1 - \frac{n_{con} \times A_{con}}{A_{pix}}\right) \exp\left(-\frac{t}{T_{2,other}}\right),$$
<div align="right">Eqn 6</div>

where n_{con} represents the number of conduits in a pixel, A_{con} their cumulative cross-sectional area, and t the time after excitation. The simulated NMR signal was sampled according to the settings used for the actual image acquisition. The resulting data points were fitted monoexponentially, providing estimates for amplitude and T_2, calculated first for the scenario in which all conduits were filled, second for the scenario in which all were cavitated. To estimate the response of both parameters to cavitation events, the percentage difference between the T_2 values of both scenarios was plotted against their difference in amplitude. The simulation was run for pixels with between 0 and 16 conduits (see pixel sketches in Fig. 7), in which the water in the conduits was modeled to have $T_{2,con}$ values of 100, 200 and 400 ms.

The results of the simulation corresponded well with the percentage change observed in the images (Fig. 7). The curves showed slopes of well over one for between one and five vessels, indicating that the presence and subsequent cavitation of only a few filled vessels already had a large influence on the observed T_2 value of a pixel. Please note that in the model, all vessels within a pixel are assumed to cavitate. For example, the cavitation of a single vessel which covers 3.4% of the pixel area will cause an amplitude change of 11%, but will cause an even larger increase in the T_2 relaxation time of 25–40%, depending on the value chosen for $T_{2,con}$. This difference decreased for larger numbers of vessels.

To facilitate a direct comparison between the parameter maps and the model, the average percentage changes of water content and T_2 within the bright xylem regions were plotted in Fig. 7. In the simulation, between three and seven vessels per pixel (n_{con}) explained the changes that were observed in amplitude and T_2, for a value for $T_{2,con}$ of between 100 and 400 ms. Those values accurately matched the numbers of vessels that have been found per MRI pixel (Fig. 4c).

During dry-down, the bright rings in the T_2 maps that indicate the presence of filled vessels were always equal in width or wider than the bright rings in the amplitude maps. This suggests that, even when in a pixel a few but not all conduits were cavitated, the T_2 value for such a pixel would remain higher. This response would correctly indicate the presence of filled conduits, but be binary in nature, contrary to the amplitude maps, in which the gradual cavitation of conduits in a pixel results in a gradual reduction of intensity. By combining the two parameters by a multiplication into the $A \times T_2$ parameter maps, the strengths of both are combined, boosting contrast and alleviating the problem of the low SNR that is inherent to the use of a low-field MR imager. The near-binary response of T_2 to the presence of filled vessels is also expressed in the width of the bright rings in the xylem. During the course of the dry-down experiment, bright rings were wider in the T_2 maps than in the water content maps. Further, in the final dry-down images (< -5 MPa) the amplitude maps no longer showed evidence of the presence of remaining filled vessels, whereas in the T_2 and $A \times T_2$ maps some pixels with filled conduits still remained (Fig. 5).

The sensitivity of the T_2 relaxation time to the presence of filled vessels is based on the large difference in the T_2 relaxation time of the NMR signal originating from water in wood and conduits. As T_2 increases with conduit diameter, the method is likely to be applicable for all species in which conduit diameters are similar to, or wider than, those of beech. However, to what degree mapping T_2 would yield comparable results in xylem architectures with smaller or fewer vessels than beech remains to be tested. If T_2 in narrow conduits approaches that of water in wood, the T_2 contrast advantage would be lost.

Vulnerability curves

Surprisingly, despite the noisy appearance of the masks resulting from the binarization of amplitude maps (Fig. 6c,d), all four approaches to obtain a measure for the relative loss of conductivity from binarized MR images successfully yielded VCs. The difference in the VCs based on amplitude maps (Fig. 6a,e) is that more water from nonconducting tissues is included. In binarizing the amplitude images much care was taken not to set the threshold too low, which, owing to the high noise floor, could have led to the exclusion of pixels with filled conduits. The application of a conservative threshold, conversely, will have resulted in the inclusion of pixels that contain wood and water, but no filled conduits. The masks based on $A \times T_2$ product maps, thanks to the high contrast and low noise figure of the latter, most effectively singled out pixels with filled conduits.

Vulnerability curves obtained from $A \times T_2$ product masks resulted in curves with a higher r^2, a more shallow slope and a less negative Ψ_{50}, compared with the VCs obtained from the binarized amplitude images. In both cases, the difference between VCs calculated on the basis of the loss of water within the binarized masks (Fig. 7e,f), and those based on the mere number of pixels left in the mask (Fig. 7a,b), was negligible. The most convenient method to derive VCs from the imaging data thus proved the most useful: binarization on the basis of $A \times T_2$ product images, combined with an estimation of the PLC on the basis of the decrease in the numbers of pixels within the binarization masks.

The differences in the estimates of Ψ_{50} for the two methods were relatively minor, ranging from -3.2 and -3.3 ($A \times T_2$ product masks) to -3.7 and -3.8 MPa (amplitude masks). These values are in good agreement with those reported in other studies on beech saplings (Caquet *et al.* (2009) and Aranda *et al.* (2015) reported values of -3.0 to -4.0, and -3.0 to -3.7 MPa, respectively), while there are also studies that found less negative values (Cochard *et al.* (1999) and Barigah *et al.* 2013) reported values of -2.5 to 3 and -2.5 MPa, respectively). Studies on mature beech trees also resulted in similar values (Lemoine *et al.*, 2002, -2.2 to -3.1 MPa; Herbette *et al.*, 2010, -3.0 MPa; Schuldt *et al.*, 2016, -3.3 to -3.7 MPa; Stojnic *et al.*, 2018, -2.9 to -3.5 MPa; Tomasella *et al.*, 2018, -2.5 MPa). In the framework of the current study we have not been able to cross-correlate our results with established benchmark methods. In future experiments it would be most interesting to follow up on this study by making such a comparison.

Conclusions

In this study we have demonstrated that MRI scanners based on small-scale, low-field permanent magnets are capable of imaging embolism formation in diffuse-porous angiosperms such as beech. By combining such an imager with an MSE imaging sequence, quantitative parameter maps of water content and T_2 signal relaxation could be obtained. While both types of images could be used to detect xylem cavitation, T_2 parameter maps were found to be especially sensitive to it. By multiplying the parameter maps of water content and T_2 relaxation time, $A \times T_2$ product maps could be obtained in which regions with filled vessels could be identified even more clearly. The improved contrast afforded by the $A \times T_2$ product maps also provided a convenient way to obtain VCs by means of straightforward image binarization.

The MSE imaging sequence, as a means to quantitatively map T_2 relaxation times to visualize and detect filled conduits that are too small to be resolved spatially, could also be helpful when used on conventional imagers with much higher field strengths. In such imagers, signal to noise will not be limiting, but T_2 contrast may still be expected to facilitate the detection of filled conduits, if the latter cannot be identified, because of the limited spatial resolution, on the basis of imaging alone.

Author contributions

CWW and MM designed, built and programmed the magnetic resonance imager. MM performed the experiment and analyzed the data. MT prepared the anatomical sections and microscopic images. MM and CWW wrote the manuscript with contributions from PF and MT.

ORCID

Petra Foerst (iD) https://orcid.org/0000-0002-6381-1543
Marco Meixner (iD) https://orcid.org/0000-0002-3992-9920
Martina Tomasella (iD) https://orcid.org/0000-0002-1470-1030
Carel W. Windt (iD) https://orcid.org/0000-0003-2400-5407

References

Aranda I, Cano FJ, Gascó A, Cochard H, Nardini A, Mancha JA, López R, Sánchez-Gómez D. 2015. Variation in photosynthetic performance and hydraulic architecture across European beech (*Fagus sylvatica* L.) populations supports the case for local adaptation to water stress. *Tree Physiology* 35: 34–46.

Barigah TS, Charrier O, Douris M, Bonhomme M, Herbette S, Améglio T, Fichot R, Brignolas F, Cochard H. 2013. Water stress-induced xylem hydraulic failure is a causal factor of tree mortality in beech and poplar. *Annals of Botany* 112: 1431–1437.

Borisjuk L, Rolletschek H, Neuberger T. 2012. Surveying the plant's world by magnetic resonance imaging. *The Plant Journal* 70: 129–146.

Brodersen CR, Choat B, Chatelet DS, Shackel KA, Matthews MA, McElrone AJ. 2013a. Xylem vessel relays contribute to radial connectivity in grapevine stems (*Vitis vinifera* and *V. arizonica*; Vitaceae). *American Journal of Botany* 100: 314–321.

Brodersen CR, Lee EF, Choat B, Jansen S, Phillips RJ, Shackel KA, McElrone AJ, Matthews MA. 2011. Automated analysis of three-dimensional xylem networks using high-resolution computed tomography. *New Phytologist* 191: 1168–1179.

Brodersen CR, McElrone AJ, Choat B, Lee EF, Shackel KA, Matthews MA. 2013b. *In vivo* visualizations of drought-induced embolism spread in *Vitis vinifera*. *Plant Physiology* 161: 1820–1829.

Brodersen CR, McElrone AJ, Choat B, Matthews MA, Shackel KA. 2010. The dynamics of embolism repair in xylem. *In vivo* visualizations using high-resolution computed tomography. *Plant Physiology* 154: 1088–1095.

Brownstein KR, Tarr CE. 1979. Importance of classical diffusion in NMR studies of water in biological cells. *Physical Review A* 19: 2446.

Caquet B, Barigah TS, Cochard H, Montpied P, Collet C, Dreyer E, Epron D. 2009. Hydraulic properties of naturally regenerated beech saplings respond to canopy opening. *Tree Physiology* 29: 1395–1405.

Choat B, Badel E, Burlett R, Delzon S, Cochard H, Jansen S. 2016. Noninvasive measurement of vulnerability to drought-induced embolism by X-ray microtomography. *Plant Physiology* 170: 273–282.

Choat B, Brodribb TJ, Brodersen CR, Duursma RA, López R, Medlyn BE. 2018. Triggers of tree mortality under drought. *Nature* 558: 531–539.

Choat B, Drayton WM, Brodersen C, Matthews MA, Shackel KA, Wada H, McElrone AJ. 2010. Measurement of vulnerability to water stress-induced cavitation in grapevine. A comparison of four techniques applied to a long-vesseled species. *Plant, Cell & Environment* 33: 1502–1512.

Clearwater MJ, Clark CJ. 2003. *In vivo* magnetic resonance imaging of xylem vessel contents in woody lianas. *Plant, Cell & Environment* 26: 1205–1214.

Cochard H, Lemoine D, Dreyer E. 1999. The effects of acclimation to sunlight on the xylem vulnerability to embolism in *Fagus sylvatica* L. *Plant, Cell & Environment* 22: 101–108.

Dai A. 2013. Increasing drought under global warming in observations and models. *Nature Climate Change* 3: 52–58.

de Schepper V, van Dusschoten D, Copini P, Jahnke S, Steppe K. 2012. MRI links stem water content to stem diameter variations in transpiring trees. *Journal of Experimental Botany* 63: 2645–2653.

Dhondt S, Vanhaeren H, van Loo D, Cnudde V, Inzé D. 2010. Plant structure visualization by high-resolution X-ray computed tomography. *Trends in Plant Science* 15: 419–422.

Donker HCW, Van As H, Snijder HJ, Edzes HT. 1997. Quantitative 1H-NMR imaging of water in white button mushrooms (*Agaricus bisporus*). *Magnetic Resonance Imaging* 15: 113–121.

Duursma RA, Choat B. 2017. fitplc. An R package to fit hydraulic vulnerability curves. *Journal of Plant Hydraulics* 4: 002.

Edzes HT, van Dusschoten D, van As H. 1998. Quantitative T$_2$ imaging of plant tissues by means of multi-echo MRI microscopy. *Magnetic Resonance Imaging* 16: 185–196.

Fukuda K, Kawaguchi D, Aihara T, Ogasa MY, Miki NH, Haishi T, Umebayashi T. 2015. Vulnerability to cavitation differs between current-year and older xylem. Non-destructive observation with a compact magnetic resonance imaging system of two deciduous diffuse-porous species. *Plant, Cell & Environment* 38: 2508–2518.

Gärtner H, Schweingruber FH. 2013. *Microscopic preparation techniques for plant stem analysis*. Remagen, Germany: Verlag Dr. Kessel.

Haacke EM, Brown RW, Thompson MR, Venkatesan R. 1999. *Magnetic resonance imaging: physical principles and sequence design*. New York, NY, USA: Wiley-Liss.

Hacke GU, Stiller V, Sperry JS, Pittermann J, McCulloh KA. 2001. Cavitation fatigue. Embolism and refilling cycles can weaken the cavitation resistance of xylem. *Plant Physiology* 125: 779–789.

Herbette S, Wortemann R, Awad H, Huc R, Cochard H, Barigah TS. 2010. Insights into xylem vulnerability to cavitation in *Fagus sylvatica* L. Phenotypic and environmental sources of variability. *Tree Physiology* 30: 1448–1455.

Hesse L, Leupold J, Speck T, Masselter T. 2018. A qualitative analysis of the bud ontogeny of *Dracaena marginata* using high-resolution magnetic resonance imaging. *Scientific Reports* 8: 9881.

Hillabrand RM, Hacke UG, Lieffers VJ. 2016. Drought-induced xylem pit membrane damage in aspen and balsam poplar. *Plant, Cell & Environment* 39: 2210–2220.

Hochberg U, Albuquerque C, Rachmilevitch S, Cochard H, David-Schwartz R, Brodersen CR, McElrone A, Windt CW. 2016. Grapevine petioles are more sensitive to drought induced embolism than stems. Evidence from *in vivo* MRI and microcomputed tomography observations of hydraulic vulnerability segmentation. *Plant, Cell & Environment* 39: 1886–1894.

Hochberg U, Windt CW, Ponomarenko A, Zhang Y-J, Gersony J, Rockwell FE, Holbrook NM. 2017. Stomatal closure, basal leaf embolism, and shedding protect the hydraulic integrity of grape stems. *Plant Physiology* 174: 764–775.

Holbrook NM, Ahrens ET, Burns MJ, Zwieniecki MA. 2001. *In vivo* observation of cavitation and embolism repair using magnetic resonance imaging. *Plant Physiology* 126: 27–31.

Homan NM, Windt CW, Vergeldt FJ, Gerkema E, Van As H. 2007. 0.7 and 3 T MRI and sap flow in intact trees. Xylem and phloem in action. *Applied Magnetic Resonance* 32: 157–170.

Kaufmann Ilja, Schulze-Till Thomas, Schneider Heike U, Zimmermann Ulrich, Jakob Peter. 2009. Functional repair of embolized vessels in maize roots after temporal drought stress, as demonstrated by magnetic resonance imaging. *New Phytologist* 184: 245–256.

Köckenberger W, Pope JM, Xia Y, Jeffrey KR, Komor E, Callaghan PT. 1997. A non-invasive measurement of phloem and xylem water flow in castor bean seedlings by nuclear magnetic resonance microimaging. *Planta* 201: 53–63.

Lechthaler S, Robert EMR, Tonné N, Prusova A, Gerkema E, van As H, Koedam N, Windt CW. 2016. Rhizophoraceae mangrove saplings use hypocotyl and leaf water storage capacity to cope with soil water salinity changes. *Frontiers in Plant Science* 7: 895.

Lemoine D, Cochard H, Granier A. 2002. Within crown variation in hydraulic architecture in beech (*Fagus sylvatica* L). Evidence for a stomatal control of xylem embolism. *Annals of Forest Science* 59: 19–27.

Leuschner C, Meier IC, Hertel D. 2006. On the niche breadth of *Fagus sylvatica*. Soil nutrient status in 50 Central European beech stands on a broad range of bedrock types. *Annals of Forest Science* 63: 355–368.

Ma J, Slavens Z, Sun W, Bayram E, Estowski L, Hwang K-P, Akao J, Vu AT. 2008. Linear phase-error correction for improved water and fat separation in dual-echo dixon techniques. *Magnetic Resonance in Medicine* 60: 1250–1255.

McDowell N, Pockman WT, Allen CD, Breshears DD, Cobb N, Kolb T, Plaut J, Sperry J, West A, Williams DG et al. 2008. Mechanisms of plant survival and mortality during drought. Why do some plants survive while others succumb to drought? *New Phytologist* 178: 719–739.

Melcher PJ, Zwieniecki MA, Holbrook NM. 2003. Vulnerability of xylem vessels to cavitation in sugar maple. Scaling from individual vessels to whole branches. *Plant physiology* 131: 1775–1780.

Metzner R, van Dusschoten D, Bühler J, Schurr U, Jahnke S. 2014. Belowground plant development measured with magnetic resonance imaging (MRI). Exploiting the potential for non-invasive trait quantification using sugar beet as a proxy. *Frontiers in Plant Science* 5: 469.

Ogasa MY, Utsumi Y, Miki NH, Yazaki K, Fukuda K. 2016. Cutting stems before relaxing xylem tension induces artefacts in *Vitis coignetiae*, as evidenced by magnetic resonance imaging. *Plant, Cell & Environment* 39: 329–337.

Pammenter NW, van der Willigen C. 1998. A mathematical and statistical analysis of the curves illustrating vulnerability of xylem to cavitation. *Tree Physiology* 18: 589–593.

Park Williams A, Allen CD, Macalady AK, Griffin D, Woodhouse CA, Meko DM, Swetnam TW, Rauscher SA, Seager R, Grissino-Mayer HD et al. 2013. Temperature as a potent driver of regional forest drought stress and tree mortality. *Nature Climate Change* 3: 292–297.

Petruzzellis F, Pagliarani C, Savi T, Losso A, Cavalletto S, Tromba G, Dullin C, Bär A, Ganthaler A, Miotto A. 2018. The pitfalls of *in vivo* imaging techniques. Evidence for cellular damage caused by synchrotron X-ray computed micro-tomography. *New Phytologist* 220: 104–110.

Press WH. 2002. *Numerical recipes in C++. The art of scientific computing*. Cambridge, UK: Cambridge University Press.

Robert E, Schmitz N, Copini P, Gerkema E, Vergeldt FJ, Windt CW, Beeckman H, Koedam N, van As H. 2014. Visualization of the stem water content of two genera with secondary phloem produced by successive cambia through Magnetic Resonance Imaging (MRI). *Journal of Plant Hydraulics* 1: e006.

Robinson A, Clark CJ, Clemens J. 2000. Using ^{1}H magnetic resonance imaging and complementary analytical techniques to characterize developmental changes in the *Zantedeschia Spreng.* tuber. *Journal of Experimental Botany* 51: 2009–2020.

Savi T, Miotto A, Petruzzellis F, Losso A, Pacilè S, Tromba G, Mayr S, Nardini A. 2017. Drought-induced embolism in stems of sunflower. A comparison of *in vivo* micro-CT observations and destructive hydraulic measurements. *Plant Physiology and Biochemistry* 120: 24–29.

Scheenen TWJ, van Dusschoten D, de Jager PA, Van As H. 2000. Quantification of water transport in plants with NMR imaging. *Journal of Experimental Botany* 51: 1751–1759.

Scheenen TWJ, Vergeldt FJ, Heemskerk AM, Van As H. 2007. Intact plant magnetic resonance imaging to study dynamics in long-distance sap flow and flow-conducting surface area. *Plant Physiology* 144: 1157–1165.

Schild HH. 1992. *MRI made easy:(–well almost)*. Wayne, NJ, USA: Berlex Laboratories.

Scholander PF, Hammel HT, Hemmingsen EA, Bradstreet ED. 1964. Hydrostatic pressure and osmotic potential in leaves of mangroves and some other plants. *Proceedings of the National Academy of Sciences, USA* 52: 119.

Schuldt B, Knutzen F, Delzon S, Jansen S, Müller-Haubold H, Burlett R, Clough Y, Leuschner C. 2016. How adaptable is the hydraulic system of European beech in the face of climate change-related precipitation reduction? *New Phytologist* 210: 443–458.

Schweingruber FH. 1990. *Anatomy of European woods*. Bern, Switzerland: Verlag Paul Haupt.

Stojnic S, Suchocka M, Benito-Garzón M, Torres-Ruiz JM, Cochard H, Bolte A, Cocozza C, Cvjetkovic B, de Luis M, Martinez-Vilalta J *et al.* 2018. Variation in xylem vulnerability to embolism in European beech from geographically marginal populations. *Tree Physiology* 38: 173–185.

Tomasella M, Beikircher B, Häberle K-H, Hesse B, Kallenbach C, Matyssek R, Mayr S. 2018. Acclimation of branch and leaf hydraulics in adult *Fagus sylvatica* and *Picea abies* in a forest through-fall exclusion experiment. *Tree Physiology* 38: 198–211.

Tomasella M, Nardini A, Hesse BD, Machlet A, Matyssek R, Häberle K-H. 2019. Close to the edge. Effects of repeated severe drought on stem hydraulics and non-structural carbohydrates in European beech saplings. *Tree Physiology* 39: 717–728.

Trenberth KE, Dai A, van der Schrier G, Jones PD, Barichivich J, Briffa KR, Sheffield J. 2014. Global warming and changes in drought. *Nature Climate Change* 4: 17–22.

Umebayashi T, Fukuda K, Haishi T, Sotooka R, Zuhair S, Otsuki K. 2011. The developmental process of xylem embolisms in pine wilt disease monitored by multipoint imaging using compact magnetic resonance imaging. *Plant Physiology* 156: 943–951.

Umebayashi T, Morita T, Utsumi Y, Kusumoto D, Yasuda Y, Haishi T, Fukuda K. 2016. Spatial distribution of xylem embolisms in the stems of *Pinus thunbergii* at the threshold of fatal drought stress. *Tree Physiology* 36: 1210–1218.

Utsuzawa S, Fukuda K, Sakaue D. 2005. Use of magnetic resonance microscopy for the nondestructive observation of xylem cavitation caused by pine wilt disease. *Phytopathology* 95: 737–743.

van As H. 2007. Intact plant MRI for the study of cell water relations, membrane permeability, cell-to-cell and long distance water transport. *Journal of Experimental Botany* 58: 743–756.

van As H, Scheenen T, Vergeldt FJ. 2009. MRI of intact plants. *Photosynthesis Research* 102: 213–222.

van As H, van Duynhoven J. 2013. MRI of plants and foods. *Journal of Magnetic Resonance* 229: 25–34.

van de Wal BAE, Windt CW, Leroux O, Steppe K. 2017. Heat girdling does not affect xylem integrity. An *in vivo* magnetic resonance imaging study in the tomato peduncle. *New Phytologist* 215: 558–568.

van der Weerd L, Claessens MMAE, Ruttink T, Vergeldt FJ, Schaafsma TJ, van As H. 2001. Quantitative NMR microscopy of osmotic stress responses in maize and pearl millet. *Journal of Experimental Botany* 52: 2333–2343.

van der Weerd L, Vergeldt FJ, Adrie de Jager P, van As H. 2000. Evaluation of algorithms for analysis of NMR relaxation decay curves. *Magnetic Resonance Imaging* 18: 1151–1158.

Windt CW, Blümler P. 2015. A portable NMR sensor to measure dynamic changes in the amount of water in living stems or fruit and its potential to measure sap flow. *Tree Physiology* 35: 366–375.

Windt CW, Vergeldt FJ, de Jager PA, van As H. 2006. MRI of long-distance water transport. A comparison of the phloem and xylem flow characteristics and dynamics in poplar, castor bean, tomato and tobacco. *Plant, Cell & Environment* 29: 1715–1729.

Windt CW, Vergeldt FJ, van As H. 2007. Correlated displacement-T_2 MRI by means of a Pulsed Field Gradient-Multi Spin Echo Method. *Journal of Magnetic Resonance* 185: 230–239.

Zwieniecki MA, Melcher PJ, Ahrens ET. 2013. Analysis of spatial and temporal dynamics of xylem refilling in *Acer rubrum* L. using magnetic resonance imaging. *Frontiers in Plant Science* 4: 265.

Supporting Information

Additional Supporting Information may be found online in the Supporting Information section at the end of the article.

Fig. S1 The data points of all three beech trees (*Fagus sylvatica*) were grouped together for analysis, to compare the four methods shown in Fig. 6 by means of FITPLC package (sigmodial model and 1000 resamples).

Fig. S2 Conduit diameter distributions of the microscopic cross-sections of beech (*Fagus sylvatica*) shown in Fig. 1 (the respective mean conduit diameters of B1, B2 and B3 are 28.5, 24.9 and 20.2 µm, respectively).

Table S1 r^2, slopes and Ψ_{50} of vulnerability curves of three beech (*Fagus sylvatica*) trees shown in Fig. 6.

Videos S1–S3 Videos of embolism formation in beech (*Fagus sylvatica*); shown are time series of magnetic resonance product ($A \times T_2$) images of the stem of three beech trees, acquired during progressive dry-down.

Please note: Wiley Blackwell are not responsible for the content or functionality of any Supporting Information supplied by the authors. Any queries (other than missing material) should be directed to the *New Phytologist* Central Office.

2.2 Publication II: Reduced spatial resolution MRI suffices to image and quantify drought induced embolism formation in trees

Marco Meixner, Petra Foerst, Carel Windt

<u>Background</u>

Magnetic resonance imaging (MRI) can be used to monitor xylem embolism formation in trees non-invasively and with high temporal resolution, even if individual xylem conduits cannot be spatially resolved. Quantitative magnetic resonance images of water content and signal relaxation time (T_2) are especially useful, since they provide information about the sample beyond the limited spatial resolution of most small-scale MRI approaches. When affordable low field MRI devices are used, spatial resolution is particularly costly in measurement time, as well as weight and price of the hardware. In this contribution it has been examined how much spatial resolution can be sacrificed without losing the ability to detect and quantify drought induced xylem emboli. For this purpose, a young spruce and a young beech tree were dehydrated inside a small-scale magnetic resonance imager, while they were continuously imaged at three different spatial resolutions. The dry-down experiment was succeeded by obtaining microscopy images at the same stem position where the MR imaging had been conducted.

<u>Results</u>

It was found that quantitative magnetic resonance images with a pixel size larger than 0.5*0.5 mm² still permit an approximate localization of embolism formation in angiosperm and gymnosperm xylem architecture, as well as the generation of accurate vulnerability curves via binarization. It was found that it is beneficial to adapt the binarization threshold to a particular measurement in terms of spatial resolution and species. Accordingly, spatial resolution can be traded off against the ability to image much more rapidly, or with significantly reduced hardware demands. Imaging at a higher time resolution can be beneficial in the context of certain research questions, regarding the dynamics of xylem dry-down or refilling, and to improve the accuracy when fitting vulnerability curves. Reduced hardware demands may allow for the use of smaller permanent magnets, as well as gradient amplifiers, and therefore potentially bring down the cost and weight of MRI scanners for monitoring and quantifying embolism formation in trees non-invasively.

<u>Author contributions</u>

Marco Meixner and Carel Windt designed, built and programmed the magnetic resonance imager. Marco Meixner performed the experiments and analyzed the data. Marco Meixner and Carel Windt wrote the manuscript with contributions from Petra Foerst.

Reduced spatial resolution MRI suffices to image and quantify drought induced embolism formation in trees

Marco Meixner[1,2], Petra Foerst[1] and Carel W. Windt[2]*

Abstract

Background: Magnetic resonance imaging (MRI) is uniquely suited to non-invasively and continuously monitor embolism formation in trees. Depending on the MRI method used, quantitative parameter maps of water content and MRI signal relaxation behavior can be generated. The ability to measure dynamic differences in water content and relaxation behavior can be used to detect xylem embolism formation, even if xylem conduits are too small to be spatially resolved. This is especially advantageous when using affordable small-scale low-field MRI scanners. The amount of signal that can be obtained from an object strongly depends on the strength of the magnetic field of the imager's magnet. Imaging at lower resolutions thus would allow to reduce the cost, size and weight of the MRI scanner and to shorten image acquisition times.

Results: We investigated how much spatial resolution can be sacrificed without losing the ability to monitor embolism formation in coniferous softwood (spruce, *Picea abies*) and diffuse porous beech (*Fagus sylvatica*). Saplings of both species were bench dehydrated, while they were continuously imaged at stepwise decreasing spatial resolutions. Imaging was done by means of a small-scale MRI device, utilizing image matrix sizes of 128×128, 64×64 and 32×32 pixels at a constant FOV of 19 and 23 mm, respectively. While images at the lowest resolutions (pixel sizes 0.59×0.59 mm and 0.72×0.72 mm) were no longer sufficient to resolve finer details of the stem anatomy, they did permit an approximate localization of embolism formation and the generation of accurate vulnerability curves.

Conclusions: When using MRI, spatial resolution can be sacrificed without losing the ability to visualize and quantify embolism formation. Imaging at lower spatial resolution to monitor embolism formation has two advantages. Firstly, the acquisition time per image can be reduced dramatically. This enables continuous imaging at high time resolution, which may be beneficial to monitor rapid dynamics of embolism formation. Secondly, if the requirements for spatial resolution are relaxed, much simpler MRI devices can be used. This has the potential to make non-invasive MR imaging of embolism formation much more affordable and more widely available.

Keywords: Magnetic resonance imaging, MRI, NMR, Spatial resolution, Xylem, Embolism, Vulnerability curve, Small-scale, Low field

Background

During the last couple of decades two non-invasive imaging methods emerged that allow the visualization and quantification of embolism formation and spread in plant xylem: High-resolution computed tomography (HRCT, also referred to as micro-CT) and MRI. For both imaging modalities methods have been developed to determine

*Correspondence: c.windt@fz-juelich.de
[2] IBG-2: Plant Sciences, Forschungszentrum Jülich, Jülich, Germany
Full list of author information is available at the end of the article

Meixner *et al. Plant Methods*   (2021) 17:38

Page 2 of 12

the percentage loss of xylem conductivity (PLC) due to the cavitation of xylem conduits. This is done by measuring, directly or indirectly, the amount of conducting xylem area that is lost.

HRCT currently is the most widely used method, known for the excellent spatial resolution it affords. It is capable of resolving individual xylem conduits, even in tree species with small conduit diameters. This allows to determine what conduits were filled before dry-down, which conduits cavitate during dry-down, and to estimate their conductivity (and loss thereof) on the basis of their diameters, in combination with the Hagen-Poiseuille law. This has been done for eucalyptus [1], grapevine [2]and walnut [3]. An important drawback of HRCT, however, is the use of ionizing radiation. Depending on the dosage, it may damage living tissue [4], disrupt cellular function [5] and cause growth inhibition [6]. Therefore, while it is an excellent tool to visualize embolized conduits in high spatial detail, it is not an ideal choice to monitor dynamic processes that require repeated or long-term imaging with large numbers of exposures [7].

For the latter purpose MRI, on the other hand, is especially well suited. It does not rely on the absorption of ionizing radiation by the sample, but is based on the principle of nuclear magnetic resonance (NMR). The energy deposition that is associated with MRI of small samples such as plant stems is negligible, especially at low magnetic fields. Therefore, samples can be imaged non-invasively, for periods of months and with a virtually unlimited number of image acquisitions. Examples of such-long term experiments are imaging of flow and water distribution in a tree stem over a period of multiple seasons [8] or imaging of sap flow towards a developing tomato truss [9]. Using the appropriate hardware and imaging pulse sequences, parameter maps can be obtained that quantitatively represent NMR parameters such as amplitude (A) and T_2 [10]. The amplitude maps acquired in the current study thus linearly and quantitatively reflect water content, and are not merely weighted by it (for further details see [10, 11]).

MRI usually cannot match the resolution offered by HRCT. The resolution that can be achieved by means of MRI is limited by the size of the sample, which usually dictates the smallest field of view (FOV) that can be used, and the number of pixels that can be acquired in that FOV. Reducing the FOV to zoom in on parts of an object in most cases is not possible, as signal from parts of the object that are outside of the FOV would fold back in, corrupting the image. The number of pixels (voxels) that can be encoded in a FOV is then defined by the strength and homogeneity of the magnetic field, as well as the strength of the imaging gradients, but almost never is chosen higher than 512×512. For plants matrix size typically is 256×256 or lower (for a more detailed explanation of the tradeoffs involved, please see the theory section). This means that in practice, even for samples measuring no more than 10 mm in diameter, it will be hard to exceed an in-plane resolution of 40×40 µm. MRI thus can only resolve xylem conduits in species or organs with wide vessels, as has been demonstrated for woody lianas [12], grapevine [2, 14–15], cucumber [16] and roots of maize [17].

To circumvent the problems imposed by this resolution limit, various techniques were developed to detect xylem embolism formation indirectly. In plants, the MR signal almost exclusively originates from protons of water molecules. This fact can be used to generate parameter maps that quantitatively reflect water content, relaxation behavior, diffusion or flow, or parameter maps that are merely weighted by one or more of these parameters. PLC has been calculated or estimated on the basis of parameter maps in a number of ways. One approach is to base PLC on the change in pixel brightness of water content weighted MR amplitude images [18]. PLC values have also been derived from binarizing various types of MR parameter maps. In the binarization approach the loss of xylem conductivity is estimated from the decline in the number of pixels above a chosen threshold, plotted in dependence of the xylem water potential. Binarization has been applied to different types of MR parameter maps, such as signal intensity maps [19–20] or quantitative water content maps [14]. In Meixner et al. [11] we obtained PLC values of beech saplings on the basis of binarizing A^*T_2 product images, obtained by pixel-wise multiplication of water content images (A) and signal relaxation time images (T_2). In A^*T_2 product images even low numbers of filled xylem vessels per pixel easily became detectable, as well as their disappearance due to cavitation; and the binarization of A^*T_2 product images resulted in accurate xylem vulnerability curves. Using this approach, detection of embolism formation and the quantification of xylem vulnerability curves could be done, despite the fact that pixels were five times larger than the average conduit diameter in beech.

There are two important benefits that may be had by imaging xylem dry-down at a lower than usual spatial resolution: MRI hardware can be scaled down in size and weight, and images can be acquired more rapidly. We recently demonstrated that imaging embolism formation is possible, even when using a mobile small-scale, low-field MRI scanner [11, 21]. The imagers used in these cases were based on a 16 kg permanent magnet. Integrated onto a trolley, the whole system weighed 45 kg and could easily be handled by a single person, even in the field [21]. While this system can already be considered mobile, reducing spatial resolution would enhance

mobility even further. If resolution is reduced, a lower magnetic field strength suffices to achieve the same signal-to-noise ratio (SNR), allowing lighter and cheaper permanent magnets to be used. A reduction in resolution would also allow the use of lighter and less powerful gradient amplifiers and therefore permit the development of low-cost imaging equipment that is even more lightweight and mobile. Another advantage when reducing spatial resolution is the ability to image more rapidly, which allows the acquisition of more PLC values per unit time, permitting higher accuracy when fitting vulnerability curves [22]. In addition, high temporal resolution dry-down movies can be generated which allow the investigation of embolism spread within and between annual rings [14, 19], even when this spread proceeds rapidly [18].

In this study we investigate if MRI spatial resolution can be reduced significantly, without losing the ability to detect and quantify embolism formation. To this end, we bench dehydrated spruce (*Picea abies*) and beech (*Fagus sylvatica*) saplings in a small-scale MRI system. During dry-down the plants' main stems were imaged continuously at three stepwise decreasing spatial resolutions. We tested whether timing and location of embolism formation during dry-down can be monitored and vulnerability curves can be obtained, even if pixel sizes are much (up to thirty times) larger than the average xylem conduit diameter.

Theory: benefits of imaging at lower spatial resolutions

MR imaging experiments always involve a trade-off between spatial resolution, signal-to-noise ratio (SNR) and imaging time. The benefits of using a lower spatial resolution are illustrated by the following equation [23]:

$$\text{SNR/pixel} \propto A_{pix} B_0 \left(\frac{N_{avg}}{SW/(N_{fq} * N_{ph})} \right)^{1/2}. \quad (1)$$

Neglecting signal decay over time due to spin–spin or spin–lattice interactions, Eq. 1 illustrates how increasing the pixel area (A_{pix}, i.e. a decrease in matrix size $N_{fq} \times N_{ph}$ at constant FOV) can compensate for: (i) the use of magnets of a lower magnetic field strength (B_0); (ii) imaging with a lower number of averages (N_{avg}); or (iii) imaging at a higher spectral width (SW). If lower magnetic fields are permitted, the magnets that provide the main magnetic field can become smaller and lighter. For example, imaging at a matrix size of 32×32 pixels instead of at 128×128, i.e. lowering spatial resolution by a factor of four while keeping all other imaging parameters the same, would allow the use of a four times weaker

magnetic field B_0, while achieving the same SNR per pixel in the same imaging time.

Alternatively, imaging at lower spatial resolutions would also allow measurements with higher temporal resolution. On the one hand because at lower resolution the number of phase encoding steps (N_{ph}) is lower, but also because the number of averages (N_{avg}) can be lowered, decreasing image acquisition time. Imaging at higher spectral width (SW) also facilitates mobile imaging in the field. It allows the use of magnets of lower homogeneity and ensures tolerance against the effects of temperature changes and magnet handling on the magnet's homogeneity during transport and field use [11, 24].

Apart from the static and homogeneous magnetic field (B_0) magnetizing the sample, MRI also requires switched magnetic field gradients to spatially encode the MR signal. The frequency width of a pixel ($\Delta \nu$) is determined by the gradient strength (G), the pixel width in real space (Δr) in the encoding direction and the gyromagnetic constant for hydrogen (γ).

$$\Delta \nu = \gamma G \Delta r \quad (2)$$

The minimum value that is acceptable for $\Delta \nu$ is, amongst other factors, determined by the homogeneity of the magnet. The more homogeneous the magnet, the lower $\Delta \nu$ is allowed to be. Small-scale magnets that are exposed to temperature changes and handling, however, require higher $\Delta \nu$ values and therefore more powerful imaging gradients (G). The need for strong and fast gradient pulses in turn limits the mobility of the MR imager. Strong and fast gradient pulses require large and heavy gradient amplifiers. For mobile systems this is particularly relevant, since the gradient amplifiers constitute the largest and heaviest hardware components of an imager, besides the magnet. Keeping all other imaging parameters unchanged, a four times reduction in imaging resolution would lower the gradient strength required by a factor of four. Imaging at lower spatial resolutions (higher values of Δr) thus also allows for the use of smaller, lighter, cheaper and more mobile gradient amplifiers.

Materials and methods

Plant materials and treatment

A potted 3-year-old spruce sapling (*Picea abies*, 82 cm high, 16 mm stem diameter at measurement position) was purchased from a local nursery (Pflanzenwelt Biermann, Trangstedt, Germany), as was a 3-year-old beech sapling (*Fagus sylvatica*, 161 cm high, 16 mm stem diameter at measurement position, Baumschule Leonhard Veith, Merzenich-Golzheim, Germany). Both trees were subsequently grown in a greenhouse at 20 °C day (16 h) and 16 °C night (8 h) temperature, provided with

Meixner *et al. Plant Methods*   (2021) 17:38

Page 4 of 12

supplemental light (250 W, Philips IP65 metal halogen vapor lamps) and kept well-watered by means of drip irrigation.

For the dry-down treatment the trees were moved to the lab. MRI scanning was started when the tree was still intact, for the spruce tree 11 h and for the beech tree 9 h prior to the initiation of dry-down, which was done by cutting the stems 5 cm above the soil (for a schematic representation of the experiment, see Fig. 1a). During the entire experiment the trees were illuminated by a sodium vapor lamp (SON-T Agro 400 W, Philips) and kept at a temperature of 22 °C during the day (12 h) and 18 °C at night (12 h). The dry-down experiment was continued until the xylem was completely embolized, which took 47 h in case of spruce and 18 h for beech. The spruce dry-down experiment was performed in the first half of February 2019, the beech dry-down experiment in the middle of June 2019.

MRI hardware and methods

The MRI scanner comprised a custom, small-scale C-shaped permanent magnet (0.25 T, 16 kg), a custom plane parallel gradient set with a maximum gradient strength of 0.3 T/m and a Kea II spectrometer (Magritek,

Wellington, New Zealand), equipped with a built-in 100 W RF amplifier. The gradient set was driven by three BAFPA40 gradient amplifiers (BRUKER, Rheinstetten, Germany). Inside the gradient system a 20 mm solenoidal RF coil with tuning mechanism was mounted. For full details on the system see Meixner et al. [11].

After winding the radio frequency (RF) coil around a Teflon former, placed on the stem (at heights of 37 and 78 cm for spruce and beech respectively), the plants were slid into the probe head of the MRI scanner. Both trees were fixed relative to the imager by means of three metal clamps, positioned below and above the magnet, and near the position where the tree was cut. For both measurements, a glass reference tube with an inner diameter of 1.7 mm, filled with nickel nitrate doped water and a T_2 value of 112.4 ms, was attached to the stem inside of the RF coil. To minimize external RF noise the magnet was covered with an earthed silver-plated copper mesh.

A multi-spin echo (MSE) pulse sequence was employed as previously described in full detail by Meixner et al. [11], acquiring 64 echoes with an echo time of 4 ms for the first echo and 2.1 ms for all subsequent ones. Excitation was done by means of a slice selective 90°, 500 μs 5-lobe sinc pulse; refocusing by means of hard, 13 μs non-slice selective 180 degree pulses. For all measurements, the spectral width was 100 kHz, the slice thickness 5 mm, the dwell time 10 μs, the number of averages 4 and the repetition time 1.5 s. The field of view (FOV) was 19×19 mm for spruce and 23×23 mm for beech. Both plants were imaged continuously, acquiring sets of three images of increasing matrix size (32×32, 64×64 and 128×128 pixels) and measurement time (3.5, 7.2 and 14.6 min, see Fig. 1). The resulting in-plane resolutions in mm were 0.59×0.59, 0.30×0.30 and 0.15×0.15 for spruce, and 0.72×0.72, 0.36×0.36, 0.18×0.18 for beech, respectively. By continuously repeating this block of three measurements three time series with different spatial resolutions were acquired, each with the same temporal resolution of 25.3 min (Fig. 1a).

Data processing

A flow chart of the image processing workflow is given in Fig. 1b. The higher resolution images (matrix sizes 64×64 and 128×128) were of lower SNR than desired for our purposes (Additional file 1). In order to raise SNR, a sliding window averaging approach was applied, averaging up to eight consecutive measurements of the same spatial resolution. Prior to sliding window averaging all images were corrected for small position changes of the tree during the dry-down. This was done by iteratively shifting each image pixel-wise in the x- and y-direction, looking for the position at which the smallest difference is found between the shifted image and the first image of

Fig. 1 Flow charts of the sequence of events during the dry-down experiment (**a**) and of the image- and data processing workflow (**b**). Images were acquired continuously and at matrix sizes of 32×32, 64×64 and 128×128 pixels

Meixner *et al. Plant Methods*   (2021) 17:38

Page 5 of 12
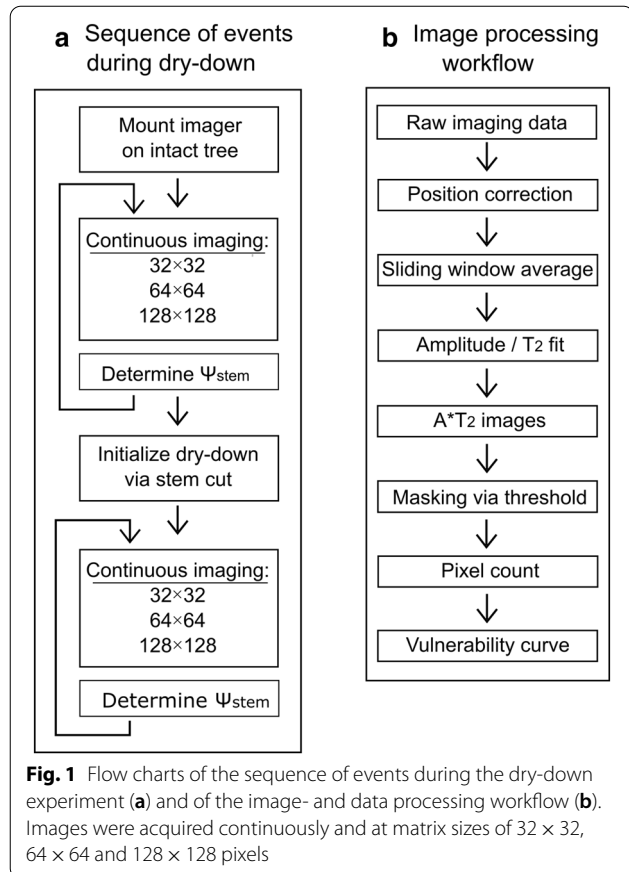
each time series. This difference was calculated by subtracting the current image in the time series from the first image, then taking the sum total of the absolute values of all pixels. After sliding window averaging all resulting images were phase corrected according to Ma et al. [25]. Subsequently, quantitative water content (A) and signal relaxation (T_2) maps were obtained by mono-exponentially fitting the echo train of each image of the measurement time series in a pixel-by-pixel manner [26]. Prior to fitting, handmade masks were applied which only included the tree stem. $A*T_2$ parameter maps were calculated by multiplying amplitude (A) and T_2 images, again pixel-by-pixel (Fig. 2).

When generating dry-down movies via sliding window averaging of one, two, four or eight images, fitting errors in the form of erroneous, bright pixels were filtered out. This was done by setting pixels to zero that have double or more, or less than half the value of all four nearest neighboring pixels.

Calculation of vulnerability curves

To generate vulnerability curves (VCs), the decline in xylem functionality was estimated from $A*T_2$ product images and plotted as a function of stem water potential (Ψ_{stem}). The latter was measured with a Scholander Chamber (Model 1000, PMS Instrument Company, Albany, USA). Throughout the dry-down, randomly chosen small twigs were carefully bagged with cling foil and aluminum foil (the latter to put the leaves in complete darkness) and left to equilibrate for 15 min. The twigs were then excised, quickly transferred to the instrument and measured. For spruce, 61 water potential values were measured over the course of four days, whereas during the more rapid dry-down of beech 26 water potential values were taken over a period of 26 h.

During the dry-down experiments, the percentage of embolized xylem conducting area was obtained by binarizing $A*T_2$ product images. This was done by matching the center of the sliding window temporally to the water potential measurements and counting the number of pixels (P_{abv}) above a binarization threshold, the value of which was determined by an optimization approach. Thresholds were iteratively applied to each dry-down series of images and the r^2 of the sigmodial fits of the resulting dry-down curves compared, until an optimal solution (maximum r^2) was found. For the three matrix sizes (32×32, 238 64×64, 128×128) this resulted in threshold values of 0.2, 0.1, 0.1 for spruce, and 1.4, 1.3, 1.3 for beech, respectively. After binarization, the P_{abv} values were normalized from 0 to 100% according to $\%_{emb} = 100 * \frac{P_{initial} - P_{abv}}{P_{initial} - P_{min}}$, with P_{abv} referring to the initial and P_{min} to the minimum number of pixels above the binarization threshold of a time series of images. The VC
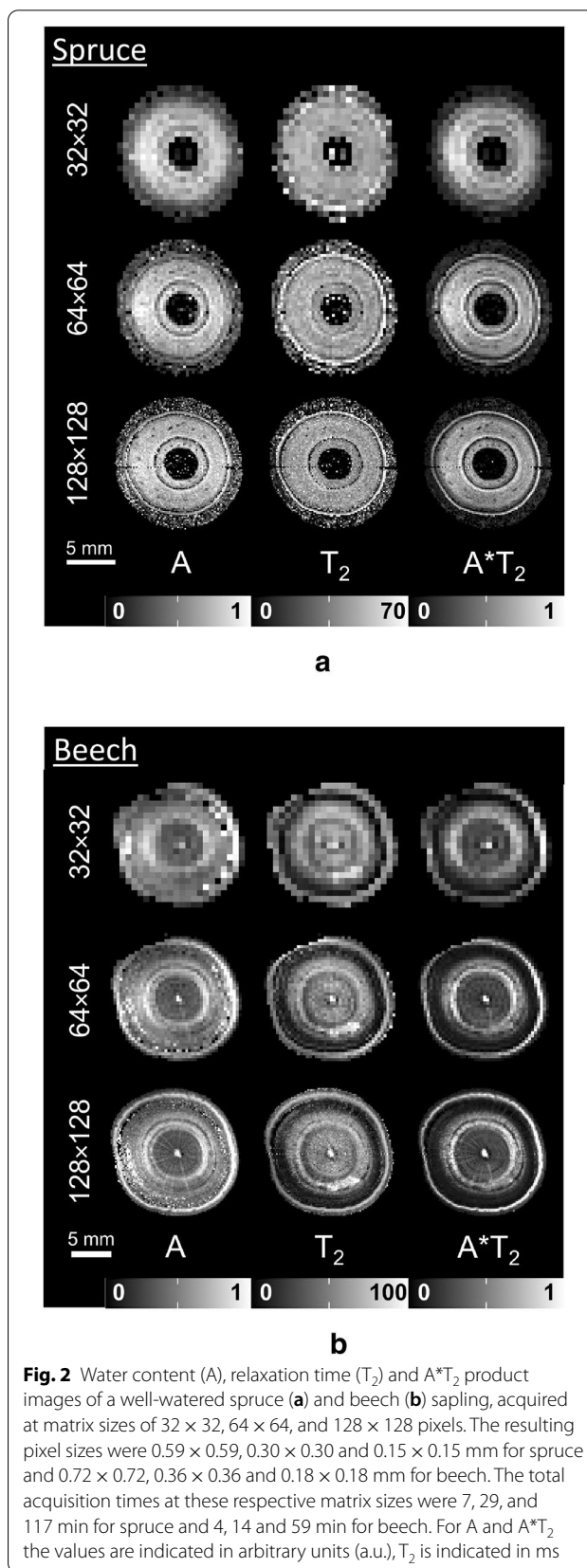
Fig. 2 Water content (A), relaxation time (T_2) and $A*T_2$ product images of a well-watered spruce (**a**) and beech (**b**) sapling, acquired at matrix sizes of 32×32, 64×64, and 128×128 pixels. The resulting pixel sizes were 0.59×0.59, 0.30×0.30 and 0.15×0.15 mm for spruce and 0.72×0.72, 0.36×0.36 and 0.18×0.18 mm for beech. The total acquisition times at these respective matrix sizes were 7, 29, and 117 min for spruce and 4, 14 and 59 min for beech. For A and $A*T_2$ the values are indicated in arbitrary units (a.u.), T_2 is indicated in ms

Meixner *et al. Plant Methods* (2021) 17:38

Page 6 of 12

was obtained by fitting a sigmodial function in dependence of the measured xylem water potential (Ψ_{xylem}):

$$\%_{emb}(\Psi_{xylem}) = 100/\left(1 + \exp\left(\frac{S}{25}(\Psi_{xylem} - \Psi_{50})\right)\right)$$

[22], with the fit parameters indicating how quickly the dry down progressed through the xylem (slope: S) and the water potential at which 50% of the initially filled xylem was embolized (Ψ_{50}). Normalization and sigmodial fitting were performed with Matlab (Mathworks, Natick, USA). Fitting errors were calculated as described by Press [27].

Microscopy

After the dry-down experiment, the imaged stem pieces were marked, excised and stored in 75% ethanol (after previously equilibrating them in 25% and 50% ethanol for 24 h each). Transverse sections of 20 μm were prepared with a sliding microtome (GSL1, Schenkung Dapples, Zürich, Switzerland) and stained with a 1:1 (v/v) mixture of safranin and astrablue, following Gärtner and Schweingruber [28]. Images of the cross section were obtained with a digital camera (DFC 320, Leica, Cambridge, UK), connected to a light microscope (DM2500, Leica Microsystems GmbH, Wetzlar, Germany).

Results and discussion

What xylem anatomical detail can be resolved at decreasing spatial resolution?

In spruce, water filled xylem could easily be distinguished from cambium and bark, even at a pixel size of 0.59×0.59 mm (matrix size 32×32 in Fig. 2a). Individual year rings, however, were only resolved at a pixel size of 0.30×0.30 mm (matrix size 64×64) and better. The cambium is the brightest tissue in the T_2 images, where it showed maximum contrast against the surrounding tissue. The border between cambium and xylem, however, appearing as a black ring both in water content (amplitude, A) and T_2, was only resolved at pixel sizes of 0.30×0.30 mm (matrix size 64×64) and 0.15×0.15 mm (matrix size 128×128). The homogeneous distribution of water inside the filled xylem was similar to that previously imaged in pine stems [20, 29].

In beech, at all pixel sizes the filled xylem could be distinguished from the cambium due to a dark region between cambium and filled xylem (Fig. 2b). Similar to spruce, individual year rings could only be recognized at pixel sizes of 0.36×0.36 mm (matrix size 64×64) and better. In the microscopic images of beech (Fig. 4b), the sapling showed two complete growth rings, and a narrow region of early wood of a third growth ring inside of the cambium, which had formed during the current year. At all matrix sizes xylem containing filled vessels could be distinguished from non-filled xylem on the basis of higher water contents (40 to 60%), but could be identified even more clearly by long T_2 (60 to 80 ms) and A^*T_2 values. Filled xylem was not found in all year rings, but only became visible in the middle of the second growth ring. Comparable water content and T_2 values for filled and embolized xylem in beech were found in Meixner et al. [11]. Merela et al. [30] observed similar water content distribution patterns in the stem of a beech sapling (please note that in this example the amplitude images were water content weighted, but did not reflect water content quantitatively). The absence of filled vessels in the newly formed xylem may indicate that the plant experienced drought stress [31], or had been repotted in spring 2019.
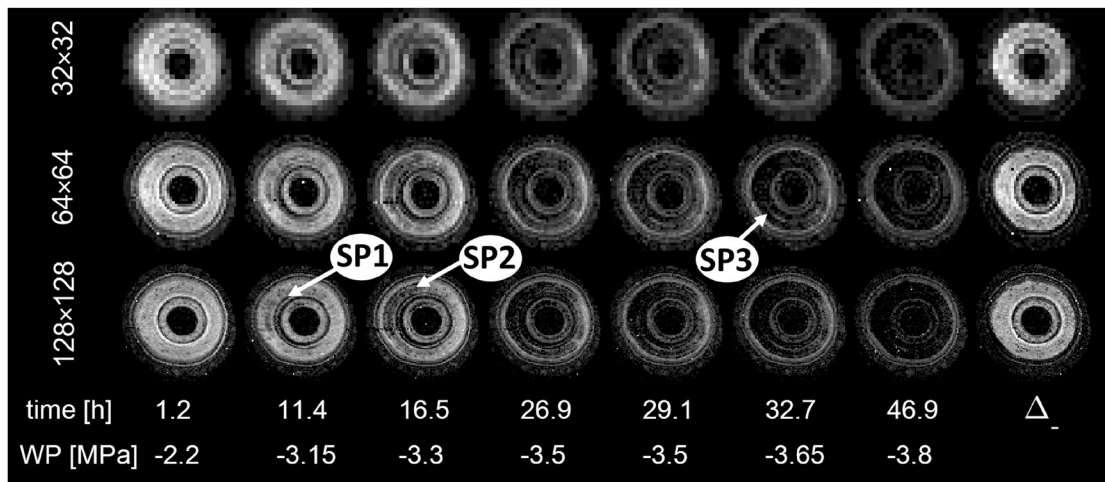
Most of the finer details of the xylem anatomy of both beech and spruce thus were already resolved at a pixel size of 0.30×0.30 mm in spruce and 0.36×0.36 mm in beech (in both cases, at a matrix size of 64×64). Pixel sizes of 0.59×0.59 mm in spruce and 0.72×0.72 mm in beech (matrix size of 32×32) were sufficient to identify filled xylem.

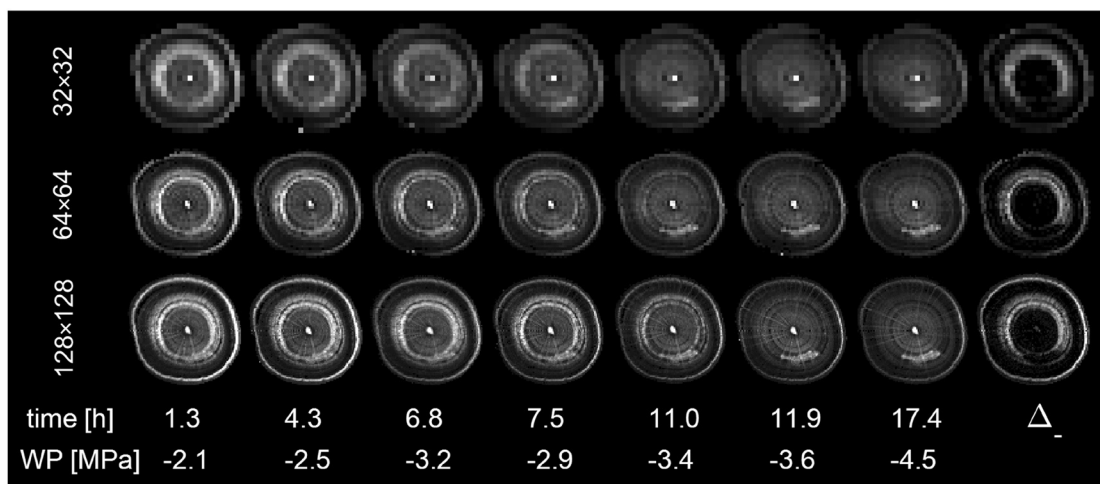### Spatio-temporal characterization of the xylem dry-down at decreasing spatial resolution

The A^*T_2 product images provided an effective means to monitor dry-down for all three matrix sizes in both xylem anatomies (Fig. 3a, b). In Meixner et al. [11] it was shown that both water content and T_2 images can be used to detect xylem cavitation in beech, but that T_2 maps are especially sensitive to it. By multiplying the parameter maps of water content (A) and T_2, A^*T_2 product maps were obtained, in which regions with filled vessels in beech could be identified even more clearly. In the current study we show that in coniferous wood the same approach is effective as well. The presence of filled xylem conduits gave rise to bright A^*T_2 regions, just like in beech, while dry-down manifested
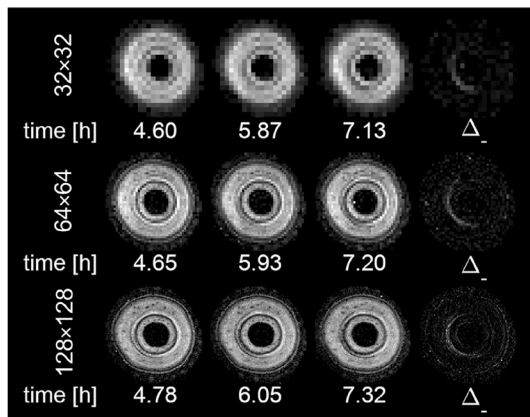
(See figure on next page.)

Fig. 3 A^*T_2 product maps of xylem embolism formation in spruce (**a**) and beech (**b**). Images were acquired with matrix sizes of 32×32, 64×64 and 128×128 pixels, resulting in pixel sizes of 0.59×0.59, 0.30×0.30 mm and 0.15×0.15 for spruce and 0.72×0.72, 0.36×0.36 and 0.18×0.18 mm for beech). Below the parameter maps desiccation time and water potential (WP) are shown. The concomitant water content and T_2 images are provided in Additional file 2. Imaging continuously allowed for resolving finer spatio-temporal details of embolism formation. In (**c**) the first emboli forming in spruce are shown, in panel (**d**) the completion of xylem dry-down in beech. In all panels (**a**–**d**), the difference in image intensity between the first and the last image is shown in the rightmost position (Δ_-)
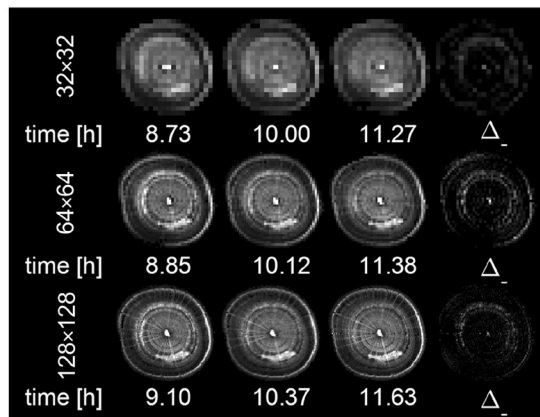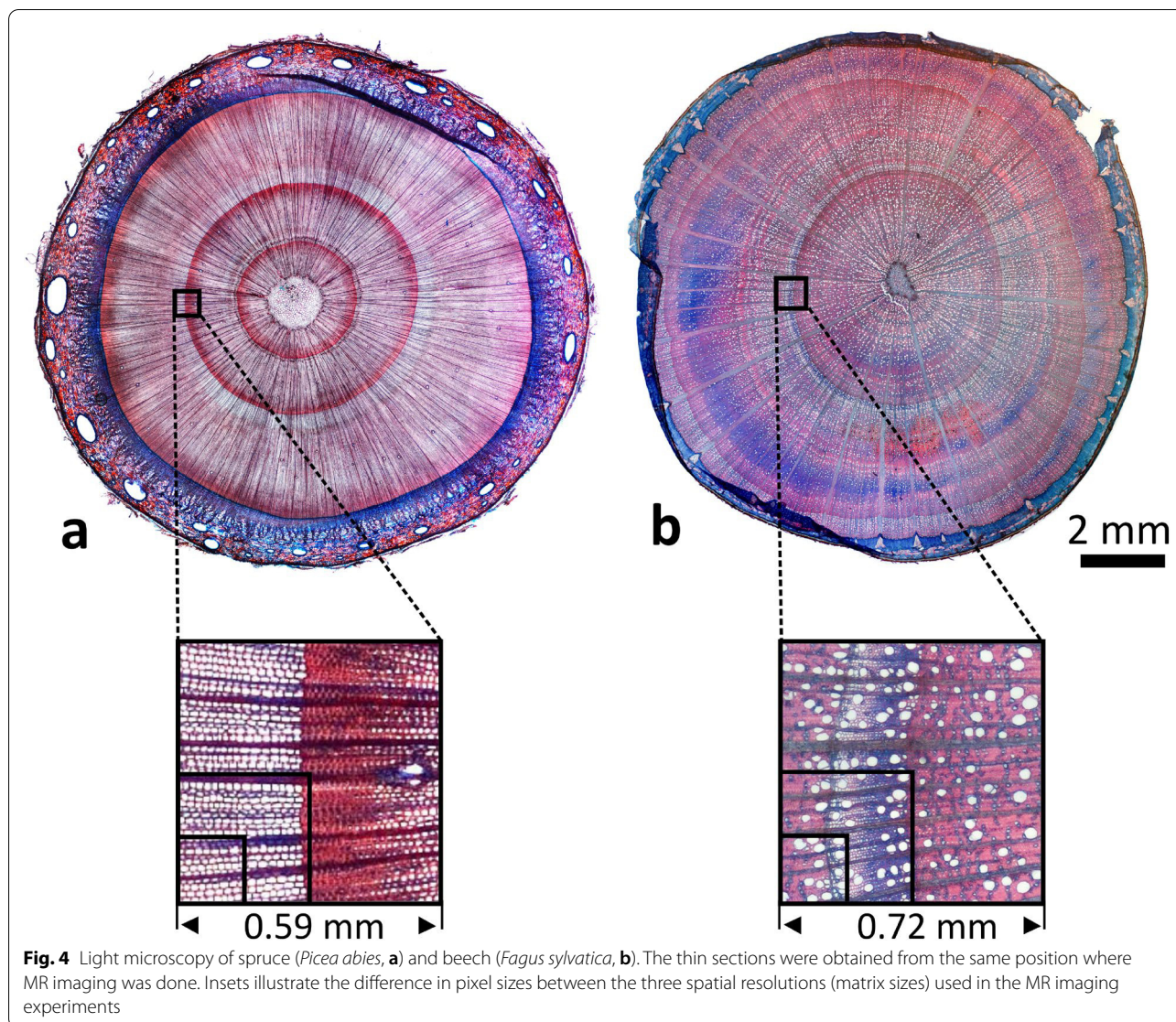
a

b

c

d

Fig. 4 Light microscopy of spruce (*Picea abies*, **a**) and beech (*Fagus sylvatica*, **b**). The thin sections were obtained from the same position where MR imaging was done. Insets illustrate the difference in pixel sizes between the three spatial resolutions (matrix sizes) used in the MR imaging experiments

itself as a strong decrease in A^*T_2 values (Fig. 3a). In the following the dry-down of both species was therefore monitored on the basis of A^*T_2 maps.

In the A^*T_2 product maps of spruce, independent of matrix size, the first emboli could be distinguished at a water potential of − 3.15 MPa, 11.4 h after dry-down initiation (Fig. 3a). Embolism formation started in the current annual ring and at the border of the neighboring second ring (Fig. 3a, arrow SP1). From this region emboli spread, first radially and then tangentially within the outer annual ring (arrow SP2), and after 16.5 h emboli also started forming in the neighboring ring. Another detail that was visible at all three spatial resolutions was a narrow strip of xylem that remained hydrated in the outer annual ring, while the xylem

tissue surrounding it appeared empty (arrow SP3). After 46.9 h (− 3.8 MPa) nearly all xylem was embolized (Fig. 3a).

In beech, emboli started forming only a few hours after cutting the plant at its base (Fig. 3b). Embolism formation manifested itself in the form of a gradual decline in A^*T_2 pixel intensities. Filled xylem, which was found only in the middle of the second growth ring, cavitated within a short time window, between hour 7.5 and 12.0. Dry-down appeared gradual and spread uniformly over the entire filled xylem, indicating that vessels cavitated in an independent, rather than in a clustered manner. Embolism spread in a tangential and radial pattern, as observed by Meixner et al. [11] within beech, was not detected.

On the basis of difference images, even at the lowest spatial resolution, it was possible to detect embolism events that play out in a time window of only a few hours (see Δ_--maps in Fig. 3c, d). In spruce it was shown that the onset of embolism formation, which took place in the early wood of the outer annual ring, happened between hour 5 and 8 after initiation of the dry-down (Fig. 3c). In beech at the lowest spatial resolution it could be shown that the final phase of the xylem dry-down happened between hour 9 and 12 (Fig. 3d). A striking difference between the sequences of A^*T_2 product images of both species was that in the xylem of spruce almost no intensity was left in the images after complete dry-down, whereas in beech always a significant amount of background signal was left visible. This reflects the differences in xylem anatomy of spruce and beech. In spruce, the xylem for the largest part consists of tracheids, and contains, apart from resin ducts, almost no other tissue types or living cells [32] (Fig. 4a). After cavitation of the tracheid, the amount of remaining water in the tracheid walls was either too little to be recognized, or its T_2 value was too short to be detected. In beech, to the contrary, the bulk of the xylem consists of narrow fibers with thick walls, interspersed between the vessels (Fig. 4b). This pool of water remained visible and, with an average T_2 value of ~ 25 ms, was detected in the stem, even when surrounding vessels cavitated.

For an animated illustration of the observations mentioned in this section a tableau of nine videos are provided for both plants as supplementary material (Additional file 3a, 4b).

Are low resolution images sufficient to obtain xylem vulnerability curves?

For spruce and beech, xylem vulnerability curves (VCs) were successfully obtained via binarizing A^*T_2 product images of all three spatial resolutions. For both species, the binarization masks at different matrix sizes were consistent in the location and timing where xylem desiccation was observed (Fig. 5a, b). VCs based on those binarization masks showed r^2 values > 0.90 and yielded comparable Ψ_{50} values. At matrix sizes of 32×32, 64×64, 128×128 for spruce values of -3.8, -4.0 and -4.0 MPa were found, for beech -3.4, -3.5 and -3.5 MPa, respectively (Fig. 5c–h).

The Ψ_{50} values found for beech at the different matrix sizes were in close agreement with one another, as well as with values obtained in other studies on beech saplings (Caquet et al. [33]: -3.0 to -4.0 MPa; Aranda et al. [34]: -3.0 to -3.7 MPa; Meixner et al. [11]: -3.2 to -3.8 MPa) and mature beech trees (Lemoine et al. [35]: -2.2 to -3.1 MPa; Herbette et al. [36]: -3.0 MPa; Schuldt et al. [37]: -3.3 to -3.7 MPa; Stojnic et al. [38]: -2.9 to 3.5 MPa; Tomasella et al. [39]: -2.5 MPa). For spruce, the Ψ_{50} values obtained in the current study were slightly higher than those obtained in other studies on spruce saplings (Mayr et al. [40]: -4.38 MPa; Chmura et al. [41]: -4.27 MPa), but lower or in agreement with values found for mature trees (Cochard [42]: -3.5 MPa; Tomasella et al. [39]: -4.01 MPa). Hence, we conclude that xylem dry-down can be quantified accurately on the basis of MR images, even if their spatial resolution is low and pixels are much larger than xylem conduit diameters.

Conclusions

In this study we demonstrated that MR imaging at low spatial resolution (pixel sizes $> 0.5 \times 0.5$ mm) suffices to detect and image the formation of xylem emboli in spruce and beech, and that these images can be used to quantify embolism formation by means of xylem vulnerability curves. While images with a matrix size of 32×32 (pixel sizes of 0.59 to 0.72 mm) were not sufficient to spatially resolve the annual rings or finer details of the stem anatomy, they did permit an approximate localization of embolism formation (e.g. to differentiate older and younger xylem tissue on the basis of their position in the stem).

The ability to obtain meaningful data and vulnerability curves from quantitative but low-resolution images can be utilized in two ways. Firstly, by imaging at lower spatial resolution the acquisition time per image can be reduced dramatically. This enables continuous imaging at high time resolution, which may be beneficial to monitor rapid dynamics of embolism formation, for example during bench dehydration. Secondly, if the requirements for spatial resolution are relaxed, much simpler MRI devices can be used. Such imagers can be based on much weaker and therefore smaller and lighter permanent magnets, as well as on smaller and lighter gradient amplifiers. For example, keeping all other imaging parameters constant, accepting a four times lower imaging resolution

---

(See figure on next page.)

Fig. 5 Vulnerability curves (VCs) obtained on the basis of binarization of A^*T_2 product maps. The matrix size of the images was varied (32×32, 64×64, and 128×128, resulting in pixel sizes of 0.59×0.59, 0.30×0.30 and 0.15×0.15 mm for spruce and 0.72×0.72, 0.36×0.36 and 0.18×0.18 mm for beech), while field of view was held constant. A subset of the binarization masks that the VC's are based on is shown, together with the corresponding water potentials (WP), in (**a**) for spruce and (**b**) beech. The resulting VCs are shown in panels (**c**, **e**, **g**) for spruce; and in panels (**d**, **f**, **h**) for beech

Meixner *et al. Plant Methods*   (2021) 17:38

Page 11 of 12
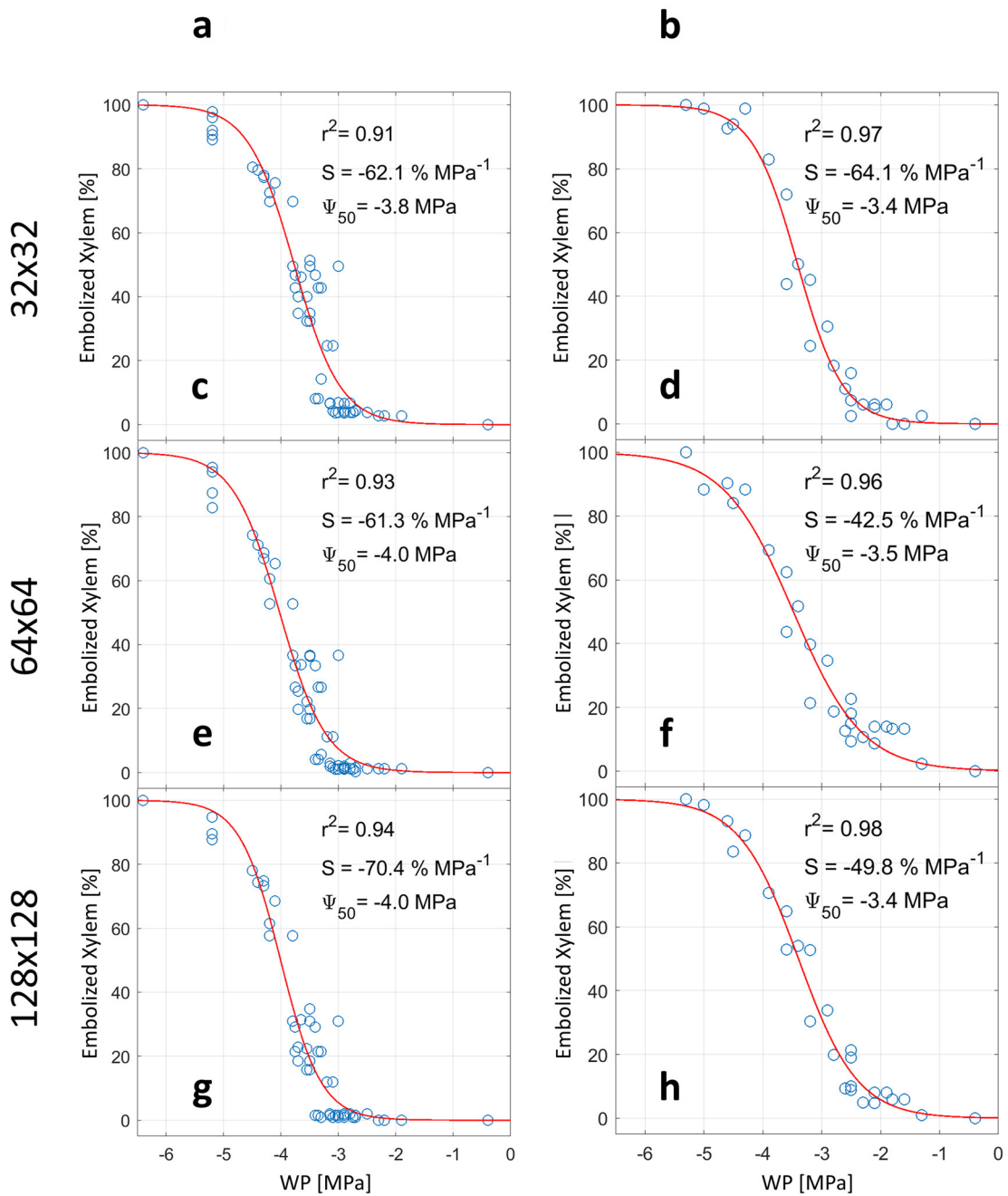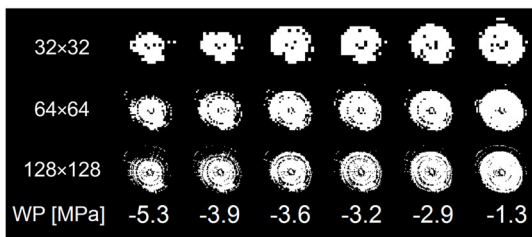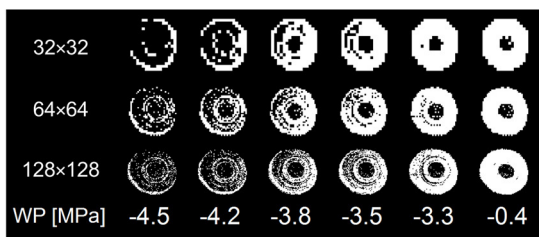
allows the strength of the main magnetic field as well as that of the imaging gradients to be reduced by a factor of four, without sacrificing SNR or increasing imaging time. Imaging at reduced spatial resolutions thus has the potential to make MR imaging of embolism formation much more mobile and affordable, further opening up the methodology to the plant hydraulics community.

Supplementary Information

The online version contains supplementary material available at https://doi.org/10.1186/s13007-021-00732-7.

Additional file 1. First echo images of well-watered spruce (a) and . beech (b), acquired with an MSE imaging sequence, illustrating the dependency of image quality and signal-to-noise ratio on matrix size and the number of acquisitions averaged (numAcq). The respective SNR is printed under each image.

Additional file 2. Water content (A) and T_2 maps of progressive xylem embolism formation in spruce (a ,b) and beech (c,d), acquired with matrix sizes of 32×32, 64×64 and 128×128 pixels, and shown in dependence of time and water potential (WP). In all panels (a-d), the difference in image intensity between the first and the last image is shown in the rightmost position ($\Delta \_$).

Additional file 3. Animated illustration of the xylem dry-down of spruce (a). Water content (A), T_2 and A^*T_2 maps were acquired at image matrix sizes of 32×32, 64×64 and 128×128 pixels. In the upper right corner dry down time and water potential are shown.

Additional file 4. Animated illustration of the xylem dry-down of beech (b). Water content (A), T_2 and A^*T_2 maps were acquired at image matrix sizes of 32×32, 64×64 and 128×128 pixels. In the upper right corner dry down time and water potential are shown.

Availability of data and materials
The datasets used and/or analysed during the current study are available from the corresponding author on reasonable request.

Declarations

Ethics approval and consent to participate
Not applicable.

Consent for publication
Not applicable.

Competing interests
The authors declare that they have no competing interests.

Author details
[1] Chair of Process Systems Engineering, Technical University Munich, Munich, Germany. [2] IBG-2: Plant Sciences, Forschungszentrum Jülich, Jülich, Germany.

References
1. Nolf M, Lopez R, Peters JMR, Flavel RJ, Koloadin LS, Young IM, Choat B. Visualization of xylem embolism by X-ray microtomography: a direct test against hydraulic measurements. New Phytol. 2017;214:890–8. https://doi.org/10.1111/nph.14462.
2. Choat B, Drayton WM, Brodersen C, Matthews MA, Shackel KA, Wada H, McElrone AJ. Measurement of vulnerability to water stress-induced cavitation in grapevine: a comparison of four techniques applied to a long-vesseled species. Plant Cell Environ. 2010;33:1502–12. https://doi.org/10.1111/j.1365-3040.2010.02160.x.
3. Knipfer T, Brodersen CR, Zedan A, Kluepfel DA, McElrone AJ. Patterns of drought-induced embolism formation and spread in living walnut saplings visualized using X-ray microtomography. Tree Physiol. 2015;35:744–55. https://doi.org/10.1093/treephys/tpv040.
4. Savi T, Miotto A, Petruzzellis F, Losso A, Pacilè S, Tromba G, et al. Drought-induced embolism in stems of sunflower: a comparison of in vivo micro-CT observations and destructive hydraulic measurements. Plant Physiol Biochem. 2017;120:24–9. https://doi.org/10.1016/j.plaphy.2017.09.017.
5. Petruzzellis F, Pagliarani C, Savi T, Losso A, Cavalletto S, Tromba G, et al. The pitfalls of in vivo imaging techniques: Evidence for cellular damage caused by synchrotron X-ray computed micro-tomography. New Phytol. 2018;220:104–10. https://doi.org/10.1111/nph.15368.
6. Dhondt S, Vanhaeren H, van Loo D, Cnudde V, Inzé D. Plant structure visualization by high-resolution X-ray computed tomography. Trends Plant Sci. 2010;15:419–22. https://doi.org/10.1016/j.tplants.2010.05.002.
7. Suuronen J-P, Peura M, Fagerstedt K, Serimaa R. Visualizing water-filled versus embolized status of xylem conduits by desktop x-ray microtomography. Plant Methods. 2013;9:11. https://doi.org/10.1186/1746-4811-9-11.
8. Nagata A, Kose K, Terada Y. Development of an outdoor MRI system for measuring flow in a living tree. J Magn Reson. 2016;265:129–38. https://doi.org/10.1016/j.jmr.2016.02.004.
9. Windt CW, Gerkema E, van As H. Most water in the tomato truss is imported through the xylem, not the phloem: A nuclear magnetic resonance flow imaging study. Plant Physiol. 2009;151:830–42. https://doi.org/10.1104/pp.109.141044.
10. van As H, Scheenen T, Vergeldt FJ. MRI of intact plants. Photosyn Res. 2009;102:213–22. https://doi.org/10.1007/s11120-009-9486-3.
11. Meixner M, Tomasella M, Foerst P, Windt CW. A small-scale MRI scanner and complementary imaging method to visualize and quantify xylem embolism formation. New Phytol. 2020. https://doi.org/10.1111/nph.16442.
12. Clearwater MJ, Clark CJ. In vivo magnetic resonance imaging of xylem vessel contents in woody lianas. Plant Cell Environ. 2003;26:1205–14. https://doi.org/10.1046/j.1365-3040.2003.01042.x.
13. Holbrook NM, Ahrens ET, Burns MJ, Zwieniecki MA. In vivo observation of cavitation and embolism repair using magnetic resonance imaging. Plant Physiol. 2001;126:27–31. https://doi.org/10.1104/pp.126.1.27.
14. Hochberg U, Albuquerque C, Rachmilevitch S, Cochard H, David-Schwartz R, Brodersen CR, et al. Grapevine petioles are more sensitive to drought induced embolism than stems: evidence from in vivo MRI and microcomputed tomography observations of hydraulic vulnerability segmentation. Plant Cell Environ. 2016;39:1886–94. https://doi.org/10.1111/pce.12688.
15. Bouda M, Windt CW, McElrone AJ, Brodersen CR. In vivo pressure gradient heterogeneity increases flow contribution of small diameter vessels in grapevine. Nat Commun. 2019;10:1–10. https://doi.org/10.17605/OSF.IO/EY2TJ.

16. Scheenen T, Heemskerk A, De Jager A, Vergeldt F, Van As H. Functional imaging of plants: a nuclear magnetic resonance study of a cucumber plant. Biophys J. 2002. https://doi.org/10.1016/S0006-3495(02)75413-1.

17. Kaufmann I, Schulze-Till T, Schneider HU, Zimmermann U, Jakob P. Functional repair of embolized vessels in maize roots after temporal drought stress, as demonstrated by magnetic resonance imaging. New Phytol. 2009;184:245–56. https://doi.org/10.1111/j.1469-8137.2009.02919.x.

18. Zwieniecki MA, Melcher PJ, Ahrens ET. Analysis of spatial and temporal dynamics of xylem refilling in Acer rubrum L. using magnetic resonance imaging. Front Plant Sci. 2013;4:265. https://doi.org/10.3389/fpls.2013.00265.

19. Fukuda K, Kawaguchi D, Aihara T, Ogasa MY, Miki NH, Haishi T, Umebayashi T. Vulnerability to cavitation differs between current-year and older xylem: non-destructive observation with a compact magnetic resonance imaging system of two deciduous diffuse-porous species. Plant Cell Environ. 2015;38:2508–18. https://doi.org/10.1111/pce.12510.

20. Umebayashi T, Morita T, Utsumi Y, Kusumoto D, Yasuda Y, Haishi T, Fukuda K. Spatial distribution of xylem embolisms in the stems of Pinus thunbergii at the threshold of fatal drought stress. Tree Physiol. 2016;36:1210–8. https://doi.org/10.1093/treephys/tpw050.

21. Meixner M, Kochs J, Foerst P, Windt CW. An integrated magnetic resonance plant imager for mobile use in greenhouse and field. J Magnet Reson. 2020. https://doi.org/10.1016/j.jmr.2020.106879.

22. Pammenter NW, van der Willigen C. A mathematical and statistical analysis of the curves illustrating vulnerability of xylem to cavitation. Tree Physiol. 1998;18:589–93. https://doi.org/10.1093/treephys/18.8-9.589.

23. Brown RW, Cheng Y-CN, Haacke EM, Thompson MR, Venkatesan R. Magnetic resonance imaging: physical principles and sequence design. Hoboken: Wiley; 2014.

24. Windt CW, Soltner H, van Dusschoten D, Blümler P. A portable Halbach magnet that can be opened and closed without force: The NMR-CUFF. J Magn Reson. 2011;208:27–33. https://doi.org/10.1016/j.jmr.2010.09.020.

25. Ma J, Slavens Z, Sun W, Bayram E, Estowski L, Hwang K-P, et al. Linear phase-error correction for improved water and fat separation in dual-echo dixon techniques. Magn Reson Med. 2008;60:1250–5. https://doi.org/10.1002/mrm.21747.

26. Edzes HT, van Dusschoten D, van As H. Quantitative T2 imaging of plant tissues by means of multi-echo MRI microscopy. Magn Reson Imaging. 1998;16:185–96. https://doi.org/10.1016/S0730-725X(97)00274-9.

27. Press WH. Numerical recipes in C++: the art of scientific computing. 2nd ed. Cambridge: Cambridge University Press; 2002.

28. Gärtner H, Schweingruber FH. Microscopic preparation techniques for plant stem analysis: Verlag Dr. Kessel; 2013.

29. Umebayashi T, Fukuda K, Haishi T, Sotooka R, Zuhair S, Otsuki K. The developmental process of xylem embolisms in pine wilt disease monitored by multipoint imaging using compact magnetic resonance imaging. Plant Physiol. 2011;156:943–51. https://doi.org/10.1104/pp.110.170282.

30. Merela M, Sepe A, Oven P, Sersa I. Three-dimensional in vivo magnetic resonance microscopy of beech (*Fagus sylvatica L.*) wood. MAGMA. 2005;18:171–4. https://doi.org/10.1007/s10334-005-0109-5.

31. Gebauer R, Plichta R, Urban J, Volařík D, Hájíčková M. The resistance and resilience of European beech seedlings to drought stress during the period of leaf development. Tree Physiol. 2020. https://doi.org/10.1093/treephys/tpaa066.

32. Pallardy SG. Physiology of woody plants. Cambridge: Academic Press; 2010.

33. Caquet B, Barigah TS, Cochard H, Montpied P, Collet C, Dreyer E, Epron D. Hydraulic properties of naturally regenerated beech saplings respond to canopy opening. Tree Physiol. 2009;29:1395–405. https://doi.org/10.1093/treephys/tpp067.

34. Aranda I, Cano FJ, Gascó A, Cochard H, Nardini A, Mancha JA, et al. Variation in photosynthetic performance and hydraulic architecture across European beech (*Fagus sylvatica L.*) populations supports the case for local adaptation to water stress. Tree Physiol. 2015;35:34–46. https://doi.org/10.1093/treephys/tpu101.

35. Lemoine D, Cochard H, Granier A. Within crown variation in hydraulic architecture in beech (*Fagus sylvatica L*): Evidence for a stomatal control of xylem embolism. Ann For Sci. 2002;59:19–27. https://doi.org/10.1051/forest:2001002.

36. Herbette S, Wortemann R, Awad H, Huc R, Cochard H, Barigah TS. Insights into xylem vulnerability to cavitation in *Fagus sylvatica L.* : Phenotypic and environmental sources of variability. Tree Physiol. 2010;30:1448–55. https://doi.org/10.1093/treephys/tpq079.

37. Schuldt B, Knutzen F, Delzon S, Jansen S, Müller-Haubold H, Burlett R, et al. How adaptable is the hydraulic system of European beech in the face of climate change-related precipitation reduction? New Phytol. 2016;210:443–58. https://doi.org/10.1111/nph.13798.

38. Stojnic S, Suchocka M, Benito-Garzón M, Torres-Ruiz JM, Cochard H, Bolte A, et al. Variation in xylem vulnerability to embolism in European beech from geographically marginal populations. Tree Physiol. 2018;38:173–85. https://doi.org/10.1093/treephys/tpx128.

39. Tomasella M, Beikircher B, Häberle K-H, Hesse B, Kallenbach C, Matyssek R, Mayr S. Acclimation of branch and leaf hydraulics in adult *Fagus sylvatica* and *Picea abies* in a forest through-fall exclusion experiment. Tree Physiol. 2018;38:198–211. https://doi.org/10.1093/treephys/tpx140.

40. Mayr S, Rothart B, Dämon B. Hydraulic efficiency and safety of leader shoots and twigs in Norway spruce growing at the alpine timberline. J Exp Bot. 2003;54:2563–8. https://doi.org/10.1093/treephys/11.1.73.

41. Chmura DJ, Guzicka M, McCulloh KA, Żytkowiak R. Limited variation found among Norway spruce half-sib families in physiological response to drought and resistance to embolism. Tree Physiol. 2016;36:252–66. https://doi.org/10.1093/treephys/tpv141.

42. Cochard H. Vulnerability of several conifers to air embolism. Tree Physiol. 1992;11:73–83. https://doi.org/10.1093/treephys/11.1.73.

Publisher's Note

2.3 Publication III: An integrated magnetic resonance plant imager for mobile use in greenhouse and field

Marco Meixner, Johannes Kochs, Petra Foerst, Carel Windt

<u>Background</u>

Magnetic resonance imagers for plants that are sufficiently mobile and robust to be easily transported and used in a greenhouse or in the field are desirable for a number of reasons. Using an imager in a greenhouse makes experiments with large numbers of plant samples more convenient, and imaging outside would allow to investigate trees and crops in their natural environment. Existing approaches are either lacking mobility, image quality or robustness. In an earlier contribution we demonstrated that in the context of monitoring xylem emboli in trees the shortcomings of a small and open permanent magnet can be compensated by using a multi-spin echo imaging pulse sequence with short echo times and many echoes (Meixner *et al.*, 2020). Short echo times and a large number of echoes, however, require a large number of short and high gradient pulses per unit time, which in turn require gradient amplifiers of sufficient strengths and speed. In this contribution we tested if these requirements can be met by adapting a gradient amplifier design of limited size to the setup presented in the earlier contribution. The robustness of the resulting magnetic resonance imaging scanner was demonstrated by imaging an apple tree in an orchard, while its long-term stability was shown in a two-month greenhouse imaging experiment on a beech tree during leaf development in spring.

<u>Results</u>

The resulting imager had a total weight of 45 kg and was small enough to fit into a car. Since all components were integrated onto an aluminum frame with wheels, the device could be moved across uneven ground by a single person and be set up within half an hour. Despite the fact that the echo number and spacing had to be chosen less demanding on the amplifier hardware than in an earlier contribution (Meixner *et al.*, 2020), high quality images with microscopic resolution were acquired during the measurements in the orchard and the greenhouse. The imager delivered images without signs of temperature drift or other artefacts when measuring outside for one hour at an ambient temperature of 7 °C, and neither when measuring continuously in a greenhouse for two months at ambient temperatures fluctuating between 18 and 28 °C.

<u>Author contributions</u>

Marco Meixner and Carel Windt designed, built and programmed the magnetic resonance imager. The mobile gradient amplifier has been designed and built by Johannes Kochs. Marco Meixner performed the experiments and analyzed the data. Marco Meixner and Carel Windt wrote the manuscript with contributions from Johannes Kochs and Petra Foerst.

An integrated magnetic resonance plant imager for mobile use in greenhouse and field

Marco Meixner [a,b], Johannes Kochs [b], Petra Foerst [a], Carel W. Windt [b,*]

[a] *Technical University Munich, SVT, Gregor-Mendel-Straße 4, 85354 Freising, Germany*
[b] *Forschungszentrum Jülich, IBG-2, Wilhelm-Johnen-Straße, Jülich, Germany*

ARTICLE INFO

ABSTRACT

In this contribution we demonstrate a mobile, integrated MR plant imager that can be handled by one single person and used in the field. Key to the construction of it was a small and lightweight gradient amplifier, specifically tailored to our combination of magnet, gradient coils and the requirements of the desired pulse sequences.

To allow imaging of branches and stems, an open C-shaped permanent magnet was used. In the design of the magnet, pole gap width, low weight and robustness were prioritized over homogeneity and field strength. To overcome the adverse effects of short T_2^*, multi-spin echo imaging was employed, using short echo times and high spectral widths. To achieve microscopic resolution under these constraints requires fast switching field gradients, driven by strong and fast gradient amplifiers. While small-scale spectrometers and RF amplifiers are readily available, appropriate small-scale gradient amplifiers or designs thereof currently are not. We thus constructed a small, 3-channel gradient amplifier on the basis of a conventional current-controlled AB amplifier design, using cheap and well-known parts. The finished device weighs 5 kg and is capable of delivering 40 A gradient pulses of >6 ms in duration.

With all components built onto an aluminum hand trolley, the imaging setup weighs 45 kg and is small enough to fit into a car. We demonstrate the mobility and utility of the device imaging quantitative water content and T_2, first of an apple tree in an orchard; second, of a beech tree during spring leaf flushing in a greenhouse. The latter experiment ran for a continuous period of 62 days, acquiring more than 6000 images.

© 2020 Forschungszentrum Jülich GmbH. Published by Elsevier Inc. This is an open access article under the CC BY-NC-ND license (http://creativecommons.org/licenses/by-nc-nd/4.0/).

1. Introduction

The development of mobile imagers and the application of mobile, field going NMR for use in plant science has long occupied the imagination of researchers [1–3], but has recently become more feasible than ever. Many components for small scale imagers have now become available, either in the form of published designs, or as ready-made commercial devices. This ranges from designs for small-scale and open (or openable) NMR magnets [4–8], via designs for small-scale, fully integrated or open source spectrometers [9–11], to examples for methods to design gradients for plane parallel magnets [12–14]. One of the most extensive studies describing the construction of a small-scale imager is that by Cooley et al. (2020) [15], who presented an affordable open source tabletop imager for teaching and testing purposes. They present

details on the construction of all components of their imager, including the software and GUI.

Despite the availability of components that would lend themselves for the construction of mobile imagers, currently no devices appear to exist that are truly mobile. Efforts to explore the utility of MR imaging of trees in the open air so far all utilized one or more conventional, full sized components [16,17]. In one case these were made transportable by mounting the setup on an electric trolley [18]. To this date, the most mobile imager that has been presented was also one of the first [2]. It was based on a commercially available small-scale TD-NMR setup, coupled with a custom-made probe head, gradient coils and gradient amplifiers. The system was used to demonstrate imaging of plants in a greenhouse. It, however, still consisted of a number of loose, interconnected components and thus did not appear suitable to be moved around.

In this work we seek to construct a truly mobile MR imager that is tailored for imaging plants at microscopic resolutions, while remaining affordable and relatively easy to build. To be called mobile, we propose that an imager a) should consist of a single,

integrated unit; b) should be light and mobile enough to be moved and handled by a single person; c) should be compact enough to fit in a regular sized car; and d) needs to be able to cope with the rigors of imaging in environments with large temperature variations and transport shocks.

In a previous study we constructed a magnet in which weight and size, as well as robustness and accessibility was prioritized over sheer magnet homogeneity [19]. The resulting C-shaped magnet has a total weight of 16 kg and can easily be re-shimmed mechanically to optimize the homogeneity of the magnetic field. It is fitted with custom-built, plane parallel gradient coils that are open from the front, yet strong and fast enough to enable the use of MSE-type sequences. The approach thus relied on a robust gradient set and a fast and powerful gradient amplifier. This requirement was easily met by a set of conventional gradient amplifiers, which, however, weighed more than 100 kg in total, making the setup large and cumbersome to move.

An integrated, truly mobile plant imager, utilizing this magnet and gradient set, would require a gradient amplifier of comparable power and speed, which at the same time would have to be small, light and robust. Unfortunately, devices of this kind have not been presented yet. Existing examples of custom-made devices are either not sufficiently mobile [16] or not sufficiently powerful [2,15]. Therefore, we here present a dedicated mobile gradient amplifier that is light and small, but at the same time sufficiently powerful to support MSE imaging at short echo times.

Using this amplifier, we constructed a practical, fully integrated mobile imager, designed specifically for imaging intact trees and plants in situ. The finished device has a total weight of 45 kg and is installed on a hand trolley. It can be moved across soft and uneven ground by a single person and allows imaging of plant organs at various heights and orientations. The mobility and functionality of the device in the field was demonstrated imaging an apple tree in an orchard. Its long-term stability was shown in a two-month greenhouse experiment, imaging the dynamics of dormancy release in the stem of a beech tree during and after spring leaf flushing.

2. Materials and methods

2.1. Mobile gradient amplifier: Design and construction

To be suitable for our purposes the gradient amplifier should allow for fast switching (<150 μs) and high current output ($\geq$40 A). These are not requirements typically associated with small-scale, mobile amplifiers. Yet, they are needed to allow for short echo times, pulsed field gradient (PFG) flow measurements of xylem and phloem sap flow in plants (future application), as well as for imaging small objects with microscopic resolution at high spectral widths. So far, we employed a stack of conventional AB power amplifiers (BAFPA40, Bruker, Rheinstetten, Germany) to achieve these requirements and drive our gradients [19]. This set of gradient amplifiers weighed approximately 105 kg, and was mounted in a 19″ rack (height of 3 × 4RU or 3 × 178 mm). In the current work we set out to replace this set of amplifiers with a unit of much lower weight (<10 kg) and bulk. This set of small-scale amplifiers should allow mobile and optionally battery driven use in the greenhouse and field, but without sacrificing current output and slew rate.

As a basis for the power stage of the mobile amplifier we chose the well-established design for a conventional AB type audio amplifier published by Giesberts (1993) [21]. This design uses cheap, well-known parts, is easy to repair, and has a low resistance power stage. To approximate the maximum current and slew rate of the full-sized amplifiers in a mobile, small-scale AB-type ampli-

fier, its efficiency needs to be much better than that of its full-sized counterpart. To achieve this goal, it is key to tailor the specifications of the amplifier to our plane parallel gradients. Due to their small size (diameter 60 mm), optimized design, thick 105 μm copper windings and low number of turns (4 in X and Y, 12 in Z) these gradients have an exceptionally low resistance (0.29 Ω in X and Y, 0.55 Ω in Z) and inductance. This allows fast slew rates even with low voltage amplifier output. Whereas the BAFPA40 reference amplifiers have a maximum output voltage of 120 V, we empirically found that 18 V already suffice to achieve a current of 40 A with a ramp time of 150 μs in the Z channel. Designing for lower output voltages markedly improves amplifier efficiency, as the average power loss (P_{loss}) at the transistors of the power stage (MOSFETS) scales with voltage:

$$P_{loss} = 1/T \int_0^T (I_{DS}(t) \cdot U_{DS}(t))dt$$

Here T represents time, I_{DS} drain-source current, and U_{DS} drain-source in-phase voltage. The maximum value of U_{DS} equals the supply voltage. By reducing the voltage of the power stages to the minimum value required by the gradient coils to achieve the desired slew rate, the heat loss per cycle in the MOSFETS was minimized. This voltage reduction also enables the use of smaller MOSFETS with a lower maximum voltage and therefore a lower internal resistance, resulting in again lower energy losses. However, there is a trade-off: the gains in efficiency come at the cost of flexibility. The amplifiers lose the ability to drive larger coils of higher impedance and will suffer a reduction in the duty cycle that can be supported.

The power stage [21] of the mobile amplifier was realized using MOSFETs IRF9540N and IRF540N in a TO-220 case (datasheet PD-91437B and PD-91341A). To increase maximum peak current and to decrease resistance we added a second pair of MOSFETs in parallel in the main branches, as simulated by Heinemann et al. [22] (Fig. 1b). No symmetrizing resistors for the current distribution were added, as would normally be used in this amplifier design. This resulted in a theoretical $R_{DS(on)}$ of 60 mΩ. The MOSFETS are cooled by means of a large aluminum cooling body and radial cooling fans (Fig. 2c, d). The cutoff frequency was 20 kHz. A standard current regulation was added as described by Cooley et al. [15], using a 50 mΩ shunt resistor as a compromise between accuracy and voltage drop.

Originally, the amplifier design mentioned above was meant to drive loads between 3 and 8 Ω. The much lower resistance of the gradient coils, in combination with parasitic inductances in the circuit, are likely to cause high peak voltages and oscillations that will damage the MOSFETS of the power stage. These oscillations were suppressed by empirically adding small capacitors between the base and collector of those transistors and in the current mirror circuit (marked *** in Fig. 1b). These additions did not increase pulse rise time.

Three gradient amplifiers were built on modular boards, designed to fit a lightweight 19″, 3RU modular euro chassis. One half of the chassis was taken up by the three gradient amplifiers, the other half of the chassis housed a set of two switched 24 V, 4 A power supplies (LS100-24, TDK-Lambda Americas Inc., Tokyo, Japan), weighing 0.6 kg each (Fig. 2). The dimensions of the power supplies ($10 \times 4 \times 25$ cm^3) are close to those of a set of heavy duty 25.9 V, 12,600 mAh lithium ion battery packs, weighing 2.0 kg each (PR-CU-R281, AA Portable power, Richmond, USA), which can easily be used to replace the power supplies, and allow for up to 8 h of continuous standalone use. Protection of gradient coils and amplifiers is ensured by fuses, as well as an analog timing circuit, limiting maximum pulse length, but allowing a shim current of

(a)

(b)
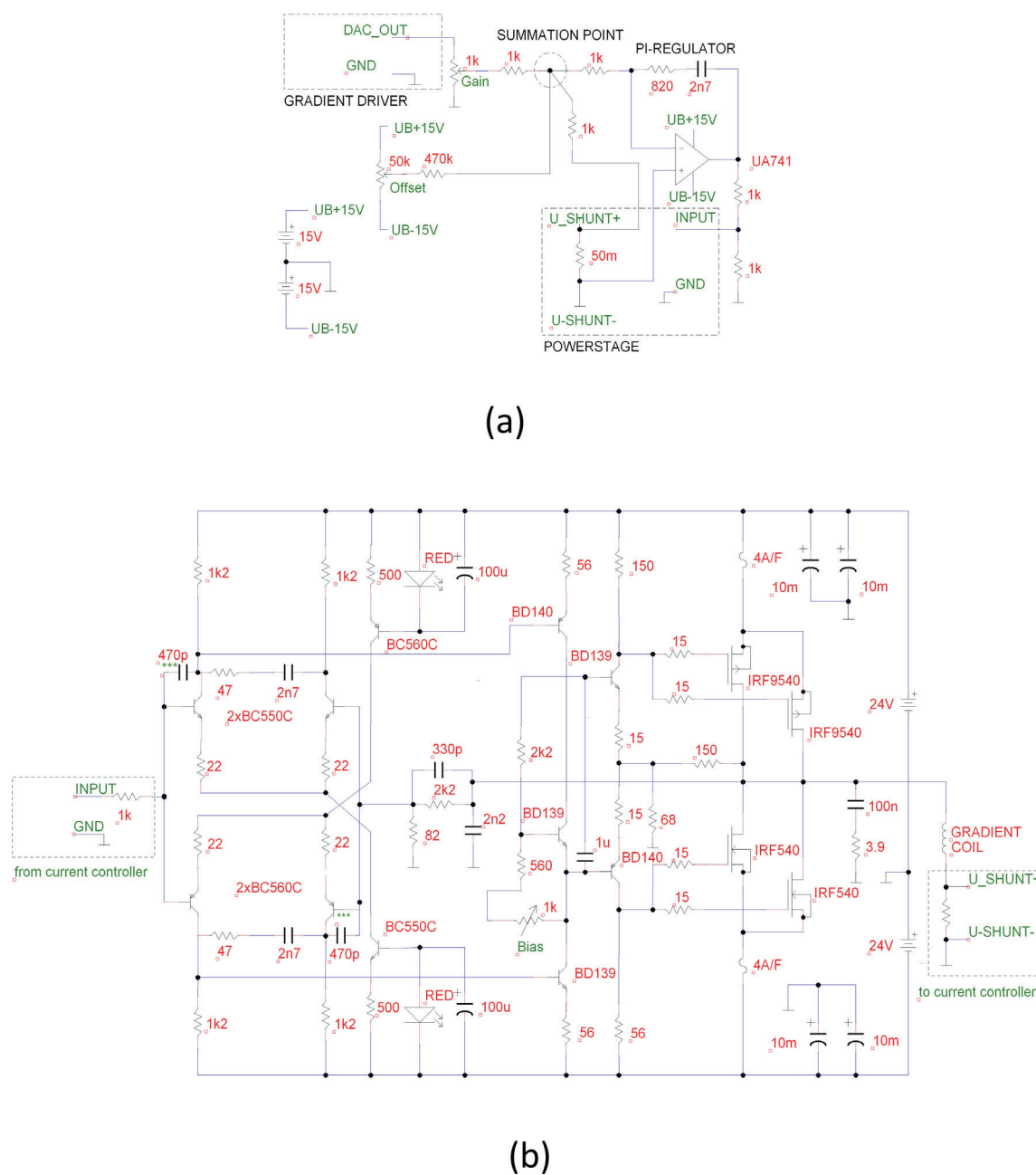
Fig. 1. Circuit diagrams of one channel of the small-scale AB gradient amplifier. The main components of the amplifiers were a pre-amplification circuit, a driver circuit, an operational amplifier based PI current regulator (shunt resistors voltage as feedback) and a power stage (MOSFET transistors 2 × IRF540, 2 × IRF9540 with a peak current >70A) (a). The power stage was based on a design published by Giesberts (1993) [21], to which capacitors were added for suppressing high peak voltages and oscillations, indicated by *** (b). To prevent voltage drop during pulsing, the supply lines of the three gradient boards were interlinked via the back plane resulting in a total capacity of 60,000 μF (not shown).

up to 2 A. Additionally, heat sink temperature is monitored for over temperature and the power stage disabled at temperatures > 70 °C.

The finished three channel amplifier weighs 5.0 kg fitted with two switched power supplies, or 7.8 kg when fitted with lithium ion battery packs. It is able to provide 40 A at a maximum voltage of 18 V per channel, for gradient pulses of up to 6 ms in duration, without significant current drop. The output current of the gradient amplifier as a function of the voltage, supplied by the gradient driver of the spectrometer, was shown to be linear (Fig. 3a). Driving the X gradient, not more than 9.5 V were required to achieve a current of 30 A with a rise time of 100 μs (Fig. 3b). In practical use, running MSE sequences at high resolution, care needed to be taken not to acquire too many echoes (<40 when measuring less than an hour, <25 during continuous imaging). At values beyond that the

transistor junction of the read channel had a tendency to overheat, and the transistors needed to be replaced. This, however, was a cheap repair of little effort. Imaging with short echo times, the modest number of echoes that can be acquired will limit the accuracy of T_2 fitting when dealing with samples with a very long T_2 (>200 ms). This may for example be encountered in the large parenchymatic cells in the pith of herbaceous plants.

2.2. Magnet and probe head

A 0.25 T, 16 kg C-shaped permanent NdFeB magnet with a 40 mm air gap was custom-built and fit with a three-axis plane parallel gradient set with a maximum gradient strength of 0.3 T/ m over a spherical volume of 25 mm in diameter in X and Y
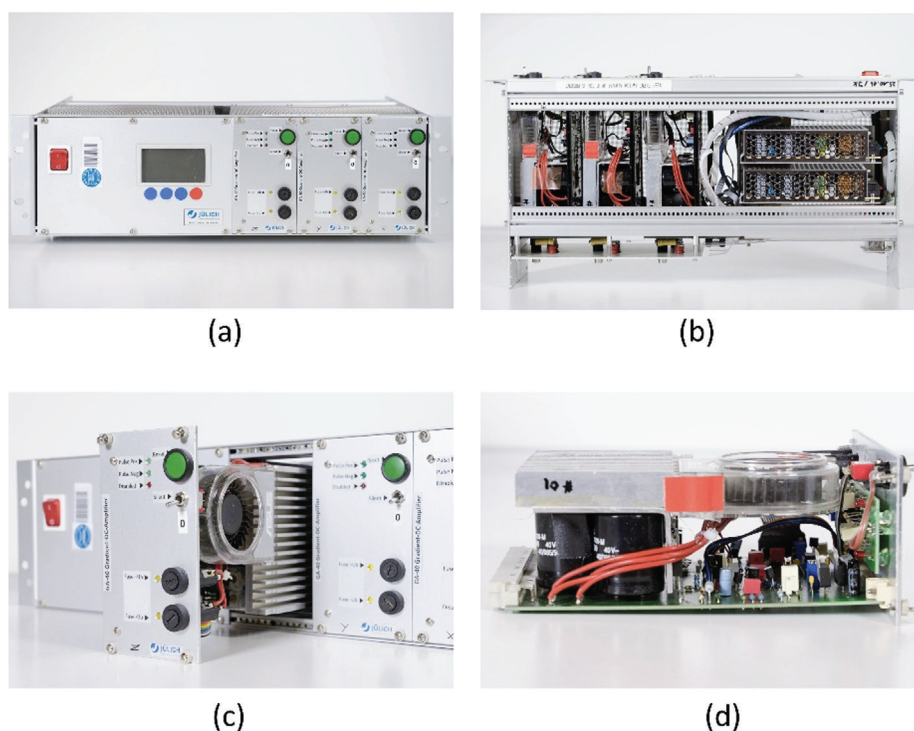
Fig. 2. Completed small-scale gradient amplifier. The front view (a) and top view with the cover removed (b) show the three amplifier modules (right in panel a), next to the power supply (left in panel a). The modular amplifier boards could be pulled out individually (c). The main transistors are fitted with an aluminum heat sink with a radial fan (d).
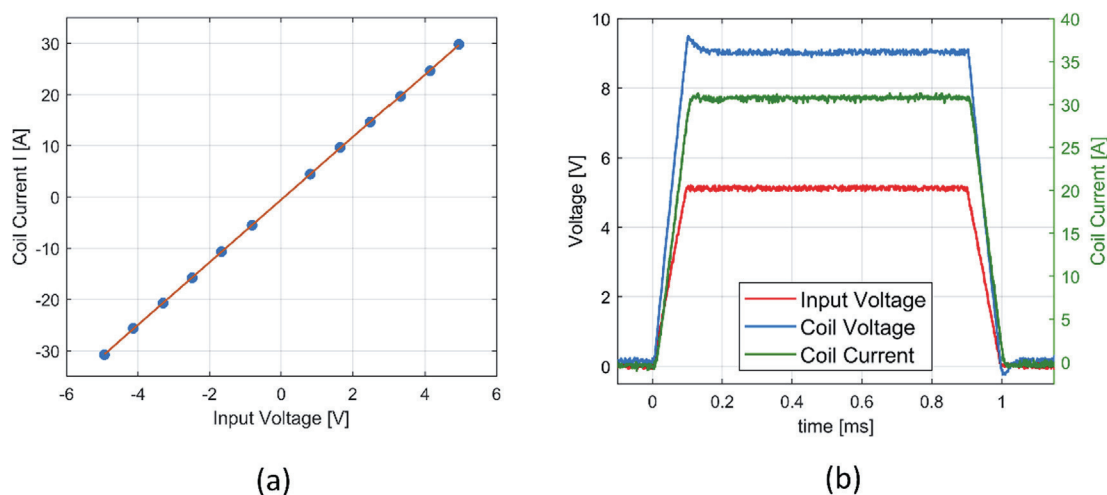

Fig. 3. Plot of the linearity of the output current of the gradient amplifier as a function of gradient driver voltage (a). Response curve of the amplifier during a 1 ms (100 μs rise time), 30 A pulse, connected to the X gradient (b). Amplifier input voltage is shown in red, coil voltage in blue and coil current in green. Current was monitored measuring the voltage drop over an additional 100 mΩ resistor mounted in series. (For interpretation of the references to color in this figure legend, the reader is referred to the web version of this article.)

direction. The diameter of the gradient coil set is 60 mm, the resistance 0.29 Ω for X and Y, and 0.55 Ω for the Z gradient. The gradient efficiency is 6.1 mT/m/A for X and Y and 22.3 mT/m/A for Z. The gradient plates were constructed on the basis of two-sided 105 μm copper circuit boards (OCTAMEX, London, United Kingdom). The gradient plates are mounted on an openable, aluminum frame that also serves as a Faraday cage (Fig. 4b). The openable probe head (RF coil, gradient coils and aluminum frame) can be rotated relative to the poles of the magnet to fit the orientation of the plant (Fig. 4c). RF coils on Teflon formers of an inner diameter of 10, 12.5, 15, 17.5 and 20 mm can be mounted in the probe head (Fig. 4d). The solenoidal coils are hand-wound onto the split

Teflon formers. To reduce magnetic field drift due to temperature changes, the poles of the magnet are equipped with resistive heating wire, coupled to an accurate temperature controller (±0.1 K regulation error) that regulated magnet temperature to a set point approximately 5 °C above ambient temperature. Further details on the magnet and probe head are given in Meixner et al. [19].

2.3. Mobile MRI hand trolley

A custom-made aluminum hand trolley with large air-filled tires was constructed as a carrier for the MR imager. A sturdy aluminum pole, that was welded to the trolley frame, supports the
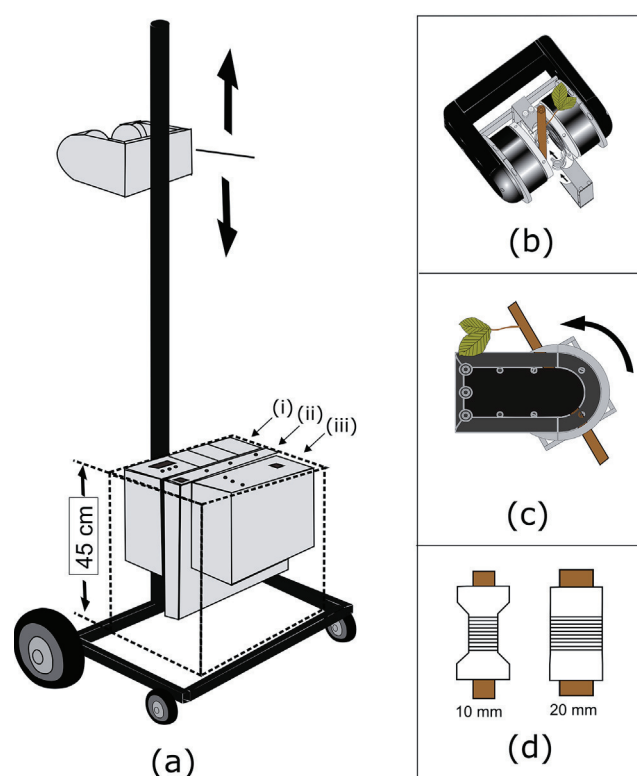
Fig. 4. Sketch of the mobile magnetic resonance imager. The setup was assembled onto a lightweight aluminum hand trolley (a). A C-shaped permanent magnet was mounted on a sturdy aluminum pole that was fixed to the hand trolley. The magnet can be moved up and down on the pole (max. height of 160 cm). The electronic components comprise a custom-built, small-scale, 3-axis gradient amplifier (i), a pre-emphasis unit (ii), and a Kea II spectrometer with built-in RF amplifier (iii). The probe head and RF coil can be opened, allowing plant stems or branches to be inserted (b). The angle of the probe head can be adjusted relative to the magnet to match the angle of the object of interest (c). The diameter of the split Teflon former of the RF coil can be chosen to closely match the diameter of the plant shoot (10–20 mm) (d).

magnet; the magnet is fixed relative to the pole with two quick release clamps. The pole provides a convenient handle to recline the trolley onto its large rear tires and move the trolley around. After parking, the magnet can be slid up the pole for easy mounting at heights between 50 and 160 cm. During the orchard measurement the magnet was covered with a thin sheet of flexible insulation foam, shielding it from the low ambient temperature (7 °C). Included in the imaging setup are the 3-axis gradient amplifier, a Kea II spectrometer (Magritek, Wellington, New Zealand) with a standard built-in 100 W RF amplifier, and a pre-emphasis unit (Resonance Research, Billerica, USA). The imaging console is operated with a standard laptop, running the proprietary spectrometer software Prospa V3.21 (Magritek, Wellington, New Zealand). The electronic components of the imager are mounted side by side in a 19″ rack at the bottom of the trolley, lowering the center of gravity and countering the weight of the magnet on the pole (Fig. 4a). The entire imager (trolley, magnet and electronic components) weighs 45 kg.

2.4. Plant material, treatment and handling

Two demonstrator experiments are presented in this contribution. The first one was conducted on a full-grown commercial apple tree (Malus domestica cv. Captan), grown in the open air in an orchard at the Research Campus Klein-Altendorf, Rheinbach,

Germany. Here, the magnet was mounted on a branch with a diameter of 10 mm at a height of about 1.5 m (Fig. 5).

The second demonstrator measurement was a long-term experiment during which the dormancy release (spring awakening) of a 150 cm tall beech tree (*Fagus sylvatica*) was monitored. The tree was purchased in mid-winter from a local nursery (Baumschule Leonhard Veith, Merzenich-Golzheim, Germany). Prior to the experiment the plant was grown in the open air, at temperatures between −7 and 5 °C. At the end of winter dormancy release was forced by moving the tree into the greenhouse, exposing it to long day length and higher temperatures (20 °C, 16 h day; 16 °C, 8 h night; 250 μmol m^2 s^{-1} PAR in supplemental lighting by metal halogen vapor lamps (250 W SON-Agro, Philips, Eindhoven, the Netherlands)). At the measurement position, 135 cm above the soil, the stem had a diameter of 18 mm. Imaging was started directly after moving the plant to the greenhouse. For this long-term measurement any movement of the plant relative to the imager was avoided by minimizing tension in the branch due to its fixation, as the gradual release of such tensions by tree growth was found to cause movement and potential ghosting artefacts in prior experiments.

2.5. MR Imaging, parameters and processing

The following steps were performed prior to image acquisition: (i) Adjustment the height of the magnet and the angle of the probe head to match that of the branch; (ii) winding the coil around the shoot; (iii) sliding the branch with the coil into the probe head; closing of the probe head and covering it with an earthed silver-plated copper mesh, (iv) tuning and matching of the coil, finding pulse settings and (v) optimizing the angle of the probe head so that it is perfectly perpendicular to the branch. The latter was done by imaging side projections of the shoot. Small adjustments of the position and angle of the branch were done by means of aluminum clamps, fastened onto the MRI hand trolley above and below the position of the magnet. All image acquisition was done with an MSE imaging pulse sequence as described by Edzes et al. [20], employing an XY-8 phase cycling scheme [19,23].

For the orchard experiment a 15 mm diameter solenoidal coil was employed. Images at two matrix sizes were acquired, 128×128 and 64×64, both with a field of view (FOV) of 16.7×16.7 mm, a slice thickness of 4 mm and the following settings: Slice selective 90° pulse: 500 μs soft five lobe sinc, −38 dB; hard 180° pulses: 7.8 μs, −16 dB; 40 echoes; echo time (TE) 4 ms, spectral width (SW) 100 kHz. Images with a matrix size of 64×64 were acquired with a repetition time (TR) of 2.5 s and 4 averages, resulting in a total image acquisition time of 5 min. The 128×128 images were acquired with a TR of 1.5 s and 16 averages, resulting in an image acquisition time of 50 min. The ambient temperature during the measurement was around 7 °C; the magnet set point temperature was 12 °C.

For the long-term dormancy release experiment a 20 mm diameter solenoidal coil was employed. In the greenhouse the tree was imaged continuously for 62 days until its leaves had fully emerged and the first leaves reached maturity. Imaging was done every 15 min, with the following settings: matrix size 128×128, FOV 24×24 mm, slice thickness 5 mm, 4 averages, TR 1.5 s, TE 5 ms, 24 echoes, 90° pulse: −36.5 dB, 500 μs five lobe sinc; hard 180° pulses: −16 dB, 9.9 μs; SW of 100 kHz. Despite the active temperature control of the magnet, strong temperature changes in the greenhouse or direct solar irradiation caused small changes in B$_0$. To compensate, resonance frequency was automatically determined between measurements and B$_1$ frequency adjusted to match.

Passive and active shimming of the magnet was done once, directly after mounting the tree into the imager. Subsequently
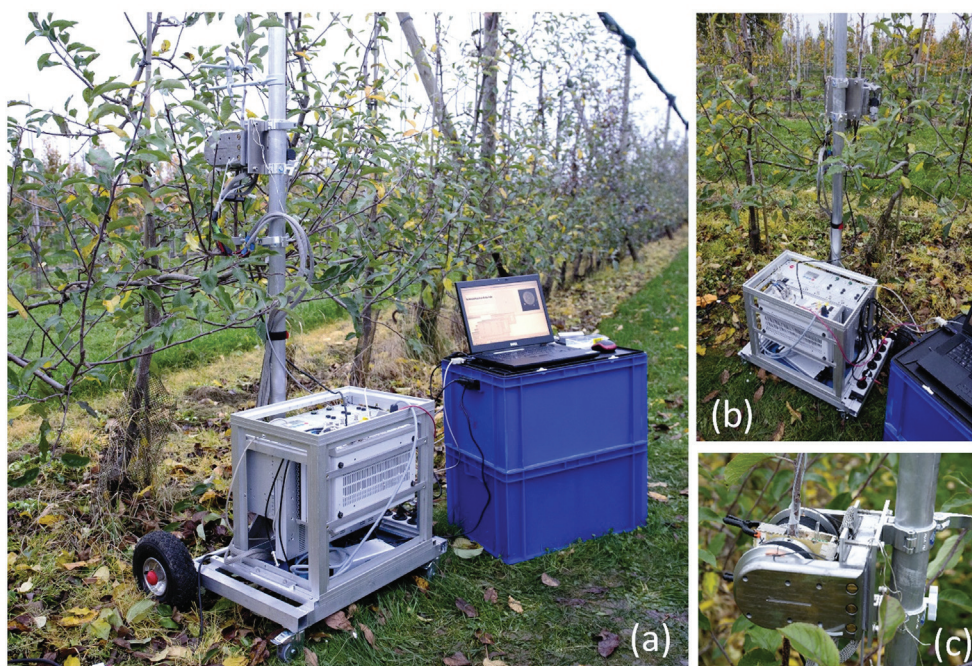
Fig. 5. The mobile MRI scanner in an orchard (Research Campus Klein-Altendorf, Rheinbach, Germany) (a). The imaging hardware was installed onto a 19″ frame, mounted on an aluminum hand trolley. The C-shaped permanent magnet was supported by an aluminum pole, which was an integral part of the hand trolley (c). By sliding up or down the magnet was adjusted in height. Empty plastic crates (blue) provided a makeshift table for the laptop. (For interpretation of the references to color in this figure legend, the reader is referred to the web version of this article.)

active shimming was done and checked every two weeks, but no significant adjustments were needed during the entire 62 day period.

All image acquisition and data processing was programmed in Prospa (Magritek, Wellington, New Zealand). First, all images were masked and phase corrected according to Ma (2008) [24]. Quantitative water content (A) and T_2-maps were calculated on the basis of a mono-exponential fit of the signal for every pixel. In the dormancy release experiment, all water content maps were normalized on the basis of the reference tube. A^*T_2 product maps were obtained by performing a pixel-by-pixel multiplication of the amplitude- and T_2-maps [19]. A^*T_2 product maps were shown to be especially helpful to visualize filled xylem vessels in trees. Xylem vessels tend to be smaller than can be spatially resolved, but give rise to pixels with elevated water content (A) and T_2. By multiplying the two parameter maps, the contrast between wood with and without filled xylem vessels is greatly enhanced, enabling the detection of pixels with filled xylem vessels even less than half the cross sectional area of those pixels is occupied by xylem sap [19]. In the greenhouse experiment, before T_2-fitting, all images were calculated based on sliding window averaging of 36 MSE measurements. To filter out noise in the animations of sequential images, pixels with values that were double or more, or half or less, than all four nearest neighboring pixels were assumed to be noise and set to zero (supplementary Fig. S1 and S2).

## 3. Results and discussion

3.1. Orchard field-measurement

The mobility and robust nature of the mobile MRI scanner were demonstrated by imaging the branch of an apple tree (Malus domestica cv. Captan) in a research orchard (Fig. 5). The experiment was done in early November on a day with a maximum tem-

perature of 7 °C. The device was loaded into the trunk of a car and taken to the measurement site. Thanks to the large air-filled tires the device could be wheeled with ease from the car to the tree of choice by a single person, unhindered by the soft and uneven field. After adjusting the set point of the temperature controller of the magnet to approximately 12 °C, magnet temperature equilibrated within about two hours. Prior to taking the setup out of the lab, the magnet was at a set point temperature of approximately 25 °C. In the car magnet temperature was not controlled and ambient temperature was approximately 20 °C. The robust and basic construction of the magnet allowed re-shimming it in minutes at the site of measurement, correcting for the potential effects of transport shocks and temperature changes. Passive shimming was done by adjusting the pole shoe alignment of the magnet; active shimming was done by means of the three gradient coils.

Images of the branch were obtained at two matrix sizes (64×64 and 128×128), both with the same FOV (16.7×16.7 mm). At a matrix size of 64×64 a full dataset could be acquired within 5 min, from which water content and T_2 images with a pixel size of 0.26×0.26 mm were obtained. At a matrix size of 128×128 (pixel size 0.13×0.13 mm) image acquisition took 50 min. During this time, no artefacts (such as blurring or image deformation) were observed, indicating that the magnet temperature was held sufficiently constant to prevent temperature induced shifts of B_0 (Fig. 6).

Images readily allowed to differentiate stem tissues, such as bark (water content 30%, T_2 40 ms), cambium (water content 50%, T_2 80 ms), xylem (water content 30 to 40%, T_2 70 to 100 ms) and pith (water content 55%, T_2 145 ms). The uniform water content (A) and T_2 values of the xylem reflected the homogeneous vessel distribution in the wood, as observed by light microscopy after harvesting (not shown). In amplitude (64×64: 0.107, 128×128: 0.115) and T_2 (64×64: 81.2 ms, 128×128: 74.9 ms) the average values of images acquired with both matrix sizes agreed within an error range <10% (Fig. 6).
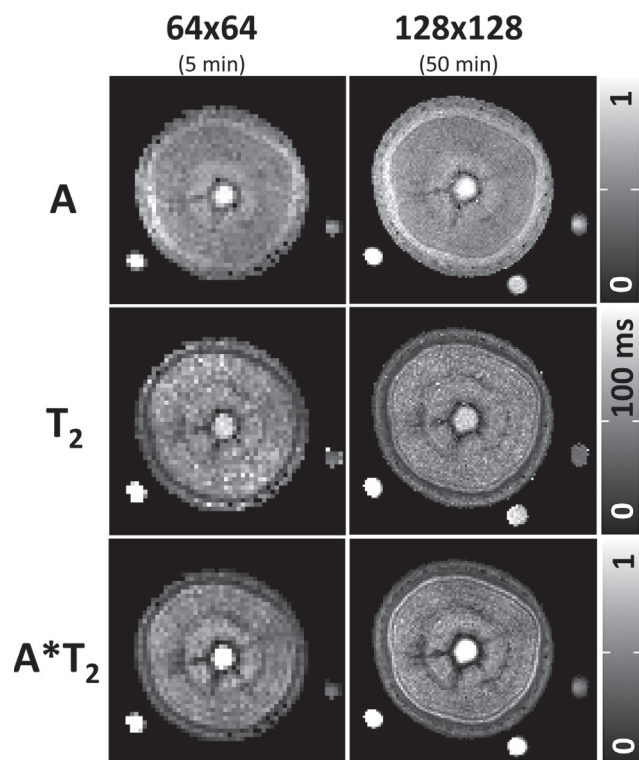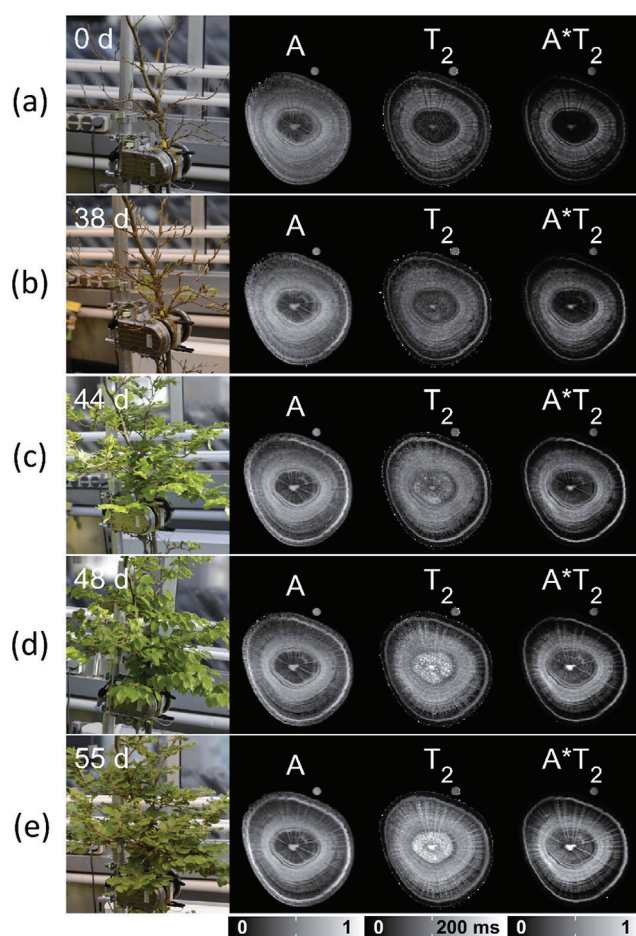
Fig. 6. Amplitude (A), T_2, $A*T_2$ images of an apple branch, acquired with the mobile imager in an orchard. Field of view 16.7×16.7 mm. At a matrix size of 64×64 (left column) image acquisition took 5 min, at a matrix size of 128×128 (right column) 50 min.

Fig. 7. Long-term greenhouse experiment, monitoring the stem of a beech tree (*Fagus sylvatica*) during bud flushing, leaf development and leaf maturation. The tree was imaged continuously for a period of 62 days; shown are images acquired between day 0 (a) – day 55 (e). Every MRI parameter map represents the sliding window average of 36 measurements, acquired over a period of 9 h. A photo of the branches of the tree is shown next to the corresponding amplitude (A), relaxation time (T_2) and $A*T_2$ product images. An animation of the whole 62 day experiment is provided as supplementary material (S1).

3.2. Long-term greenhouse measurement

As a demonstrator experiment for the long term use of the imager in an agronomical setting with strongly varying environmental conditions, the MRI scanner was set up in a greenhouse to monitor an 18 mm diameter beech stem (*Fagus sylvatica*) during bud burst and leaf flushing, for a continuous period of 62 days (Fig. 7). In the greenhouse the imager experienced diurnal temperature changes between 18 and 28 °C and was occasionally exposed to direct sunlight and high air humidity. During the experimental period B_0 showed a variation of 9.8 kHz at the very extremes, but usually did not show a diurnal drift of more than 3.9 kHz (Fig. S3), i.e. half a pixel at a matrix size of 128 at a spectral width of 100 kHz. This was easily corrected by determining and adjusting resonance frequency between measurements. The imager remained functional for the whole time, acquiring >6000 images sequentially, demonstrating the reliability and durability of the setup in the challenging greenhouse environment.

The water content and T_2 values of the various tissues in the stem (bark, cambium and phloem, xylem, pith; Fig. 7) were in line with previous experiments imaging beech [19,25]. In the xylem, one large and mostly connected ring of tissue had the highest water contents (33 to 40%) and T_2 values (50 to 90 ms). Over a period of 62 days, water content in this ring increased from around 35% to values of up to 57%; while T_2 increased from around 70 ms to a maximum value of 127 ms. In the oldest xylem in the center, T_2 increased from 30 ms to more than 100 ms, while water content values in this area increased from 15 to 20% (Fig. 7).

The average water content and T_2 values of the stem were found to oscillate diurnally during the whole experiment (Fig. 8a). Both parameters exhibited fluctuations of around 3 to 4%, with a maximum in the morning and a minimum in the evening. Both quantities thus reflect the diurnal pattern of the depletion of stem water

reserves during the day and their replenishment during the night [1,7,8,26,27]. The diurnal pattern of fluctuation closely matched that which is observed when measuring stem diameter variations by means of dendrometers [5,28]. In vivo MRI of oak revealed that most of the diurnal shrinkage and swelling in that species is caused by water content fluctuations in the elastic bark tissues [27]. The water content fluctuations that we observed in the bark after leaf emergence (supplementary animations S2c and S2d) mirror this behavior and suggest that the same holds true in beech.

Bud development during the first 36 days, prior to leaf emergence, coincided with a moderate increase in stem water content (~10%; Fig. 8b-c). This increase was observed mainly in the bright xylem ring. Between day 0 and 20 the average T_2 value of the stem increased from 47 to 63 ms. This became visible throughout the xylem, but was especially noticeable in the older year rings (Fig. 8b). Between days 20 to 37 the stem average T_2 value went back down to 53 ms, with T_2 decreasing again throughout the xylem (Fig. 8a, c). Between day 37 and 47 the first leaves emerged, while a significant T_2 increase in the older xylem and the pith was observed (Fig. 8d). The rays stood out in T_2 and $A*T_2$ images, while a more moderate T_2 increase was observed in the younger xylem. Between day 47 and day 61 water content increased significantly in the cambium and in the younger xylem, resulting in an average
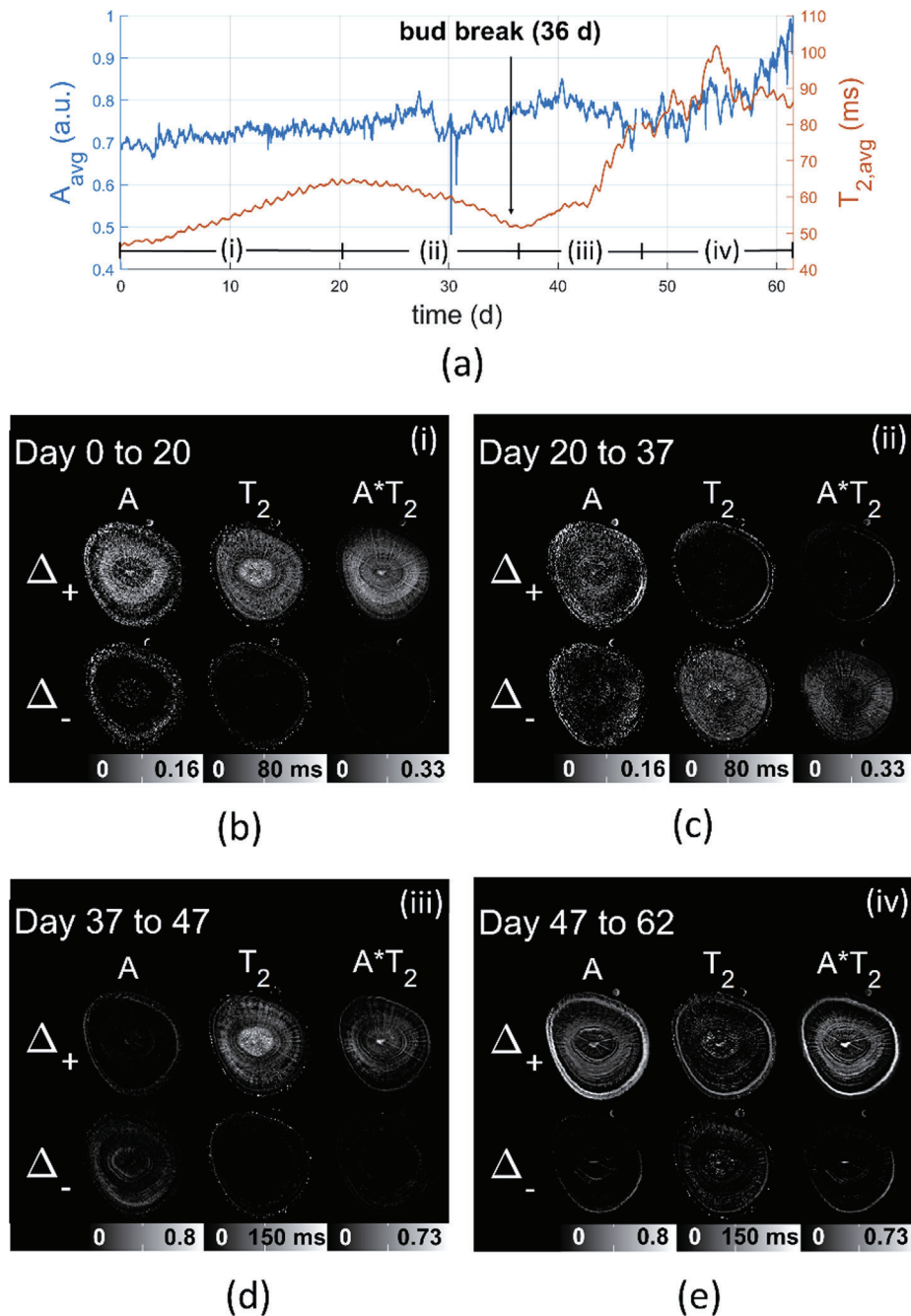
Fig. 8. Average amplitude (A), T_2, and $A*T_2$ in the stem of beech during bud flushing and leaf maturation over a period of 62 days (a). The most significant positive and negative changes during periods (i) to (iv) in the A, T_2 and $A*T_2$ parameter maps are shown in panels b-e. Positive changes in the respective time periods are shown in the top half of the panels (Δ_+), negative changes in the bottom half (Δ_-). The scaling of the water content and $A*T_2$ product images is relative to the scaling used in Fig. 6. Animations representing the timeframes of panel b) - e) are provided as supplementary material (S2a-d).

water content increase of 36% (Fig. 8a, e). This was accompanied by a moderate change in T_2 in the cambium.

The observed T_2 of water in compartments in porous structures such as plant tissues is negatively correlated with compartment size if, after excitation, magnetization bearing protons are likely to reach the compartment wall by diffusion in a timescale shorter than the intrinsic (or bulk) T_2 of the liquid [29]. This correlation has been observed for living vacuolated plant tissues [30,31], as well as for woody xylem conduits [32,33]. In the context of drought stress in trees, we utilized this effect to monitor embolism formation (i.e, the collapse of water columns) in xylem conduits [19]. In the context of flushing, an increase in T_2 as observed in Fig. 8b and d may

reflect the swelling of compartments, or water entering larger, previously empty lumina. Other factors that are associated with flushing and that might influence T_2, such as an increased sugar concentration in the xylem sap, or an increased membrane permeability, are unlikely to have caused the T_2 increase. They would both rather have caused the opposite effect, a decrease in the observed T_2 [34,35].

In temperate angiosperms including beech [36], a substantial part of the conductive xylem tissue is embolized due to freeze-thaw cycles during winter [37,38]. In beech, active refilling is the dominant mechanism to reestablish xylem function [39], allowing for flow resumption during leaf development [40]. Refilling is

thought to involve the wood rays, consisting of radially aligned files of specialized parenchyma cells. They form a link between xylem and phloem, and allow radial bi-directional transport of water and solutes. Rays were found to be involved in the storage and remobilization of starch, sugars, protein and fats [41,42]. Sucrose and other soluble sugars are essential for the development of new leaves in spring. They were found to arise from starch mobilization, after which they are radially translocated from the rays to the phloem, or the conduit lumen [43,44]. Tantalizingly, indirect evidence for both processes would appear to become visible in the increases in amplitude and T_2 of the rays (Fig. 8a, 8d, supplemental animation S2a, S2c, S2d) and in T_2 for the potential mobilization of starch in the center of the tree (Fig. 8d, supplemental animation S2c, from day 45 onwards).

Copini et al. [45] used MRI to monitor dormancy release in oak by imaging and subsequently harvesting two individuals per phenophase from April till June. Even though oak has a ring porous wood architecture that is different from semi-diffuse porous beech, similarities in the pattern of spring refilling were found. For both species, before bud break water in the stem was distributed fairly diffusely and homogeneously (Fig. 7a). Upon dormancy release average stem water content increased only moderately, but marked increases in water content were observed in the newly formed xylem (Fig. 8e). In both species water in the older year rings appeared to converge in particular regions, increasing contrast between wood regions with and without water. Copini et al. found the development of new vessels to coincide with leaf formation. In beech we also observed the start of xylem formation to coincide with bud break.

The T_2 dynamics between day 37 and 47 are particularly interesting (Fig. 8d). Bud break was accompanied by the start of a strong increase in the T_2 of the oldest xylem and the pith in the middle of the plant. Due to its low water content ($\sim$15%) this region would not appear to contain conducting xylem. The strong increase in T_2 in the center was accompanied by a more moderate T_2 increase in the surrounding xylem tissue, with especially the wood rays standing out (Fig. 8d). These increases in T_2 were followed between day 47 and 61 by a marked increase in water content in the cambium and the younger xylem, indicating radial growth (Fig. 8e, see supplementary animations S2c,d for details). This suggests that older xylem may have been used for storing starch. The increase in T_2 then may be associated with the mobilization (hydrolyzation) of starch into of soluble sugars around bud break. Such soluble sugars are osmotically active, attracting water and potentially causing a local increase in turgor. The sugars are subsequently transported via the rays to the xylem vessels, supporting xylem refilling and flow resumption, as well as to the cambium to support growth [46]. In spring, when sugars are mobilized, wood ray cells are likely to attract water and swell. The resulting decrease in surface-to-volume ratio may have caused the observed increase in the T_2 of the wood rays.

4. Conclusion

We presented a fully integrated, mobile plant imager with a maximum field of view of 20 mm.

To be able to run an MSE pulse sequence with short echo times and high spectral width, while achieving microscopic resolution, we constructed a small-scale gradient amplifier that was capable of generating pulses of up to 40 A at a duration of up to 6 ms.

By mounting all components of the MRI scanner (magnet, spectrometer, pre-emphasis unit, gradient amplifier) on a hand trolley, a mobile imager was obtained that could be moved by one person, transported in a regular car and used in the field. It was capable of delivering water content and T_2 images of high quality, while operating under challenging environmental conditions and over extended periods of time.

All components that were custom built for the imager (i.e., the magnet, gradient coils and gradient amplifier) were of well-known design and could potentially be manufactured at low to moderate cost, especially if produced in larger numbers. The spectrometer was the most expensive element in the imager. In the future, by also replacing the spectrometer with an affordable open source design, the imaging setup could become more affordable still. This, as well as the fact that the machine could easily be shared between labs, could make MRI available more widely for applications in plant physiology. Cheaper measurement time would also allow imaging of plants over extended periods of time.

Declaration of Competing Interest

Acknowledgements

Appendix A. Supplementary data

Supplementary data to this article can be found online at https://doi.org/10.1016/j.jmr.2020.106879.

References

[1] H. Van As, J.E.A. Reinders, P.A. de Jager, P. van de Sanden, T.J. Schaafsma, In situ plant water balance studies using a portable NMR spectrometer, J. Exp. Bot. 45 (1994) 61–67, https://doi.org/10.1093/jxb/45.1.61.

[2] M. Rokitta, E. Rommel, U. Zimmermann, A. Haase, Portable nuclear magnetic resonance imaging system, Rev. Sci. Instrum. 71 (2000) 4257, https://doi.org/10.1063/1.1318922.

[3] B. Goodson, Mobilizing magnetic resonance, Phys. World 19 (2006) 28.

[4] T. Umebayashi, K. Fukuda, T. Haishi, R. Sotooka, S. Zuhair, K. Otsuki, The developmental process of xylem embolisms in pine wilt disease monitored by multipoint imaging using compact magnetic resonance imaging, Plant Physiol. 156 (2011) 943–951, https://doi.org/10.1104/pp.110.170282.

[5] C.W. Windt, P. Blümler, A portable NMR sensor to measure dynamic changes in the amount of water in living stems or fruit and its potential to measure sap flow, Tree Physiol. 35 (2015) 366–375, https://doi.org/10.1093/treephys/tpu105.

[6] K. Fukuda, D. Kawaguchi, T. Aihara, M.Y. Ogasa, N.H. Miki, T. Haishi, T. Umebayashi, Vulnerability to cavitation differs between current-year and older xylem: non-destructive observation with a compact magnetic resonance imaging system of two deciduous diffuse-porous species, Plant Cell Environ. 38 (2015) 2508–2518, https://doi.org/10.1111/pce.12510.

[7] C.W. Windt, H. Soltner, D. van Dusschoten, P. Blümler, A portable Halbach magnet that can be opened and closed without force: the NMR-CUFF, J. Magn. Reson. 208 (2011) 27–33, https://doi.org/10.1016/j.jmr.2010.09.020.

[8] S. Lechthaler, E.M.R. Robert, N. Tonné, A. Prusova, E. Gerkema, H. van As, N. Koedam, C.W. Windt, Rhizophoraceae mangrove saplings use hypocotyl and leaf water storage capacity to cope with soil water salinity changes, Front. Plant Sci. 7 (2016) 895, https://doi.org/10.3389/fpls.2016.00895.

[9] K. Takeda, OPENCORE NMR: open-source core modules for implementing an integrated FPGA-based NMR spectrometer, J. Magn. Reson. 192 (2008) 218–229, https://doi.org/10.1016/j.jmr.2008.02.019.

[10] C.A. Michal, A low-cost multi-channel software-defined radio-based NMR spectrometer and ultra-affordable digital pulse programmer, Concepts

Magnetic Reson. Part B: Magnetic Reson. Eng. 48 (2018) e21401, https://doi.org/10.1002/cmr.b.21401.

[11] J.B.W. Webber, P. Demin, Credit-card sized field and benchtop NMR relaxometers using field programmable gate arrays, Magn. Reson. Imaging 56 (2019) 45–51, https://doi.org/10.1016/j.mri.2018.09.018.

[12] W. Liu, D. Zu, X. Tang, H. Guo, Target-field method for MRI biplanar gradient coil design, J. Phys. D Appl. Phys. 40 (2007) 4418.

[13] M. Zhu, L. Xia, F. Liu, S. Crozier, Deformation-space method for the design of biplanar transverse gradient coils in open MRI systems, IEEE Trans. Magn. 44 (2008) 2035–2041, https://doi.org/10.1109/TMAG.2008.923898.

[14] Y. Wang, Q. Wang, L. Guo, Z. Chen, C. Niu, F. Liu, An actively shielded gradient coil design for use in planar MRI systems with limited space, Rev. Sci. Instrum. 89 (2018) 95110.

[15] C.Z. Cooley, J.P. Stockmann, T. Witzel, C. LaPierre, A. Mareyam, F. Jia, M. Zaitsev, Y. Wenhui, W. Zheng, P. Stang, Design and implementation of a low-cost, tabletop MRI scanner for education and research prototyping, J. Magnetic Resonance 310 (2020) 106625, https://doi.org/10.1016/j.jmr.2019.106625.

[16] M. Jones, P.S. Aptaker, J. Cox, B.A. Gardiner, P.J. McDonald, A transportable magnetic resonance imaging system for in situ measurements of living trees: The Tree Hugger, J. Magn. Reson. 218 (2012) 133–140, https://doi.org/10.1016/j.jmr.2012.02.019.

[17] A. Nagata, K. Kose, Y. Terada, Development of an outdoor MRI system for measuring flow in a living tree, J. Magn. Reson. 265 (2016) 129–138, https://doi.org/10.1016/j.jmr.2016.02.004.

[18] T. Kimura, Y. Geya, Y. Terada, K. Kose, T. Haishi, H. Gemma, Y. Sekozawa, Development of a mobile magnetic resonance imaging system for outdoor tree measurements, Rev. Sci. Instrum. 82 (2011) 53704, https://doi.org/10.1063/1.3589854.

[19] M. Meixner, M. Tomasella, P. Foerst, C.W. Windt, A small-scale MRI scanner and complementary imaging method to visualize and quantify xylem embolism formation, New Phytol. 33 (2020) 1502, https://doi.org/10.1111/nph.16442.

[20] H.T. Edzes, D. van Dusschoten, H. van As, Quantitative T2 imaging of plant tissues by means of multi-echo MRI microscopy, Magn. Reson. Imaging 16 (1998) 185–196, https://doi.org/10.1016/S0730-725X(97)00274-9.

[21] T. Giesberts, HEXFET-medium-power-amp: symmetrische FET-endstufe, ELEKTOR Magazine 12 (1993).

[22] R. Heinemann, Braunschweig, Germany, PSpice-Simulation eines 120 W Leistungsverstärkers mit komplementären MOSFets IRF150 und IRF9140, 2012. http://www.spicelab.de/mosfet_endstufe.htm (accessed 18 July 2019).

[23] C.W. Windt, F.J. Vergeldt, H. van As, Correlated displacement-T2 MRI by means of a pulsed field gradient-multi spin echo method, J. Magn. Reson. 185 (2007) 230–239, https://doi.org/10.1016/j.jmr.2006.12.015.

[24] J. Ma, Z. Slavens, W. Sun, E. Bayram, L. Estowski, K.-P. Hwang, J. Akao, A.T. Vu, Linear phase-error correction for improved water and fat separation in dual-echo dixon techniques, Magn. Reson. Med. 60 (2008) 1250–1255, https://doi.org/10.1002/mrm.21747.

[25] M. Merela, A. Sepe, P. Oven, I. Sersa, Three-dimensional in vivo magnetic resonance microscopy of beech (Fagus sylvatica L.) wood, MAGMA 18 (2005) 171–174, https://doi.org/10.1007/s10334-005-0109-5.

[26] K. Steppe, R. Lemeur, An experimental system for analysis of the dynamic sap-flow characteristics in young trees: Results of a beech tree, Functional Plant Biol. 31 (2004) 83–92, https://doi.org/10.1071/FP03150.

[27] V. de Schepper, D. van Dusschoten, P. Copini, S. Jahnke, K. Steppe, MRI links stem water content to stem diameter variations in transpiring trees, J. Exp. Bot. 63 (2012) 2645–2653, https://doi.org/10.1093/jxb/err445.

[28] P. Köcher, V. Horna, C. Leuschner, Stem water storage in five coexisting temperate broad-leaved tree species: significance, temporal dynamics and dependence on tree functional traits, Tree Physiol. 33 (2013) 817–832, https://doi.org/10.1093/treephys/tpt055.

[29] H. van As, Intact plant MRI for the study of cell water relations, membrane permeability, cell-to-cell and long distance water transport, J. Exp. Bot. 58 (2007) 743–756, https://doi.org/10.1093/jxb/erl157.

[30] L. van der Weerd, M.M.A.E. Claessens, T. Ruttink, F.J. Vergeldt, T.J. Schaafsma, H. van As, Quantitative NMR microscopy of osmotic stress responses in maize and pearl millet, J. Exp. Bot. 52 (2001) 2333–2343, https://doi.org/10.1093/jexbot/52.365.2333.

[31] L. van der Weerd, S.M. Melnikov, F.J. Vergeldt, E.G. Novikov, H. van As, Modelling of self-diffusion and relaxation time NMR in multicompartment systems with cylindrical geometry, J. Magn. Reson. 156 (2002) 213–221, https://doi.org/10.1006/jmre.2002.2550.

[32] N.M. Homan, C.W. Windt, F.J. Vergeldt, E. Gerkema, H. Van As, 0.7 and 3 T MRI and sap flow in intact trees: xylem and phloem in action, Appl. Magn. Reson. 32 (2007) 157–170, https://doi.org/10.1007/s00723-007-0014-3.

[33] Araujo, MacKay, Hailey, Whittall, Le, Proton magnetic resonance techniques for characterization of water in wood: application to white spruce, 1992.

[34] B.P. Hills, S.L. Duce, The influence of chemical and diffusive exchange on water proton transverse relaxation in plant tissues, Magn. Reson. Imaging 8 (1990) 321–331, https://doi.org/10.1016/0730-725X(90)90106-C.

[35] L. van der Weerd, M.M.A.E. Claessens, C. Efde, H. Van As, Nuclear magnetic resonanceimaging of membrane permeability changes in plants during osmoticstress, Plant Cell Environ 25 (2002) 1539–1549, https://doi.org/10.1046/j.1365-3040.2002.00934.x.

[36] M. Borghetti, S. Leonardi, A. Raschi, D. Snyderman, R. Tognetti, Ecotypic variation of xylem embolism, phenological traits, growth parameters and allozyme characteristics in Fagus sylvatica, Funct. Ecol. (1993) 713–720.

[37] J.S. Sperry, J.E.M. Sullivan, Xylem embolism in response to freeze-thaw cycles and water stress in ring-porous, diffuse-porous, and conifer species, Plant Physiol. 100 (1992) 605–613, https://doi.org/10.1104/pp.100.2.605.

[38] T. Améglio, C. Bodet, A. Lacointe, H. Cochard, Winter embolism, mechanisms of xylem hydraulic conductivity recovery and springtime growth patterns in walnut and peach trees, Tree Physiol. 22 (2002) 1211–1220, https://doi.org/10.1093/treephys/22.17.1211.

[39] H. Cochard, D. Lemoine, T. Améglio, A. Granier, Mechanisms of xylem recovery from winter embolism in Fagus sylvatica, Tree Physiol. 21 (2001) 27–33, https://doi.org/10.1093/treephys/21.1.27.

[40] J. Urban, E. Bednarova, R. Plichta, V. Gryc, H. Vavrčík, J. Hacura, M. Fajstavr, J. Kučera, Links between phenology and ecophysiology in a European beech forest, iForest-Biogeosciences and Forestry 8 (2014) 438. https://doi.org/10.3832/ifor1307-007.

[41] J.J. Sauter, B. van Cleve, Storage, mobilization and interrelations of starch, sugars, protein and fat in the ray storage tissue of poplar trees, Trees 8 (1994) 297–304, https://doi.org/10.1007/BF00202674.

[42] S. Pfautsch, Hydraulic anatomy and function of trees—basics and critical developments, Curr. Forest. Rep. 2 (2016) 236–248, https://doi.org/10.1007/s40725-016-0046-8.

[43] A.J.E. van BEL, Xylem-phloem exchange via the rays: the undervalued route of transport, J. Exp. Bot. 41 (1990) 631–644, https://doi.org/10.1093/jxb/41.6.631.

[44] M.J. Clearwater, G. Goldstein, N.M. Holbrook, M.A. Zwieniecki, Vascular transport in plants, Academic Press, Burlington, 2005, pp. 375–399.

[45] P. Copini, F.J. Vergeldt, P. Fonti, U. Sass-Klaassen, J. den Ouden, F. Sterck, M. Decuyper, E. Gerkema, C.W. Windt, H. van As, Magnetic resonance imaging suggests functional role of previous year vessels and fibres in ring-porous sap flow resumption, Tree Physiol. 39 (2019) 1009–1018, https://doi.org/10.1093/treephys/tpz019.

[46] U. Hacke (Ed.), Functional and ecological xylem anatomy, Springer, Cham, 2015.

3 Overarching discussion and literature reflection

3.1 Hypothesis I: The use of a multi-spin echo imaging pulse sequence compensates for the imperfect homogeneity and lower field strength of small-scale and open permanent magnets.

The first hypothesis was confirmed. A novel MRI approach to image plant xylem was introduced. A relatively light, open and robust permanent magnet with limited field strength and homogeneity was paired with a multi-spin echo imaging pulse sequence with short echo times and a large number of echoes. Within less than two hours quantitative water content and signal relaxation time (T_2) images were obtained with pixel sizes between 100*100 and 200*200 µm². The images provided high anatomical detail of the stem of young spruce and beech trees, allowing the different stem tissue types to be distinguished (Meixner et al., 2020; Meixner et al., 2021a). At pixel sizes between 300*300 and 360*360 µm² annual rings could still be distinguished in both types of xylem architecture, which was not possible anymore at pixel sizes above 500*500 µm².

The novel MRI approach introduced in Meixner *et al.* (2020) is advantageous compared to existing approaches of imaging plants with open small-scale magnets (Umebayashi et al., 2011; Umebayashi et al., 2016; Fukuda et al., 2015), as in all of those existing approaches single-spin echo imaging pulse sequences were used (with echo times >10 ms). The use of multi-spin echo pulse sequences with short echo times was found to compensate the shortcoming of an open small-scale magnet in different ways (see Fig. 8). The limited field strength is compensated as the signal is used more efficiently. The limited homogeneity of the magnetic field, which causes the signal to decay rapidly, is compensated by refocusing the signal as soon as possible after its excitation. Finally, another advantage of multi-spin echo imaging is that the large number of signal acquisitions allows to fit the signal for each pixel with high accuracy and to obtain quantitative water content and signal relaxation time (T_2) images.

3.2 Hypothesis II: Quantitative MR imaging allows the detection and visualization of xylem emboli, even if xylem conduits are not spatially resolved.

The second hypothesis was also confirmed. Quantitative water content and signal relaxation time (T_2) images both provided sufficient contrast between pixels that contain filled xylem conduits and those that do not in beech and spruce xylem. This provided a way to monitor xylem desiccation in angiosperm and gymnosperm xylem, even when pixel sizes were significantly larger than xylem conduits (Meixner *et al.*, 2020; Meixner *et al.*, 2021a). Combining water content (A) and signal relaxation time (T_2) images via pixelwise multiplication resulted in A*T_2 product images, which showed a higher image quality and higher signal-to-noise ratio than water content or relaxation time images individually. Also, product images were found to be more sensitive against a limited number of conduits per pixel drying down,

which was particularly beneficial when monitoring the disappearance of filled vessels in beech, which was challenging due to water remaining in smaller lumina (e.g. fibers) beyond the dry-down. On the basis of a simulation, the high sensitivity of product images to monitor xylem dry-down in beech was ascribed to a the longer T_2 values of water in larger lumina, such as vessels (Meixner *et al.*, 2020). It was further shown that monitoring the emergence of xylem emboli on the basis of $A*T_2$ product images also works at pixel sizes beyond 500*500 µm² (Meixner *et al.*, 2021a).

Existing approaches to use MRI for monitoring xylem embolism formation in trees that have been applied to gymnosperm species confirmed the relatively homogeneous xylem structure of this type of xylem architecture (Utsuzawa *et al.*, 2005; Umebayashi *et al.*, 2011; Umebayashi *et al.*, 2016). Two studies that have been conducted on angiosperm tree species were both limited in the sense that only the water in large vessels (with long T_2 values) was visualized, while signal from water in smaller lumina within the tissue surrounding the vessels was not acquired due to its short T_2 value (Zwieniecki *et al.*, 2013; Fukuda *et al.*, 2015). In Meixner *et al.* (2020) and Meixner *et al.* (2021a) it was shown that when imaging beech xylem with a sufficiently short echo time and a large number of echoes, quantitative images can be obtained that allow to also visualize water in smaller lumina next to the vessels. Quantitative water content images allowed to monitor the amount of water, while signal relaxation time images allowed to draw conclusions on the compartment size of the lumina the water is contained by. The ability to detect water in smaller as well as larger lumina provides a more complete understanding of how certain species handle drought stress, especially in case of angiosperm species.

3.3 Hypothesis III: Xylem vulnerability curves can be obtained from quantitative water content and T_2 images.

The third hypothesis could also be confirmed. Xylem vulnerability curves were successfully obtained from water content (A) as well as $A*T_2$ product images, despite the fact that the pixels of the MR images were at least five times larger than the average vessel diameter (Meixner *et al.*, 2020; Meixner *et al.*, 2021a). Different ways have been tested to obtain xylem vulnerability curves. For all tested approaches fitted vulnerability curves were in good agreement with the dry-down data (r^2 values >0.9); the most accurate vulnerability curves, however, were obtained via binarizing $A*T_2$ product images. This was ascribed to the higher contrast in $A*T_2$ product images between xylem pixels that contain filled conduits and those that do not. The approach to obtain vulnerability curves via binarizing product images was refined further by optimizing the binarization threshold on the basis of maximizing the agreement between the dry-down data and the resulting sigmodial fit; the agreement was quantified on the basis of the r^2 values. Binarizing product images was confirmed to yield accurate vulnerability curves at different spatial imaging resolutions. For beech and spruce vulnerability curves were found to be in agreement with curves obtained in other studies (Meixner *et al.*, 2020; Meixner *et al.*, 2021a).

In existing MRI dry-down studies on trees vulnerability curves have been based on pixel values directly (Zwieniecki *et al.*, 2013), and the binarization of MR images (Fukuda *et al.*, 2015; Umebayashi *et al.*, 2016). In all of those cases signal intensity images were used that are simultaneously weighted by different sample parameters (i.e. water content and T_2). In such studies the unique capability of MRI to produce quantitative images was therefore not utilized. Also, existing studies hardly ever discuss the choice of their binarization threshold, which indicates that it is not based on a strict methodological approach. Finally, the degree to which fitted vulnerability curves agree to the dry-down data is limited in some of the studies mentioned, while in Meixner *et al.* (2020) and Meixner *et al.* (2021a) the r^2 values of the sigmodial fits were above 0.9 in all cases, even when pixel sizes were above 0.5*0.5 mm².

3.4 Hypothesis IV: All imaging components can become sufficiently small and robust for imagers to be easily moved, set up and used in a greenhouse or in the field.

Lastly, also the fourth hypothesis was confirmed. A single unit mobile MRI scanner with a total weight of 45 kg was constructed. The device was based on the imaging approach presented in Meixner *et al.* (2020), which was combined with a small but powerfully gradient amplifier (Meixner *et al.*, 2021b). The gradient amplifier had been based on an existing audio amplifier design, which was tailored to the gradient coils and sequences used in Meixner *et al.* (2020) and Meixner *et al.* (2021a). The mobility of the device, as well as its functionality outdoors, was illustrated by obtaining quantitative high-quality images of the twig of an apple tree; the measurement has been conducted in an orchard at an ambient temperature of 7 °C. A second measurement was conducted to illustrate the capability of the setup to image continuously over extended time periods and despite significant fluctuations of ambient temperature and air moisture. For this purpose, a beech tree was imaged during spring leaf development over a period of two months in a greenhouse. Quantitative water content and T_2 images suggested that water and starch dynamics in the stem during spring refilling have been observed successfully in vivo.

Most existing approaches of imaging plants outdoors can be called mobile only to a limited extent, either due to the size and weight of the permanent magnet (Nagata *et al.*, 2016), or the electronics (Kimura *et al.*, 2011; Jones *et al.*, 2012). The most mobile device so far has been presented by Rokitta *et al.* (2000). It used a 52 kg, 0.47 T magnet and required 20 kg of additional electronic hardware. While this device has been shown to be capable of imaging in a greenhouse, the number of acquired images was limited, and the images were of limited quality. Further, the device of Rokitta *et al.* consisted of a number of loose, interconnected components, preventing its convenient use in the field. Existing small-scale amplifier approaches were found not to be sufficiently mobile (Jones *et al.*, 2012) or not sufficiently powerful (Rokitta *et al.*, 2000; Cooley *et al.*, 2020).

4   Conclusions and outlook

In this thesis it was shown that, in the context monitoring xylem emboli in trees non-invasively, some of the shortcomings of the MRI technology can be compensated by using a dedicated combination of hardware, imaging pulse sequences and data evaluation routines. The use of a small and open permanent magnet results in limited strength and homogeneity of the static magnetic field that the magnet provides, limiting the MRI signal and causing its rapid decay. Both properties, however, were compensated by using a multi-spin echo imaging pulse sequence (with short echo times and a large number of echoes).

As low-field MRI only provides limited spatial resolution, pixels sizes above 100*100 µm² prevented individual xylem conduits in trees to be spatially resolved. Combining quantitative water content and T_2 images via pixelwise multiplication, however, was found to generate high quality images with a high sensitivity to xylem cavitation in angiosperm and gymnosperm xylem. The correlation of compartment size and T_2 allowed to recognize the dry-down of a limited number of conduits per pixel with high sensitivity. This approach allowed to obtain accurate xylem vulnerability curves, even at pixels sizes beyond 500*500 µm².

Finally, it was shown that quantitative high-quality images can also be obtained in the field or greenhouse, by combining the small open magnet and the multi-spin echo pulse sequence with a tailored mobile gradient amplifier. As the amplifier was based on a well-known design and cheap parts, this approach not only demonstrated a way to make quantitative imaging of plants mobile and suitable for outdoor measurements, but also showed that it can be made more affordable.

Accordingly, MRI has potential beyond its current use to study plant hydraulics. The ability to image plant stems with small and open magnets of a simple design has a number of beneficial implications. The limited size and weight makes the magnets relatively cheap and mobile, while the fact that they are open allows their convenient use when imaging plant stems. Cheaper MRI devices based on such magnets can reduce the cost for measurement time and allow to continuously image xylem dry-down (and potentially also refilling) of larger numbers of samples, and to obtain vulnerability curves non-invasively, even in the field. This can provide a broader basis of in vivo data to verify existing hydraulic methods, but also to tackle unresolved questions around repair, plasticity, segmentation, and potentially also questions regarding the plant metabolism under water stress.

A better understanding of these questions is expected to provide answers regarding the vulnerability to drought stress of present-day forests and to allow more accurate future predictions. Understanding of this kind will further assist to choose species and varieties, as more plants are expected to face higher temperatures and less precipitation. Also, the optimization of watering strategies for crops will

benefit from a better understanding of the dynamics of xylem water and repair, as plants face drought stress.

Future challenges that have to be resolved to make MRI more accessible to plant scientist mostly are linked to its complexity. The biggest challenge probably is to make the technology failsafe and automate it to a degree so that it can be easily used by non-MRI-experts on a daily basis (e.g optimization of a large number of imaging parameters), while keeping the hardware and programming costs within affordable limits.

Finally, the NMR principle provides a unique way to directly and non-invasively obtain a full distribution of flow velocities for each pixel of an MR image. The components presented and used in this thesis (magnet, gradient coils and amplifiers) have been designed so that they are capable of flow measurements in the xylem and phloem. The implementation of this functionality would open a new set of possible applications, e.g. to base xylem vulnerability curves on the actual percentage loss of conductivity, obtained via non-invasive xylem flow measurements.

5   References

Alder, NN, Pockmann, JS, Nuismer, S. 1996. Use of centrifugal force in the study of xylem cavitation. *Journal of experimental botany* **48**: 665–674.

Allen, CD, Macalady, AK, Chenchouni, H, Bachelet, D, McDowell, N, Vennetier, M, Kitzberger, T, Rigling, A, Breshears, DD, Hogg, ET. 2010. A global overview of drought and heat-induced tree mortality reveals emerging climate change risks for forests. *Forest ecology and management* **259**: 660–684.

Anderegg, WRL. 2015. Spatial and temporal variation in plant hydraulic traits and their relevance for climate change impacts on vegetation. *New Phytologist* **205**: 1008–1014.

Barigah, TS, Charrier, O, Douris, M, Bonhomme, M, Herbette, S, Améglio, T, Fichot, R, Brignolas, F, Cochard, H. 2013. Water stress-induced xylem hydraulic failure is a causal factor of tree mortality in beech and poplar. *Annals of botany* **112**: 1431–1437.

Bauerle, WL, Hinckley, TM, Cermak, J, Kucera, J, Bible, K. 1999. The canopy water relations of old-growth Douglas-fir trees. *Trees* **13**: 211–217.

Bouda, M, Windt, CW, McElrone, AJ, Brodersen, CR. 2019. In vivo pressure gradient heterogeneity increases flow contribution of small diameter vessels in grapevine. *Nature communications* **10**: 1–10.

Briggs, LJ. 1950. Limiting negative pressure of water. *Journal of Applied Physics* **21**: 721–722.

Brodersen, CR, Lee, EF, Choat, B, Jansen, S, Phillips, RJ, Shackel, KA, McElrone, AJ, Matthews, MA. 2011. Automated analysis of three-dimensional xylem networks using high-resolution computed tomography. *The New phytologist* **191**: 1168–1179.

Brodersen, CR, McElrone, AJ. 2013. Maintenance of xylem Network Transport Capacity. A Review of Embolism Repair in Vascular Plants. *Frontiers in plant science* **4**: 108.

Brodersen, CR, McElrone, AJ, Choat, B, Lee, EF, Shackel, KA, Matthews, MA. 2013. In vivo visualizations of drought-induced embolism spread in Vitis vinifera. *Plant physiology* **161**: 1820–1829.

Brodersen, CR, McElrone, AJ, Choat, B, Matthews, MA, Shackel, KA. 2010. The dynamics of embolism repair in xylem. In vivo visualizations using high-resolution computed tomography. *Plant physiology* **154**: 1088–1095.

Brodersen, CR, Roddy, AB, Wason, JW, McElrone, AJ. 2019. Functional Status of Xylem Through Time. *Annual review of plant biology*.

Brodribb, TJ, Carriqui, M, Delzon, S, Lucani, C. 2017. Optical measurement of stem xylem vulnerability. *Plant Physiology* **174**: 2054–2061.

Brodribb, TJ, Cochard, H. 2009. Hydraulic failure defines the recovery and point of death in water-stressed conifers. *Plant physiology* **149**: 575–584.

Brodribb, TJ, Powers, J, Cochard, H, Choat, B. 2020. Hanging by a thread? Forests and drought. *Science (New York, N.Y.)* **368**: 261–266.

Brown, HR. 2013. The theory of the rise of sap in trees: some historical and conceptual remarks. *Physics in Perspective* **15**: 320–358.

Brown, RW, Cheng, Y-CN, Haacke, EM, Thompson, MR, Venkatesan, R. 2014. Magnetic resonance imaging: physical principles and sequence design: John Wiley & Sons.

Brownstein, KR, Tarr, CE. 1979. Importance of classical diffusion in NMR studies of water in biological cells. *Physical review A* **19**: 2446.

Callaghan, PT. 1991. Principles of NMR Microscopy, Clarendon: Oxford.

Caupin, F, Arvengas, A, Davitt, K, Azouzi, MEM, Shmulovich, KI, Ramboz, C, Sessoms, DA, Stroock, AD. 2012. Exploring water and other liquids at negative pressure. *Journal of Physics: Condensed Matter* **24**: 284110.

Caupin, F, Herbert, E. 2006. Cavitation in water: a review. *Comptes Rendus Physique* **7**: 1000–1017.

Chavhan, GB, Babyn, PS, Thomas, B, Shroff, MM, Haacke, EM. 2009. Principles, techniques, and applications of T2*-based MR imaging and its special applications. *Radiographics* **29**: 1433–1449.

Choat, B, Badel, E, Burlett, R, Delzon, S, Cochard, H, Jansen, S. 2016. Noninvasive Measurement of Vulnerability to Drought-Induced Embolism by X-Ray Microtomography. *Plant physiology* **170**: 273–282.

Choat, B, Brodersen, CR, McElrone, AJ. 2015. Synchrotron X-ray microtomography of xylem embolism in Sequoia sempervirens saplings during cycles of drought and recovery. *The New phytologist* **205**: 1095–1105.

Choat, B, Brodribb, TJ, Brodersen, CR, Duursma, RA, López, R, Medlyn, BE. 2018. Triggers of tree mortality under drought. *Nature* **558**: 531–539.

Choat, B, Drayton, WM, Brodersen, C, Matthews, MA, Shackel, KA, Wada, H, McElrone, AJ. 2010. Measurement of vulnerability to water stress-induced cavitation in grapevine. A

comparison of four techniques applied to a long-vesseled species. *Plant, cell & environment* **33**: 1502–1512.

Choat, B, Jansen, S, Brodribb, TJ, Cochard, H, Delzon, S, Bhaskar, R, Bucci, SJ, Feild, TS, Gleason, SM, Hacke, UG. 2012. Global convergence in the vulnerability of forests to drought. *Nature* **491**: 752–755.

Clearwater, MJ, Clark, CJ. 2003. In vivo magnetic resonance imaging of xylem vessel contents in woody lianas. *Plant, Cell and Environment* **26**: 1205–1214.

Cochard, H. 2002. A technique for measuring xylem hydraulic conductance under high negative pressures. *Plant, Cell and Environment* **25**: 815–819.

Cochard, H, Badel, E, Herbette, S, Delzon, S, Choat, B, Jansen, S. 2013. Methods for measuring plant vulnerability to cavitation. A critical review. *Journal of experimental botany* **64**: 4779–4791.

Cochard, H, Delzon, S, Badel, E. 2015. X-ray microtomography (micro-CT). A reference technology for high-resolution quantification of xylem embolism in trees. *Plant, cell & environment* **38**: 201–206.

Cochard, H, Lemoine, D, Améglio, T, Granier, A. 2001. Mechanisms of xylem recovery from winter embolism in Fagus sylvatica. *Tree physiology* **21**: 27–33.

Cooley, CZ, Stockmann, JP, Witzel, T, LaPierre, C, Mareyam, A, Jia, F, Zaitsev, M, Wenhui, Y, Zheng, W, Stang, P. 2020. Design and implementation of a low-cost, tabletop MRI scanner for education and research prototyping. *Journal of Magnetic Resonance* **310**: 106625.

Couvreur, V, Ledder, G, Manzoni, S, Way, DA, Muller, EB, Russo, SE. 2018. Water transport through tall trees: a vertically explicit, analytical model of xylem hydraulic conductance in stems. *Plant, Cell and Environment* **41**: 1821–1839.

Cruiziat, P, Cochard, H, Améglio, T. 2002. Hydraulic architecture of trees. Main concepts and results. *Annals of Forest Science* **59**: 723–752.

Dai, A. 2013. Increasing drought under global warming in observations and models. *Nature Climate Change* **3**: 52–58.

Davitt, K, Arvengas, A, Caupin, F. 2010. Water at the cavitation limit: Density of the metastable liquid and size of the critical bubble. *EPL (Europhysics Letters)* **90**: 16002.

Debenedetti, PG. 1996. Metastable liquids. Concepts and principles: Princeton University Press.

Denny, M. 2011. Tree hydraulics: how sap rises. *European Journal of Physics* **33**: 43.

Dhondt, S, Vanhaeren, H, van Loo, D, Cnudde, V, Inzé, D. 2010. Plant structure visualization by high-resolution X-ray computed tomography. *Trends in plant science* **15**: 419–422.

Dixon, HH, Joly, J. 1894. On the ascent of sap. *Proceedings of the Royal Society of London* **57**: 3–5.

Edzes, HT, van Dusschoten, D, van As, H. 1998. Quantitative T2 imaging of plant tissues by means of multi-echo MRI microscopy. *Magnetic Resonance Imaging* **16**: 185–196.

Franc, J-P, Michel, J-M. 2006. Fundamentals of cavitation: Springer Science & Business Media.

Fukuda, K, Kawaguchi, D, Aihara, T, Ogasa, MY, Miki, NH, Haishi, T, Umebayashi, T. 2015. Vulnerability to cavitation differs between current-year and older xylem. Non-destructive observation with a compact magnetic resonance imaging system of two deciduous diffuse-porous species. *Plant, cell & environment* **38**: 2508–2518.

Fukuda, K, Utsuzawa, S, Sakaue, D. 2007. Correlation between acoustic emission, water status and xylem embolism in pine wilt disease. *Tree physiology* **27**: 969–976.

Galloway, WJ. 1954. An experimental study of acoustically induced cavitation in liquids. *The Journal of the Acoustical Society of America* **26**: 849–857.

Gennes, P-G de, **Brochard-Wyart, F, Quéré, D. 2013.** Capillarity and wetting phenomena: drops, bubbles, pearls, waves: Springer Science & Business Media.

Gibson, L, Lee, TM, Koh, LP, Brook, BW, Gardner, TA, Barlow, J, Peres, CA, Bradshaw, CJA, Laurance, WF, Lovejoy, TE. 2011. Primary forests are irreplaceable for sustaining tropical biodiversity. *Nature* **478**: 378–381.

H. Y. Carr and E. M. Purcell. 1954. Effects of Diffusion on Free Precession in Nuclear Magnetic Resonance Experiments.

Hacke, UG, Sperry, JS, Pockman, WT, Davis, SD, McCulloh, KA. 2001. Trends in wood density and structure are linked to prevention of xylem implosion by negative pressure. *Oecologia* **126**: 457–461.

Hacke, UG, Venturas, MD, MacKinnon, ED, Jacobsen, AL, Sperry, JS, Pratt, RB. 2015. The standard centrifuge method accurately measures vulnerability curves of long-vesselled olive stems. *New Phytologist* **205**: 116–127.

Hahn, EL. 1950. Spin echoes. *Physical review* **80**: 580.

Henderson, aSJ, Speedy, RJ. 1980. A Berthelot-Bourdon tube method for studying water under tension. *Journal of Physics E: Scientific Instruments* **13**: 778.

**Hochberg, U, Albuquerque, C, Rachmilevitch, S, Cochard, H, David-Schwartz, R, Brodersen,
CR, McElrone, A, Windt, CW. 2016a.** Grapevine petioles are more sensitive to drought
induced embolism than stems. Evidence from in vivo MRI and microcomputed
tomography observations of hydraulic vulnerability segmentation. *Plant, cell &
environment* **39**: 1886–1894.

Hochberg, U, Herrera, JC, Cochard, H, Badel, E. 2016b. Short-time xylem relaxation results in
reliable quantification of embolism in grapevine petioles and sheds new light on their
hydraulic strategy. *Tree physiology* **36**: 748–755.

Holbrook, NM, Ahrens E. T., Burns M. J., Zwieniecki, MA. 2001. In Vivo Observation of
Cavitation and Embolism Repair Using Magnetic Resonance Imaging. *Plant physiology* **126**:
27–31.

Homan, NM, Windt, CW, Vergeldt, FJ, Gerkema, E, Van As, H. 2007. 0.7 and 3 T MRI and
Sap Flow in Intact Trees. Xylem and Phloem in Action. *Applied Magnetic Resonance* **32**:
157–170.

Jackson, GE, Grace, J. 1996. Field measurements of xylem cavitation. Are acoustic emissions
useful? *Journal of experimental botany* **47**: 1643–1650.

Jacobsen, AL, Pratt, RB. 2012. No evidence for an open vessel effect in centrifuge-based
vulnerability curves of a long-vesselled liana (Vitis vinifera). *The New phytologist* **194**: 982–
990.

Jones, M, Aptaker, PS, Cox, J, Gardiner, BA, McDonald, PJ. 2012. A transportable magnetic
resonance imaging system for in situ measurements of living trees. The Tree Hugger.
Journal of magnetic resonance (San Diego, Calif. : 1997) **218**: 133–140.

Jurin, J. 1718. II. An account of some experiments shown before the Royal Society; with an
enquiry into the cause of the ascent and suspension of water in capillary tubes.
Philosophical Transactions of the Royal Society of London **30**: 739–747.

Kaufmann, I, Schulze-Till T., Schneider, HU, Zimmermann U., Jakob P., Wegner L. H. 2009.
Functional repair of embolized vessels in maize roots after temporal drought stress, as
demonstrated by magnetic resonance imaging. *The New phytologist* **184**: 245–256.

Keenan, TF, Williams, CA. 2018. The terrestrial carbon sink. *Annual Review of Environment
and Resources* **43**: 219–243.

Kimura, T, Geya, Y, Terada, Y, Kose, K, Haishi, T, Gemma, H, Sekozawa, Y. 2011. Development of a mobile magnetic resonance imaging system for outdoor tree measurements. *The Review of scientific instruments* **82**: 53704.

Kleinberg, RL. 1999. 9. Nuclear Magnetic Resonance. In: Experimental methods in the physical sciences: Elsevier, 337–385.

Koch, GW, Sillett, SC, Jennings, GM, Davis, SD. 2004. The limits to tree height. *Nature* **428**: 851–854.

Lipp, G, Körber, CH, Englich, S, Hartmann, U, Rau, G. 1987. Investigation of the behavior of dissolved gases during freezing. *Cryobiology* **24**: 489–503.

Mayr, S, Sperry, JS. 2010. Freeze–thaw-induced embolism in Pinus contorta: centrifuge experiments validate the 'thaw-expansion hypothesis' but conflict with ultrasonic emission data. *New Phytologist* **185**: 1016–1024.

McDowell, N, Pockman, WT, Allen, CD, Breshears, DD, Cobb, N, Kolb, T, Plaut, J, Sperry, J, West, A, Williams, DG, Yepez, EA. 2008. Mechanisms of plant survival and mortality during drought. Why do some plants survive while others succumb to drought? *The New phytologist* **178**: 719–739.

Meadley, SL, Angell, CA. 2015. Water and its relatives: The stable, supercooled and particularly the stretched regimes. *Water: Fundamentals as the Basis for Understanding the Environment and Promoting Technology* **187**: 19.

Meiboom, S, Gill, D. 1958. Modified Spin-Echo Method for Measuring Nuclear Relaxation Times. *Review of Scientific Instruments* **29**: 688–691.

Meixner, M, Foerst, P, Windt, CW. 2021a. Reduced spatial resolution MRI suffices to image and quantify drought induced embolism formation in trees. *Plant methods* **17**: 1–12.

Meixner, M, Kochs, J, Foerst, P, Windt, CW. 2021b. An integrated magnetic resonance plant imager for mobile use in greenhouse and field. *Journal of Magnetic Resonance* **323**: 106879.

Meixner, M, Tomasella, M, Foerst, P, Windt, CW. 2020. A small-scale MRI scanner and complementary imaging method to visualize and quantify xylem embolism formation. *New Phytologist* **226**: 1517–1529.

Melcher, PJ, Zwieniecki, MA, Holbrook, NM. 2003. Vulnerability of xylem vessels to cavitation in sugar maple. Scaling from individual vessels to whole branches. *Plant physiology* **131**: 1775–1780.

Nagata, A, Kose, K, Terada, Y. 2016. Development of an outdoor MRI system for measuring flow in a living tree. *Journal of magnetic resonance (San Diego, Calif. : 1997)* **265**: 129–138.

Nardini, A, Savi, T, Losso, A, Petit, G, Pacilè, S, Tromba, G, Mayr, S, Trifilò, P, Lo Gullo, MA, Salleo, S. 2017. X-ray microtomography observations of xylem embolism in stems of Laurus nobilis are consistent with hydraulic measurements of percentage loss of conductance. *The New phytologist* **213**: 1068–1075.

Nolf, M, Lopez, R, Peters, JMR, Flavel, RJ, Koloadin, LS, Young, IM, Choat, B. 2017. Visualization of xylem embolism by X-ray microtomography. A direct test against hydraulic measurements. *The New phytologist* **214**: 890–898.

Oertli, JJ. 1971. Stability of water under tension in the xylem. *Zeitschrift fur Pflanzenphysiologie*.

Papastefanou, P, Zang, CS, Pugh, T am, **Liu, D, Grams, TEE, Hickler, T, Rammig, A. 2020.** A dynamic model for strategies and dynamics of plant water-potential regulation under drought conditions. *Frontiers in plant science* **11**: 373.

Park Williams, A, Allen, CD, Macalady, AK, Griffin, D, Woodhouse, CA, Meko, DM, Swetnam, TW, Rauscher, SA, Seager, R, Grissino-Mayer, HD, Dean, JS, Cook, ER, Gangodagamage, C, Cai, M, McDowell, NG. 2013. Temperature as a potent driver of regional forest drought stress and tree mortality. *Nature Climate Change* **3**: 292–297.

Petruzzellis, F, Pagliarani, C, Savi, T, Losso, A, Cavalletto, S, Tromba, G, Dullin, C, Bär, A, Ganthaler, A, Miotto, A. 2018. The pitfalls of in vivo imaging techniques. Evidence for cellular damage caused by synchrotron X-ray computed micro-tomography. *New Phytologist* **220**: 104–110.

Petty, JA. 1978. Fluid flow through the vessels of birch wood. *Journal of experimental botany* **29**: 1463–1469.

Petty, JA. 1981. Fluid flow through the vessels and intervascular pits of sycamore wood. *Holzforschung* **35**: 213–216.

Pickard, WF. 1981. The ascent of sap in plants. *Progress in biophysics and molecular biology* **37**: 181–229.

Pockman, WT, Sperry, JS, O'Leary, JW. 1995. Sustained and significant negative water pressure in xylem. *Nature* **378**: 715–716.

Poon, CS, Henkelman, RM. 1992. Practical T2 quantitation for clinical applications. *Journal of Magnetic Resonance Imaging* **2**: 541–553.

Reece, JB, Urry, LA, Cain, ML, Wasserman, SA, Minorsky, PV, Jackson, RB. 2014. Campbell biology: Pearson Boston.

Robert, E, Schmitz, N, Copini, P, Gerkema, E, Vergeldt, FJ, Windt, CW, Beeckman, H, Koedam, N, van As, H. 2014. Visualization of the stem water content of two genera with secondary phloem produced by successive cambia through Magnetic Resonance Imaging (MRI). *Journal of Plant Hydraulics* **1**: e006-e006.

Rokitta, M, Rommel, E, Zimmermann, U, Haase, A. 2000. Portable nuclear magnetic resonance imaging system. *Review of Scientific Instruments* **71**: 4257.

Rosner, S, Klein, A, Wimmer, R, Karlsson, B. 2006. Extraction of features from ultrasound acoustic emissions. A tool to assess the hydraulic vulnerability of Norway spruce trunkwood? *The New phytologist* **171**: 105–116.

Savi, T, Miotto, A, Petruzzellis, F, Losso, A, Pacilè, S, Tromba, G, Mayr, S, Nardini, A. 2017. Drought-induced embolism in stems of sunflower. A comparison of in vivo micro-CT observations and destructive hydraulic measurements. *Plant physiology and biochemistry : PPB* **120**: 24–29.

Scheenen, TW, van Dusschoten, D, Jager, PA de, **Van As, H. 2000.** Microscopic displacement imaging with pulsed field gradient turbo spin-echo NMR. *Journal of magnetic resonance (San Diego, Calif. : 1997)* **142**: 207–215.

Schepper, V de, **van Dusschoten, D, Copini, P, Jahnke, S, Steppe, K. 2012.** MRI links stem water content to stem diameter variations in transpiring trees. *Journal of experimental botany* **63**: 2645–2653.

Schlesinger, WH, Jasechko, S. 2014. Transpiration in the global water cycle. *Agricultural and Forest Meteorology* **189**: 115–117.

Scholander, PF, Bradstreet, ED, Hemmingsen, EA, Hammel, HT. 1965. Sap pressure in vascular plants: negative hydrostatic pressure can be measured in plants. *Science (New York, N.Y.)* **148**: 339–346.

Schuldt, B, Buras, A, Arend, M, Vitasse, Y, Beierkuhnlein, C, Damm, A, Gharun, M, Grams, TEE, Hauck, M, Hajek, P. 2020. A first assessment of the impact of the extreme 2018 summer drought on Central European forests. *Basic and Applied Ecology* **45**: 86–103.

Schweingruber, FH. 1990. Anatomy of European woods. Bern, CH: Verlag Paul Haupt, 1990.

Snaar, H. Van As. 1992. Probing water compartments and membrane permeability in plant cells by 1H NMR relaxation measurements.

Sperry, J. 2013. Cutting-edge research or cutting-edge artefact? An overdue control experiment complicates the xylem refilling story. *Plant, cell & environment* **36**: 1916–1918.

Sperry, JS. 2011. Hydraulics of vascular water transport. In: Mechanical integration of plant cells and plants: Springer, 303–327.

Sperry, JS, Christman, MA, Torres-Ruiz, JM, Taneda, H, Smith, DD. 2012. Vulnerability curves by centrifugation. Is there an open vessel artefact, and are 'r' shaped curves necessarily invalid? *Plant, cell & environment* **35**: 601–610.

Sperry, JS, Sullivan, JEM. 1992. Xylem embolism in response to freeze-thaw cycles and water stress in ring-porous, diffuse-porous, and conifer species. *Plant Physiology* **100**: 605–613.

Sutcliffe, J. 1968. Plants and water. *Plants and water*.

Suuronen, J-P, Peura, M, Fagerstedt, K, Serimaa, R. 2013. Visualizing water-filled versus embolized status of xylem conduits by desktop x-ray microtomography. *Plant methods* **9**: 11.

Tobin, MF, Pratt, RB, Jacobsen, AL, Guzman, ME de. **2013.** Xylem vulnerability to cavitation can be accurately characterised in species with long vessels using a centrifuge method. *Plant biology (Stuttgart, Germany)* **15**: 496–504.

Torres-Ruiz, JM, Cochard, H, Mayr, S, Beikircher, B, Diaz-Espejo, A, Rodriguez-Dominguez, CM, Badel, E, Fernández, JE. 2014. Vulnerability to cavitation in Olea europaea current-year shoots. Further evidence of an open-vessel artifact associated with centrifuge and air-injection techniques. *Physiologia Plantarum* **152**: 465–474.

Tötzke, C, Miranda, T, Konrad, W, Gout, J, Kardjilov, N, Dawson, M, Manke, I, Roth-Nebelsick, A. 2013. Visualization of embolism formation in the xylem of liana stems using neutron radiography. *Annals of botany* **111**: 723–730.

Trenberth, KE, Dai, A, van der Schrier, G, Jones, PD, Barichivich, J, Briffa, KR, Sheffield, J. 2014. Global warming and changes in drought. *Nature Climate Change* **4**: 17–22.

Trevena, DH. 1984. Cavitation and the generation of tension in liquids. *Journal of Physics D: Applied Physics* **17**: 2139.

Trifilò, P, Raimondo, F, Lo Gullo, MA, Barbera, PM, Salleo, S, Nardini, A. 2014. Relax and refill. Xylem rehydration prior to hydraulic measurements favours embolism repair in stems and generates artificially low PLC values. *Plant, cell & environment* **37**: 2491–2499.

Tyree, MT, Sperry, JS. 1988. Do woody plants operate near the point of catastrophic xylem dysfunction caused by dynamic water stress? Answers from a model. *Plant Physiology* **88**: 574–580.

Tyree, MT, Sperry, JS. 1989. Vulnerability of xylem to cavitation and embolism. *Annual Review of Plant Physiology and Plant Molecular Biology* **40**: 19–36.

Tyree, MT, Zimmermann, MH. 1971. The theory and practice of measuring transport coefficients and sap flow in the xylem of red maple stems (Acer rubrum). *Journal of experimental botany* **22**: 1–18.

Tyree and Zimmermann. 2002. Xyelm Structure and the Ascent of Sap. *Springer*.

Umebayashi, T, Fukuda, K, Haishi, T, Sotooka, R, Zuhair, S, Otsuki, K. 2011. The developmental process of xylem embolisms in pine wilt disease monitored by multipoint imaging using compact magnetic resonance imaging. *Plant physiology* **156**: 943–951.

Umebayashi, T, Morita, T, Utsumi, Y, Kusumoto, D, Yasuda, Y, Haishi, T, Fukuda, K. 2016. Spatial distribution of xylem embolisms in the stems of Pinus thunbergii at the threshold of fatal drought stress. *Tree physiology* **36**: 1210–1218.

Urli, M, Porté, AJ, Cochard, H, Guengant, Y, Burlett, R, Delzon, S. 2013. Xylem embolism threshold for catastrophic hydraulic failure in angiosperm trees. *Tree physiology* **33**: 672–683.

Utsuzawa, S, Fukuda, K, Sakaue, D. 2005. Use of magnetic resonance microscopy for the nondestructive observation of xylem cavitation caused by pine wilt disease. *Phytopathology* **95**: 737–743.

van As, H, Scheenen, T, Vergeldt, FJ. 2009. MRI of intact plants. *Photosynthesis research* **102**: 213–222.

van der Weerd, L, Claessens, MMAE, Ruttink, T, Vergeldt, FJ, Schaafsma, TJ, van As, H. 2001. Quantitative NMR microscopy of osmotic stress responses in maize and pearl millet. *Journal of experimental botany* **52**: 2333–2343.

Venturas, MD, MacKinnon, ED, Jacobsen, AL, Pratt, RB. 2015. Excising stem samples underwater at native tension does not induce xylem cavitation. *Plant, Cell and Environment* **38**: 1060–1068.

Venturas, MD, Pratt, RB, Jacobsen, AL, Castro, V, Fickle, JC, Hacke, UG. 2019. Direct comparison of four methods to construct xylem vulnerability curves. Differences among techniques are linked to vessel network characteristics. *Plant, cell & environment*.

Venturas, MD, Sperry, JS, Hacke, UG. 2017. Plant xylem hydraulics. What we understand, current research, and future challenges. *Journal of integrative plant biology* **59**: 356–389.

Wang, Y, Lee, J, Werber, JR, Elimelech, M. 2020. Capillary-driven desalination in a synthetic mangrove. *Science advances* **6**: eaax5253.

Wheeler, JK, Huggett, BA, Tofte, AN, Rockwell, FE, Holbrook, NM. 2013. Cutting xylem under tension or supersaturated with gas can generate PLC and the appearance of rapid recovery from embolism. *Plant, cell & environment* **36**: 1938–1949.

Wheeler, TD, Stroock, AD. 2008. The transpiration of water at negative pressures in a synthetic tree. *Nature* **455**: 208–212.

Windt, CW, Vergeldt, FJ, van As, H. 2007. Correlated displacement-T2 MRI by means of a Pulsed Field Gradient-Multi Spin Echo Method. *Journal of magnetic resonance (San Diego, Calif. : 1997)* **185**: 230–239.

Wojtaszek, P. 2011. Mechanical integration of plant cells and plants: Springer Science & Business Media.

Zheng, Q, Durben, DJ, Wolf, GH, Angell, CA. 1991. Liquids at large negative pressures: water at the homogeneous nucleation limit. *Science (New York, N.Y.)* **254**: 829–832.

Zwieniecki, MA, Holbrook, NM. 2009. Confronting Maxwell's demon: biophysics of xylem embolism repair. *Trends in plant science* **14**: 530–534.

Zwieniecki, MA, Melcher, PJ, Ahrens, ET. 2013. Analysis of spatial and temporal dynamics of xylem refilling in Acer rubrum L. using magnetic resonance imaging. *Frontiers in plant science* **4**: 265.

6 Acknowledgements

7   Appendix: Supplementary material of embedded publications

7.1   Publication I: A small-scale MRI scanner and complementary imaging method to visualize and quantify xylem embolism formation

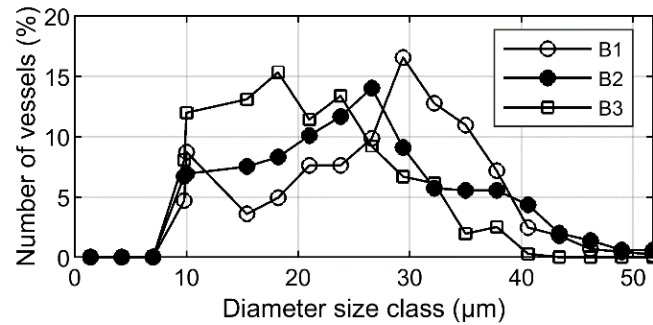Marco Meixner, Martina Tomasella, Petra Foerst, Carel Windt

Figure S1: Conduit diameter distributions of the microscopic cross sections of beech (*Fagus sylvatica*) shown in Fig. 1. Mean diameter values in μm are $B1_{mean}$ = 28.5, $B2_{mean}$ = 24.9, $B3_{mean}$ = 20.2.
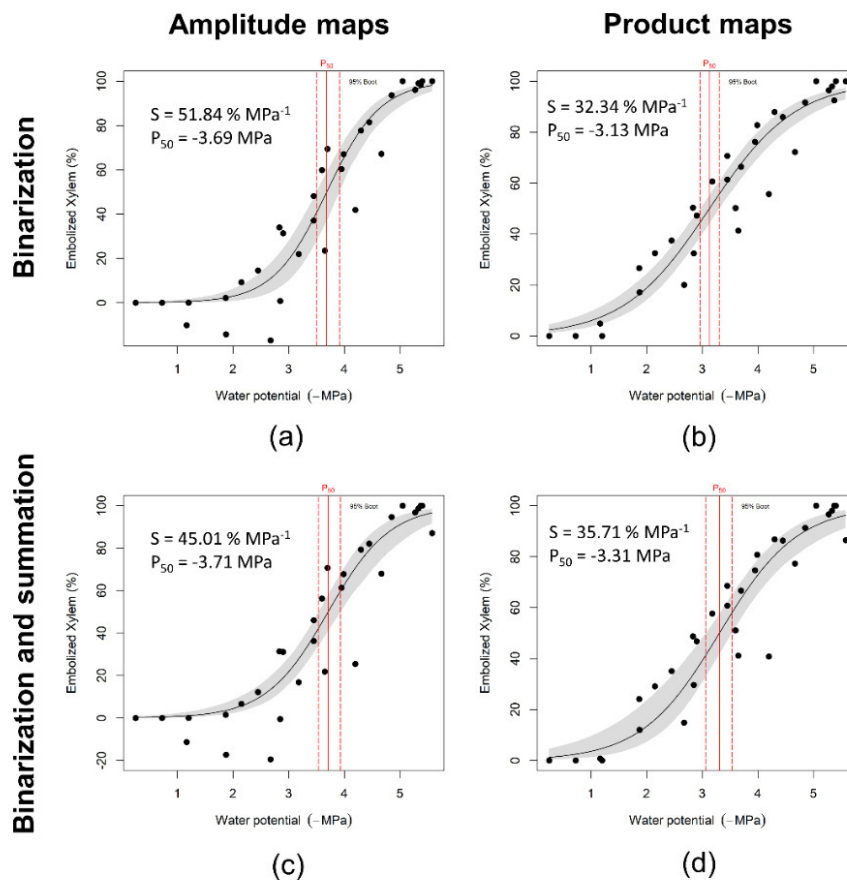

Figure S2: The three beech trees (Fagus sylvatica) were grouped together to compare the four methods shown in Fig. 6 by using the fitPLC with a sigmodial model and 1000 resamples.

Table S1: r^2, slopes and Ψ_{50} of vulnerability curves of three beech (Fagus sylvatica) trees shown in Fig. 7. Curves were acquired via applying a threshold to amplitude (a) and product (b) images and counting the number of pixels that contained values above that threshold at a certain water potential; in a second step VCs were obtained by using the mask created by thresholding amplitude and product images and summing up the amplitude values of all the pixels inside of them (c and d). The slope (S) indicates how fast the dry-down happens; Ψ_{50} is the water potential value at which 50% of the vessels are embolized, indicating the position of the curve; the coefficient of determination R^2 is a measure for how well the data suits the sigmodial fit function.

|		r^2	S (% MPa^{-1})	Ψ_{50} (MPa)
(a)	B1	0.98	-44.07 ± 2.45	-3.58 ± 0.09
	B2	0.87	-48.59 ± 11.17	-4.12 ± 0.18
	B3	0.96	-44.63 ± 1.85	-3.47 ± 0.07
(b)	B1	0.99	-33.42 ± 1.03	-2.84 ± 0.02
	B2	0.96	-29.48 ± 1.94	-3.74 ± 0.06
	B3	0.98	-29.67 ± 1.01	-2.97 ± 0.08
(c)	B1	0.97	-48.37 ± 4.72	-3.62 ± 0.07
	B2	0.84	-47.49 ± 20.90	-4.29 ± 0.32
	B3	0.96	-46.92 ± 6.82	-3.47 ± 0.09
(d)	B1	0.99	-34.06 ± 0.98	-2.93 ± 0.05
	B2	0.92	-30.50 ± 4.02	-3.86 ± 0.16
	B3	0.99	-31.21 ± 3.71	-3.02 ± 0.07

Video S1-S3: Videos of the time series of magnetic resonance product (A*T$_2$) images of the stem of three beech (*Fagus sylvatica*) trees, acquired during progressive dry down. The plant is indicated in the upper left corner (B1, B2, B3); the corresponding water potential is indicated in the lower left corner. The number of images per plant is 14 for B1, 10 for B2 and 7 for B3.

7.2   Publication II: Reduced spatial resolution MRI suffices to image and quantify

drought induced embolism formation in trees

Marco Meixner, Petra Foerst, Carel Windt
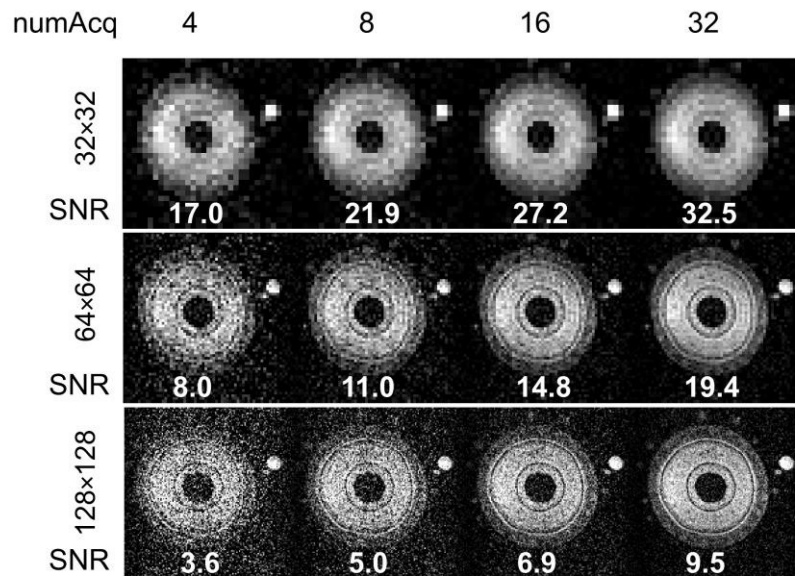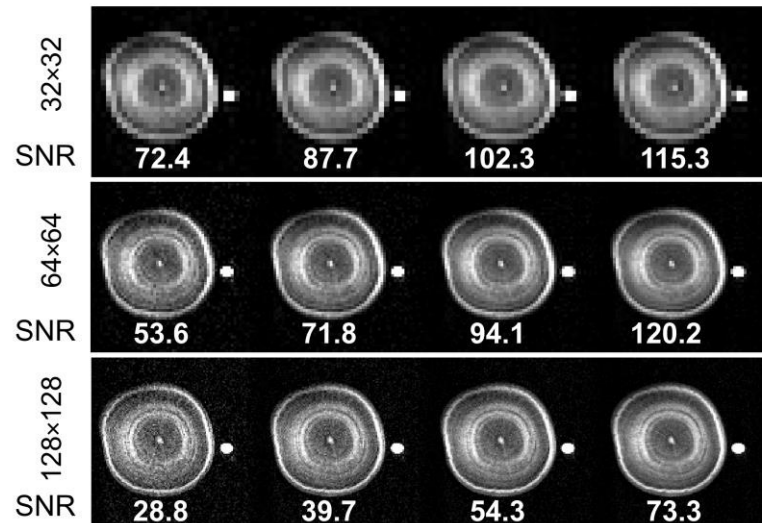
Figure S1: First echo images of well-watered spruce (a) and beech (b), acquired with an MSE imaging sequence, illustrating the dependency of image quality and signal-to-noise ratio on matrix size and the number of acquisitions averaged (numAcq). The respective SNR is printed under each image.
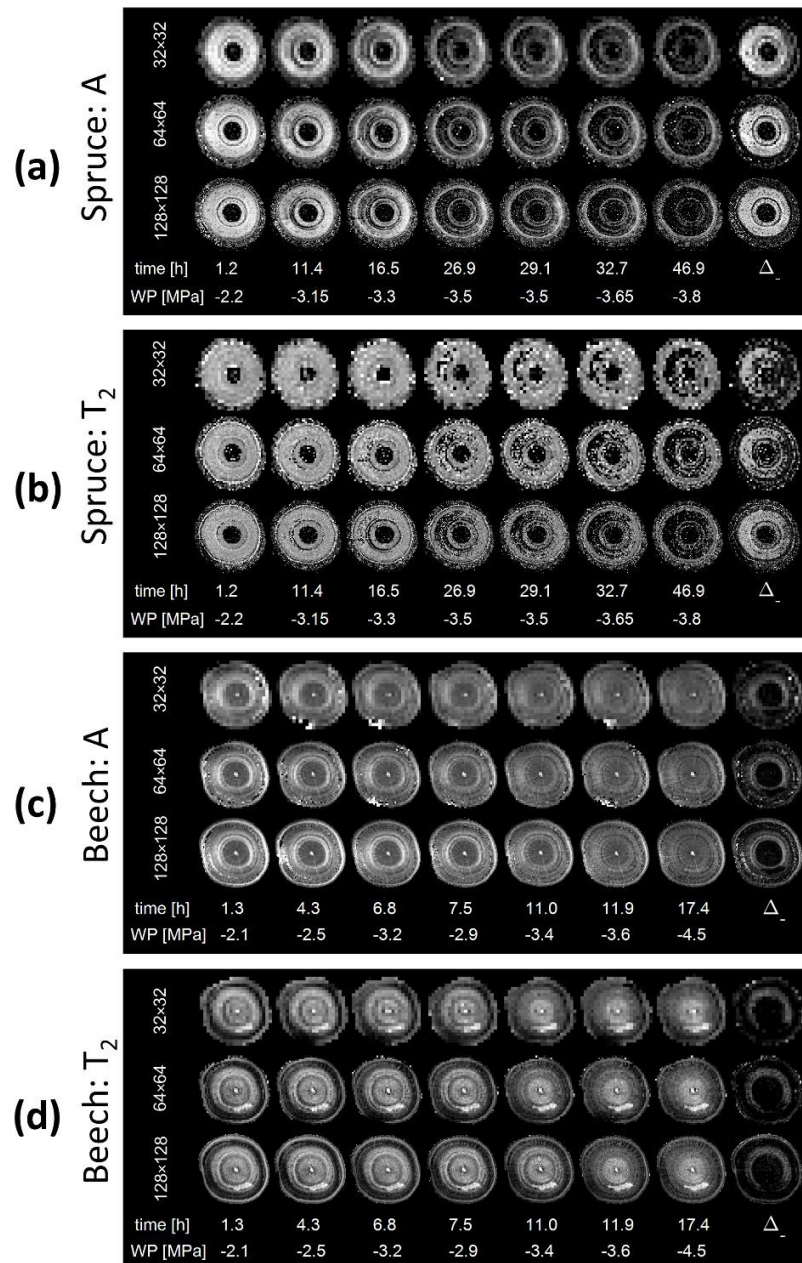
Figure S2: Fig. 3: Water content (A) and T_2 maps of xylem embolism formation in spruce (a,b) and beech (c,d), acquired with matrix sizes of 32x32, 64x64 and 128x128 pixels, shown in dependence of time and water potential (WP). In all panels (a-d), the positive difference in image intensity between the first and the last image is shown in the rightmost position (Δ_+).

Figure S3,S4: Animated illustration of the xylem dry-down of spruce (S3) and beech (S4). Water content (A), T_2 and $A*T_2$ maps are displayed at different imaging matrices (32×32, 64×64 and 128×128), all with the same field of view. In the upper right corner the time and water potential values corresponding with each image are shown.

7.3   Publication III: An integrated magnetic resonance plant imager for mobile use in greenhouse and field

Marco Meixner, Johannes Kochs, Petra Foerst, Carel Windt

Supplementary video S1: Animation of the amplitude (A), relaxation time (T_2) and A*T_2 product images of a beech tree, acquired during 62 days of bud flushing, leaf development and leaf maturation. A photo indicating the developmental stage of the tree and its buds is shown next to the parameter images. Time elapsed is indicated in the upper left corner in days. Image intensities are scaled as indicated in Fig. 7.

Supplementary video S2a: Animations of the changes in amplitude (A), relaxation time (T_2) and A*T_2 during days 0 to 20 (a), 20 to 37 (b), 37 to 47 (c) and 47 to 61, i.e. the same timeframes as shown in Fig. 8. A, T_2 and A*T_2 product images are shown in the left column of parameter images. Corresponding parameter images depicting increase and decreases in intensity are shown in the middle and right column, respectively. To the right of the three columns of parameter images, photos of the branches of the tree are shown indicating the developmental stage of the tree and its buds. The parameter images in the left column are scaled as indicated in Fig. 7. The parameter images in the middle and right column are scaled as indicated in Fig. 8.
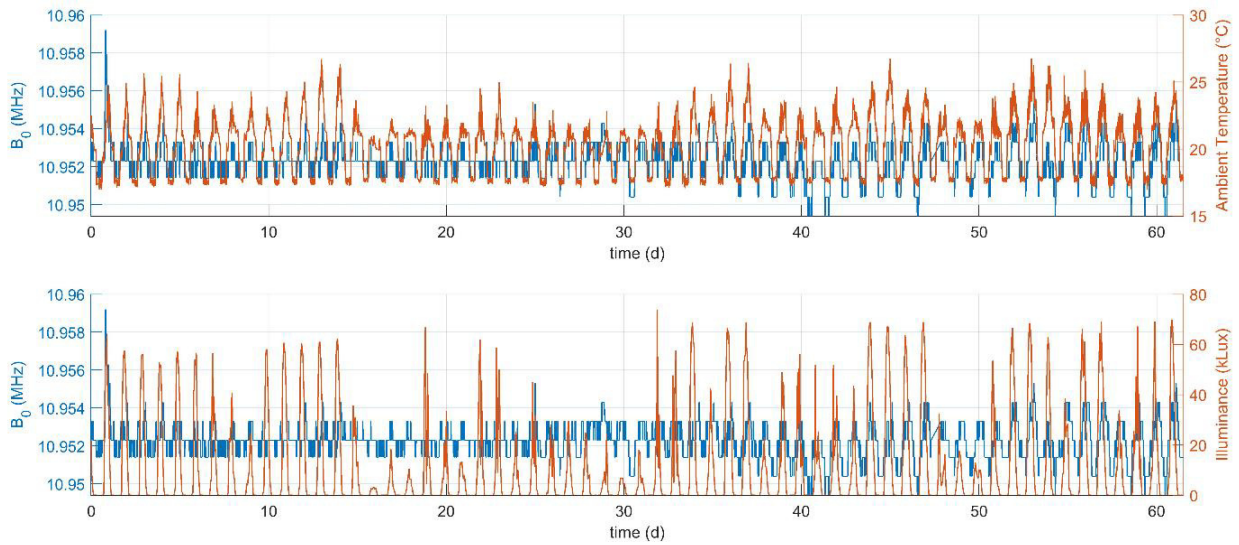
Supplementary data S3: Magnetic field drift during the long-term greenhouse experiment. Plotted are B_0 (blue line) and ambient temperature (red line) during the 62 day greenhouse experiment (top panel), and B_0 (blue line) and solar illuminance (red line) as measured on top of the greenhouse (bottom panel). The accuracy with which B_0 can be measured and corrected is limited by the precision with which frequency can be set in this version of the spectrometer software (Prospa V3.21, Magritek, Wellington, New Zealand), as a result of which the B_0 is plotted in discrete steps. The increase in the maximum temperature extremes and solar irradiation towards the second half of the experiment correspond with the occurrence of warmer and sunnier days in April. During the entire period B_0 showed a variation of 9.8 kHz at the very extremes, but on average did not exhibit a diurnal drift of more than 3.9 kHz. The positive correlation of B_0 and ambient temperature indicates a slight under-regulation of the temperature controller. This in all likelihood is caused by the position of the controller's temperature sensor in the yoke of the magnet, since it cannot be placed at the core of the magnet poles.